

**Techniques in Frequency  
Conversion and Time-Resolved  
Spectroscopy with Nonlinear  
Optical Processes in the  
Femtosecond Regime**

**Dissertation**

zur Erlangung des

Naturwissenschaftlichen Doktorgrades

der Bayerischen Julius-Maximilians-Universität Würzburg

vorgelegt von

**Raman Maksimenka**

aus Soligorsk, Weißrussland

Würzburg 2005

Eingereicht am: .....  
bei der Fakultät für Chemie und Farmazie

1. Gutachter: .....  
2. Gutachter: .....  
der Dissertation

1. Prüfer: .....  
2. Prüfer: .....  
3. Prüfer: .....  
des Öffentlichen Promotionskolloquiums

Tag des Öffentlichen Promotionskolloquiums:.....

Doktorurkunde ausgehändigt am: .....

*To Katja and Matvei*



# *Abstract*

*In the presented work, utilization of the non-linear optical processes for the frequency conversion of the low-energy femtosecond laser pulses on a solid-state base is demonstrated. Raman conversion of femtosecond pulses in a  $\text{KGd}(\text{WO}_4)_2$  crystal is achieved in the regime of impulsive stimulated Raman scattering utilizing special properties of the Bessel beam. Ultra-broadband emission was generated efficiently in micro-structure optical fibers due to high-level confinement of the electric field.*

*Utilization of the non-linear optical processes, such as four-wave mixing, in the time-resolved spectroscopic techniques is demonstrated on the examples of coherent anti-Stokes Raman scattering and transient population gratings applied for the monitoring of the vibrational as well as electronic relaxation pathways in photoexcited polyatomic molecules.*



# Contents

List of Figures . . . . .	ix
<b>1 Introduction</b>	<b>1</b>
<b>2 Generation of femtosecond pulses</b>	<b>5</b>
2.1 Oscillator . . . . .	6
2.2 Amplifier system . . . . .	10
2.3 Optical parametric generators . . . . .	11
<b>I Nonlinear frequency conversion of femtosecond pulses</b>	<b>13</b>
<b>3 Raman conversion of fs pulses</b>	<b>17</b>
3.1 Theory . . . . .	19
3.1.1 SRS in steady-state regime . . . . .	22
3.1.2 SRS in the transient regime . . . . .	24
3.1.3 Impulsive SRS . . . . .	25
3.1.4 Competition of SRS with other nonlinear processes . . . . .	27
3.1.5 Bessel beam pumping . . . . .	28
3.2 Raman media . . . . .	30
3.3 Experimental setup . . . . .	32
3.4 Results and discussion . . . . .	34
3.5 Conclusion . . . . .	39
<b>4 Spectral superbroadening of fs pulses in microstructure fibers</b>	<b>41</b>
4.1 Theory . . . . .	43
4.1.1 Spectral superbroadening of fs laser pulses . . . . .	43
4.1.2 Limiting enhancement of nonlinear-optical processes in small-core microstructure fibers . . . . .	45
4.2 Experimental setup . . . . .	50
4.3 Results and discussion . . . . .	52
4.4 Conclusion . . . . .	62

<b>II</b>	<b>Time-resolved spectroscopy on excited-state dynamics of polyatomic molecules</b>	<b>63</b>
<b>5</b>	<b>Spectroscopic techniques</b>	<b>67</b>
5.1	Pump-probe transient absorption . . . . .	67
5.2	Transient population gratings . . . . .	69
5.3	Pump-CARS scheme . . . . .	73
<b>6</b>	<b>Excited-state dynamics of azulene and its derivatives</b>	<b>81</b>
6.1	Materials. Azulene and its derivatives . . . . .	82
6.2	Experimental details . . . . .	86
6.3	Results and discussion . . . . .	88
6.3.1	Coherent wave-packet motion during $S_0 \leftarrow S_1$ internal conversion in azulene . . . . .	88
6.3.2	Transient absorption of azulene derivatives . . . . .	89
6.3.3	Transient grating on azulene derivatives . . . . .	93
6.4	Conclusion . . . . .	96
<b>7</b>	<b>Vibrational energy redistribution in stilbene-3</b>	<b>97</b>
7.1	Experimental details . . . . .	100
7.2	Materials. Stilbene-3 system . . . . .	101
7.2.1	Raman spectrum of stilbene-3 . . . . .	102
7.3	Results and discussion . . . . .	104
7.3.1	Transient $S_n \leftarrow S_1$ absorption . . . . .	104
7.3.2	Pump-CARS . . . . .	104
7.3.3	Time-domain CARS . . . . .	106
7.4	Conclusion . . . . .	114
<b>8</b>	<b>Conclusion - Zusammenfassung</b>	<b>117</b>
8.1	Conclusion . . . . .	117
8.2	Zusammenfassung . . . . .	122
	<b>Bibliography</b>	<b>127</b>
	<b>Acknowledgments</b>	<b>141</b>



# List of Figures

2.1	Schematic sketch of the femtosecond laser system. . . . .	7
2.2	Schematic view of the cavity configuration for the KLM Ti:Sapphire laser. Here, M1 is an input coupling mirror, M2 and M3 are focusing mirrors, M4 is a highly reflective end mirror, M5 is an output coupler mirror, Ti:Sa is a Ti:Sapphire rod, PC is a prism compressor and BF is a birefringent filter. . . . .	9
2.3	Principle scheme of regenerative amplification in the TRA 1000. . . . .	10
3.1	Group velocity of a Bessel pulse for a refractive axicon. Snapshots of the interference maximum on the axis produced by two tilted pulses for two instants separated by $\Delta t$ are shown. Dashed lines perpendicular to the propagation directions indicate the phase fronts. . . . .	29
3.2	Scheme of the Bessel-pump ISRS experiment. PC: double-pass prism compressor; A: Bessel lens (axicon); C: KGW crystal, variable position along the optical axis; PH: pinhole; L: focusing lens; S: detector (spectrometer/powermeter). . . . .	33
3.3	Spectrum of OPG radiation used in ISRS experiments. Intensity is shown in logarithmic scale. . . . .	33
3.4	A photo of the axicon used in Bessel-pump ISRS experiments . . . . .	34
3.5	Output beams observed on the screen in the far zone of a Raman converter (schematic reproduction). . . . .	36
3.6	Measured spectra for the light beams participating in Raman conversion: pump, spectrum of the pump beam; Stokes, spectrum of Raman-converted radiation in the axial direction; 1st AS, spectrum of the ring generated first anti-Stokes beam; 2nd AS, spectrum of the ring generated second anti-Stokes beam. . . . .	36
3.7	Spectral evolution of the axial Raman converted beam with increasing pump level. . . . .	37
3.8	Dependence of the spectral bandwidth of the axial Raman-converted beam on pump energy. Inset, dependence of the axial Raman-shifted power on the pump power. . . . .	38

4.1	Group-velocity dispersion calculated as a function of radiation wavelength $\lambda$ for fibers consisting of a fused-silica core with a diameter of (1) 0.8, (2) 1.5, and (3) 3 $\mu\text{m}$ and air cladding. The inset shows the cross section of a multiple-core microstructure fiber. The central core has a diameter of about 5 $\mu\text{m}$ . The diameter of six smaller thread-like cores surrounding the central core is 0.8 $\mu\text{m}$ . . . . .	46
4.2	The factor $\xi$ , characterizing the waveguide enhancement of nonlinear optical processes for radiation with the wavelength of 1 $\mu\text{m}$ , calculated as a function of the fiber-core radius $a$ for a fiber with the refractive index of the fiber core $n_{co} \approx 1.45$ and the refractive index of the cladding $n_{cl} \approx 1$ : (curve <b>1</b> ) the result of a full analysis of light confinement in the fiber core with no simplifying assumptions on the factor $\eta$ and (curves <b>2</b> and <b>3</b> ) predictions of equations 4.3 and 4.4 with the mode parameter $u$ found by solving the mode characteristic equation (curve <b>2</b> , asterisks) and with $u \approx 2.4$ (curve <b>3</b> ). . . . .	49
4.3	Schematic of the experiment. PC: double-pass prism compressor; N: neutral density filter; O: 40x micro-objective; F: piece of MS fiber; L: focusing lens; S: spectrometer. . . . .	51
4.4	Two strategies of supercontinuum generation with multiple-core microstructure fibers: <b>a</b> fs laser pulses are coupled into one or several submicron fused-silica threads surrounding the central core of a MS fiber, <b>b</b> pump pulses are coupled into the central fiber core with a diameter ranging from 2 up to 5 $\mu\text{m}$ . . . . .	53
4.5	Spectra of supercontinuum emission produced by <b>a</b> 80 fs pulses of an OPG radiation with a wavelength tuned from 750 to 600 nm in a 0.8 $\mu\text{m}$ core of a microstructure fiber with the cross-section structure shown in the inset of Fig. 4.1 and a length of 2.5 cm, <b>b</b> 80 fs pulses of the OPG radiation with a wavelength tuned from 750 to 620 nm in a 3 $\mu\text{m}$ central core of a microstructure fiber with the cross-section structure shown in the inset of Fig. 4.1 and a length of 37 cm. . . . .	54
4.6	The spectra of chirp-controlled supercontinuum generated in a submicron core of a microstructure fiber: (1) the input pulse, (2) SC produced with a transform-limited pulse, (3) SC produced with a positively chirped pulse. . . . .	55
4.7	Spectral transformation of a 70 fs pulse of 790 nm pump radiation in a microstructure fiber with a 3- $\mu\text{m}$ -diameter central core. The spectrum of the input pulse is shown by line <b>1</b> . The input pulse energy is (2) 10, (3) 50, and (4) 100 pJ. The inset shows the emission pattern at the output of the fiber. . . . .	56

4.8	Mismatch of propagation constant $\delta\beta$ of higher-order waveguide mode involved in the four-wave mixing process in a fused-silica MS fiber. The pump wavelengths are 800 nm (curve 1) and 790 nm (curve 2). Inset 1, cross-section view of the MS fiber. Insets 2 and 3, field intensity distributions in the fundamental and higher-order guided modes. . . .	58
4.9	Spectral transformation of a 70 fs pulse of 790 nm pump radiation in a microstructure fiber. The spectrum of the input pulse is shown by curve 1. The input pulse energy is 0.1 (curve 2), 0.5 (curve 3), and 1 nJ (curve 4). Inset, emission pattern at the output of the fiber. . . .	59
4.10	Spectra of supercontinuum emission produced by 80 fs pulses with a wavelength tuned from 750 to 600 nm in a 0.8 $\mu\text{m}$ peripheral core of a microstructure fiber with the cross-section structure shown in the inset 1 of Fig. 4.8 and a length of 2.5 cm . . . . .	61
5.1	A schematic diagram of the pump-probe transient absorption setup in the form used for the experiments presented in the work. For details see text. . . . .	68
5.2	Potential energy diagram illustrating a TG experiment. . . . .	71
5.3	Scheme of a TG experiment setup as used for experiments described in section 6.3.1. For details see text. . . . .	72
5.4	The BOXCARS arrangement of the beams as used for the TG experiments. For details see text. . . . .	73
5.5	Potential energy diagram illustrating pump-CARS experiment. . . . .	75
5.6	Scheme of pump-CARS setup as used in the experiments described in chapter 7. For details see text. . . . .	77
5.7	BOXCARS arrangement of the beams as used in pump-CARS experiments. For details see text. . . . .	78
6.1	Absorption spectrum of azulene (black line). Inset shows the zoomed part of the spectrum corresponding to the $S_1$ absorption (blue line) together with the spectra of pump (green line) and probe (red line) pulses used in the TG experiments described in this section. . . . .	83
6.2	The chemical structures of the investigated azulene derivatives. . . . .	84
6.3	Absorption spectra of the investigated azulene derivatives shown in Fig. 6.2. Dashed line marks the position of the 490 nm pump, whereas dot-dashed line marks the position of 380 nm pump pulses. . . . .	85
6.4	Transient grating signal of azulene rendering the $S_1$ dynamics at a pump wavelength of 620 nm. . . . .	89
6.5	Upper panel, difference absorption spectra of compound <b>2</b> (Fig. 6.2) obtained for an excitation at 490 nm; lower panel, difference absorption of compound <b>2</b> plotted as a function of the pump delay time $\Delta t$ for different wavelengths. . . . .	90

6.6	Upper panel, difference absorption spectra of compound <b>2</b> (Fig. 6.2) obtained for an excitation at 380 nm; lower panel, difference absorption of compound <b>2</b> plotted as a function of the pump delay time $\Delta t$ for different wavelengths. . . . .	91
6.7	A model postulated for the relaxation pathways of the electronic excited states of the azulene derivatives. Here, $t_1$ is the time constant of $g \leftarrow e_1$ internal conversion, $t_2$ is the time constant of $e_d \leftarrow e_1$ IC. For further details see text. . . . .	92
6.8	Spectrally integrated TG signals obtained for the azulene derivatives shown in Fig. 6.2 excited at 490 nm (panel A) and 380 nm (panel B), respectively. . . . .	94
7.1	Chemical structure of stilbene-3. . . . .	102
7.2	Raman spectrum of stilbene-3 dissolved in 1:1 ethanol/water mixture. Excitation wavelength 514 nm. . . . .	103
7.3	Lower panel, ground-state absorption spectrum of stilbene-3 (black line) together with the spectrum of the UV-pump pulse (dark blue line); upper panel, difference absorption spectrum of the $S_1$ state of stilbene-3 (black line), spectrum of Stokes pulse (red line), spectrum of CARS-pump pulse (green line), spectrum of anti-Stokes signal (blue line). . . . .	105
7.4	Transient CARS signal of stilbene-3 integrated between <b>A</b> 1550 and 1850 $\text{cm}^{-1}$ and <b>B</b> 1100 and 1350 $\text{cm}^{-1}$ relative shift to the maximum of the CARS-pump spectrum as a function of the delay to the UV-pump, $\Delta t_1$ (see Fig. 5.5). Insets show the CARS intensity for longer time delays (up to 500 ps). Circles represent the experimental data, solid lines - the fitted data. . . . .	107
7.5	CARS spectra of stilbene-3 plotted as a function of the delay time $\Delta t_2$ (see Fig. 5.5). Difference between pump and Stokes is tuned for both cases to approximately 1400 $\text{cm}^{-1}$ (680 nm). Panel <b>A</b> , ground state CARS (UV-pump is off), panel <b>B</b> , excited state resonance CARS (UV-pump is on, $\Delta t_1 = 20$ ps). The black curves are cuts through the data at a CARS wavelength position of 620 nm. . . . .	109
7.6	FFT amplitude of the oscillating contributions to the time-domain CARS signal from the (A) ground and (B) excited state stilbene-3 in an ethanol/water solution plotted as a function of the CARS signal relative wavenumber. . . . .	111

## Chapter 1

# Introduction

Nonlinear optics study the processes of light-matter interaction, whose character essentially depends on the intensity of light. Although the Kerr effect, manifesting itself in the dependence of the material refractive index on the electro-magnetic field intensity, was known since the end of the nineteenth century, the *true* dawn of the experimental nonlinear optics braked after the source of intense enough radiation was invented - in 1960s. Second harmonic generation, a type of parametric light interaction, was observed by Franken [1] in 1961. Shortly after that, in 1962, a sight of stimulated Raman scattering was caught by Woodbury and Ng [2] during experiments with Q-switching in ruby laser. The third important type of nonlinear optical phenomenon, self-action or AC Kerr effect, was observed experimentally in the form of self-focusing in 1965 by Pilipetskii and Rustamov [3]. All three named types of nonlinear optical effects can be utilized to extend the spectral range of the coherent emission, produced by laser.

In the first part of the presented work, the frequency conversion of femtosecond laser pulses is investigated in two types of solid-state media,  $\text{KGd}(\text{WO}_4)_2$  (potassium gadolinium tungstate, KGW) crystal and microstructure fibers. The purpose of these experiments was to explore nonlinear optical phenomena in solid-state materials in the femtosecond time-regime and to examine possibilities to generate coherent broadband femtosecond radiation with well controlled properties on a solid-state background. A detailed understanding of the mechanisms of nonlinear frequency conversion is crucial

for assessing the possibilities of using generated broadband radiation for spectroscopy, metrology, biomedical applications, pulse-compression, etc.

In order to achieve Raman conversion in the regime of impulsive stimulated Raman scattering, the KGW crystal was pumped with a Bessel beam, allowing for suppression of competing nonlinear processes, such as self-phase modulation. Pumping with a Bessel beam has an additional advantage in the possibility to compensate the group-velocity mismatch between the pump pulse and the generated Stokes pulse, introduced by the dispersion of the index of refraction in crystal.

Efficiency of nonlinear frequency conversion can be greatly increased by confinement of the electro-magnetic field of laser pulses in multiple cores of microstructure fibers. In such conditions, the threshold energy for nonlinear optical processes is substantially lowered. A microstructure fiber was utilized for the generation of ultra-broadband radiation on a low-energy level. A design of such fiber combines the ideas of a holey fiber and a tapered fiber by integrating several small core high-refractive-index-step fibers into a bundle.

Nonlinear optical interactions of intense laser light with matter provide an outstanding spectroscopic tool. Great number of degrees of freedom available within multiwave-mixing and other nonlinear optical processes allows the investigation of microscopic material structure and selective monitoring of elementary events in complex chemical reactions. Coherent nature of the signal, produced as a result of nonlinear interactions, leads to extreme sensitivity of nonlinear spectroscopic techniques. Time resolution available with the modern laser equipment allows for detection of the fastest possible motions in materials, such as nuclear vibrations or even electron transitions.

In the second part of this work, energy transformations in photoexcited polyatomic molecules are investigated by means of femtosecond four-wave mixing techniques. Nuclear energy relaxation subsequent to a photo-induced electronic transition in the model system stilbene-3 was explored by means of femtosecond pump-CARS technique. Here, the CARS process is implemented as the probe mechanism in a conventional pump-probe scheme and serves as a mode-selective filter allowing for the population dynamics within specific vibrational modes to be monitored. These exper-

iments provided insight into ultrafast dynamics of nuclear geometry rearrangement upon photoexcitation.

The transient grating as well as pump-probe transient absorption techniques were applied to investigate the non-radiative transitions in azulene and its derivatives. Coherent wave-packet motion was observed during internal conversion from the first excited to the ground electronic state of azulene. For azulene derivatives time constants associated with possible non-radiative decay channels of the first as well as of the second excited electronic states were determined with high accuracy. The knowledge of the excited-state electronic structure and dynamics will lead to more effective utilization of the non-linear optical properties of azulene derivatives as active components in molecular electronics devices.





## Chapter 2

# Generation of femtosecond pulses

It is impossible to imagine modern world without lasers. Lasers are used in various fields: from fundamental science and medical applications to communication and entertainment. Since the invention of the laser in 1960 [4–6] the generation of shorter and shorter laser pulses was a quest for scientists. Indeed, the generation of laser pulses of hundreds of attoseconds ( $10^{-16}$  s) duration was achieved recently [7, 8].

It was the cavity dumping method, that made it possible to obtain laser pulses as short as  $10^{-8}$ – $10^{-9}$  s in the early sixties. The high peak power ( $10^7$ – $10^8$  W) of such pulses lead to the development of nonlinear optics. A few years later, in the mid-sixties, the invention of mode-locking methods lead to the generation of picosecond ( $10^{-12}$  s) pulses with peak powers as high as  $10^{10}$  W. Non-linear optical methods of generation and compression were demonstrated, which allowed to tune frequency of picosecond pulses and cover thus IR and VIS spectral ranges. It was in 1986, when progress in the development of passive mode-locking methods lead to the generation of 27 fs pulses [9], which were later compressed down to 6 fs [10]. These pulses contained only three optical cycles. The next decade was spent for an improvement of various generation, amplification, conversion and compression methods. Specifically, the development of solid state lasers capable to produce ultrashort pulses made femtosecond equipment much cheaper, safer and more compact.

By means of femtosecond pulses it is possible to create strongly non-equilibrium states of fast relaxing excitations (relaxation times  $10^{-13}$ – $10^{-14}$  s), i.e. electronic excitations in polyatomic molecules, semiconductors and metals, and observe new types of ultrafast optically induced phase transitions. The possibility to study chemical reactions in real time lead to the development of new science branch, *femtochemistry*, for which 1999 the Nobel Prize in Chemistry was awarded to Ahmed Zewail [11]. In communication technologies femtosecond pulses allow for the highest possible speed of optical data processing and transmission. The high peak power available within the short duration time of a femtosecond pulse ( $10^{12}$  W for 100 fs pulse of energy 0.1 J) made it possible to obtain electric fields up to  $10^{10}$  V/cm, which are higher than typical intra-molecular fields ( $10^9$  V/cm for hydrogen atom). Predictions of nonlinear quantum electrodynamics (nonlinear light scattering on relativistic electrons, light-on-light scattering in vacuum etc.) could be verified directly by means of intense femtosecond pulses [12].

In this chapter the laser equipment is described, which was used through all experiments presented in this work. The system is based on the Kerr-lens mode-locked femtosecond oscillator (Mira 900, Coherent) and a regenerative amplifier system (CPA 1000, Clark MXR) together with two optical parametric generators (TOPAS, Light Conversion). The layout of the laser system is depicted in Fig. 2.1. Detailed description of the elements together with the basic theoretical background of their operation is presented in the following sections.

## 2.1 Oscillator

Short-pulse laser operation requires a phase-locking of the cavity *eigenfrequencies* (longitudinal modes), which is possible when an *amplitude modulator* with a modulation frequency equal to the frequency spacing of the modes is introduced inside the cavity. This type of operation is referred to as *mode-locking*. In the time-domain picture, mode-locking means that the amplitude modulator opens and closes synchronously with the light propagating through the cavity. The modulator can either be driven by an external signal source (active mode-locking) or directly by the optical pulses inside the laser cavity (passive mode-locking).

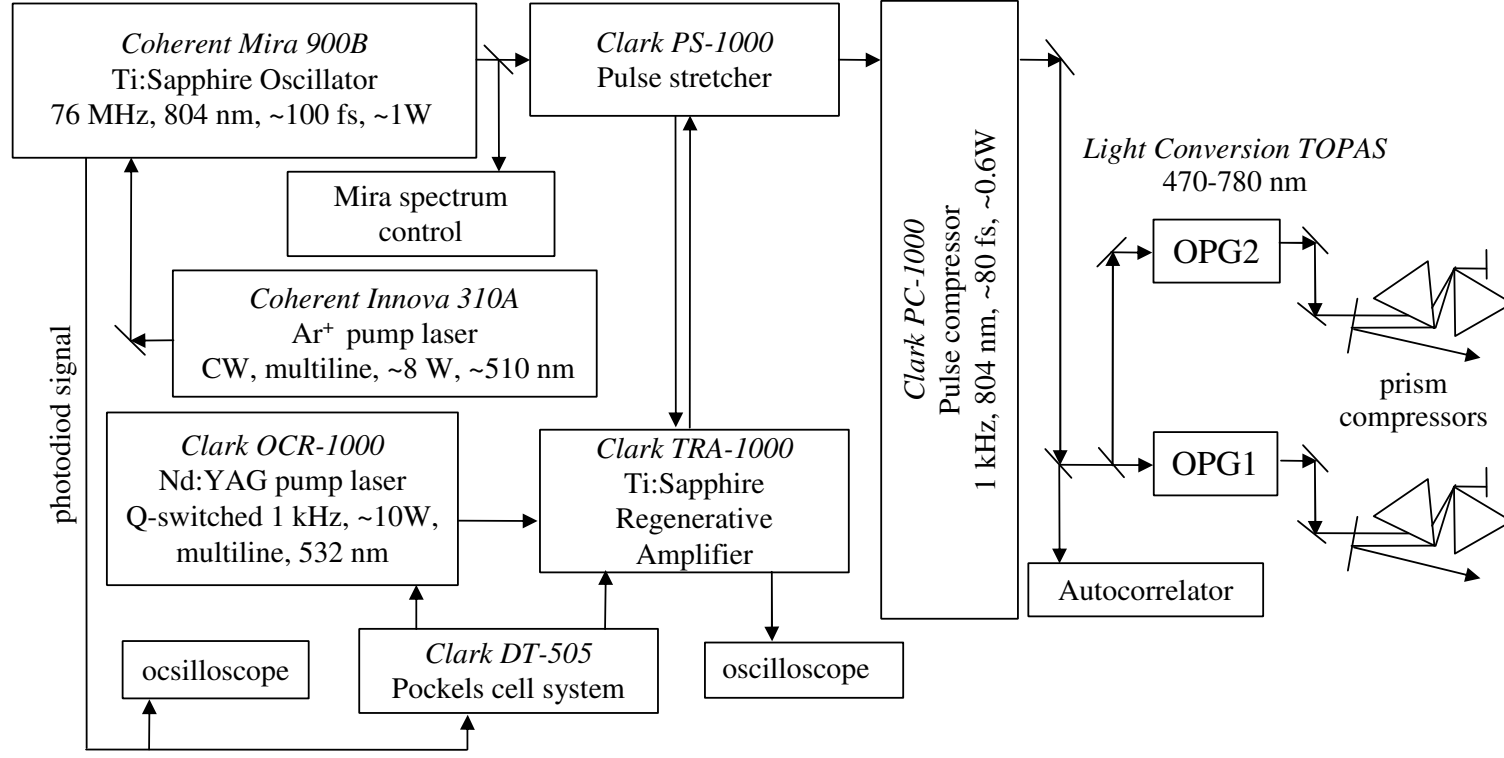


Figure 2.1: Schematic sketch of the femtosecond laser system.

Until 1991 only dye lasers were able to produce sub-100 fs pulses. In such lasers the saturable absorption and the saturable gain of organic dyes act together as an optical shutter. In solid-state media a fast saturable absorption action using self-focusing (Kerr-lensing) and aperturing was first demonstrated for Ti:Al<sub>2</sub>O<sub>3</sub> (Ti:Sapphire) [13]. The theory of Kerr-lens mode-locked (KLM) lasers is well described in the literature [14, 15]. Therefore, only the basic operation principles of KLM Ti:Sapphire oscillator are considered here.

The interaction of intense laser light with a medium leads to changes in the index of refraction of the medium (optical Kerr effect). In the transverse direction this results in the formation of an effective *Kerr lens*, which focuses the beam (self-focusing). Normally only the instantaneous intensity of the mode-locked pulse is sufficient to form the lens, while the weak intensity of continuous-wave (cw) light is not. Hence, the lens is only formed upon the arrival of the mode-locked pulse and only for these pulses the beam will be spatially narrowed. The addition of a slit to allow only narrow beams to pass through unattenuated forms a complete saturable absorber system providing a real driving force for mode-locking. In order to start mode-locking, high intensity fluctuations have to be introduced by changing the cavity length at the proper speed and thus allowing for a large number of modes to lase simultaneously.

The propagation of the ultrashort pulse through a dispersive medium (with normal refractive index dispersion) is affected by the group velocity dispersion (GVD), introduced by the difference in propagation rates of the different frequency components of the pulse, and by self-phase modulation (SPM), which is the result of a longitudinal optical Kerr effect. Both GVD and SPM lead to a time delay of the short-wavelength components of the pulse with respect to the long-wavelength components, introducing thus a *positive chirp*. In order to compensate this chirp, an element with negative GVD is required within the oscillator system. In the Mira 900, a prism compressor serves as such element.

Self-phase modulation constitutes the basis of a stable operating KLM laser. If a pulse becomes more intense, the increased SPM will cause the pulse to broaden, distributing the energy over a longer period of time and thus reducing the pulse intensity and bringing it back to the equilibrium state [16].

In the Mira 900 laser, a Ti:Sapphire rod acts as an active medium and at the same time as the Kerr medium. Optical pumping of the gain medium is provided by an Ar-ion laser (Innova 300, Coherent) operating in a continuous-wave multiline mode. A simplified scheme of the cavity configuration of the self-mode-locked Ti:Sapphire laser is depicted in Fig. 2.2. The spectrum of the oscillator emission is recorded by means of a fiber spectrometer (Ocean Optics). Usually its center wavelength is set to 804 nm with a FWHM of 12 nm.

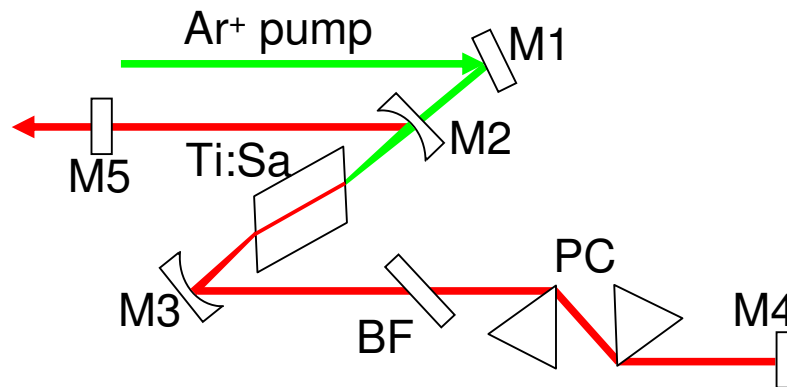


Figure 2.2: Schematic view of the cavity configuration for the KLM Ti:Sapphire laser. Here, M1 is an input coupling mirror, M2 and M3 are focusing mirrors, M4 is a highly reflective end mirror, M5 is an output coupler mirror, Ti:Sa is a Ti:Sapphire rod, PC is a prism compressor and BF is a birefringent filter.

The cavity length of the Mira 900 is 1.5 m and it takes light  $\sim 10$  ns to make one round-trip inside the cavity. Therefore, every 10 ns a single pulse is emitted from the output coupler mirror, resulting in a repetition rate of 75 MHz. The average power emitted is around 1 W and therefore pulses have typically energies of 10 nJ. As long as the efficiency of non-linear processes is determined by the intensity of the electric field of the pulse, it is desirable to increase the pulse energy and thus achieve a higher field intensity. An amplifier system like the one described in the next section serves this propose.

## 2.2 Amplifier system

The basic design principles of amplifiers have been established for picosecond and nanosecond pulse amplification. The pulses to be increased in energy are sent through a medium, which provides the required gain factor. However, on a femtosecond time scale new design methods are required to keep the pulse duration short and to avoid undesired nonlinear effects caused by the extremely high intensities of the amplified ultrashort pulses. A common technique to avoid the problems associated with high peak powers is to use dispersive elements to stretch the pulse duration to a picosecond time scale prior to amplification [17, Chapter 6]. In the CPA 1000 amplifier system the pulse stretcher PS 1000 utilizes a combination of gratings and a telescope in order to conserve the original pulse spectrum. After the amplification the original pulse duration can be restored by the conjugated dispersion line (PC 1000 pulse compressor) if the amplifier bandwidth exceeds that of the pulse and the amplifier is not saturated.

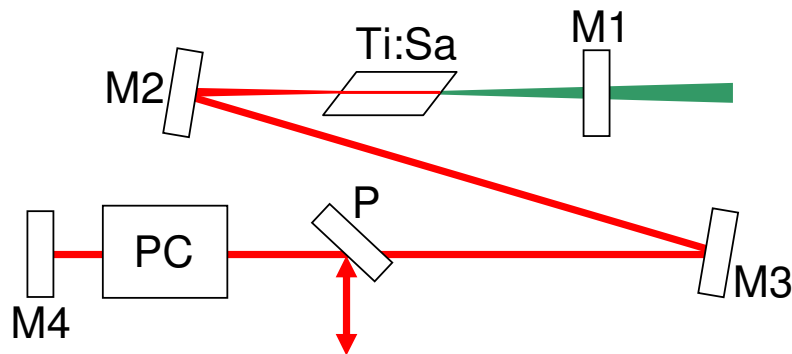


Figure 2.3: Principle scheme of regenerative amplification in the TRA 1000.

A broad gain bandwidth and high saturation energy density make some solid-state materials prime candidates for the generation of powerful femtosecond light pulses. A large energy storage time ( $10^{-6}$  s) is generally associated with the small gain cross-section of these amplifying media. *Regenerative amplification* is the most efficient method to transfer energy to a fs pulse. The concept of regenerative amplification is illustrated in Fig. 2.3. The gain medium is placed in a resonator built by the dichroic

mirror M1 and the high reflective end mirror M4. After the seed pulse is coupled into the resonator through a polarizer P, the Pockels cell PC is switched to rotate the polarization of the seed pulse and to Q-switch the resonator. The pulse circulates in the resonator and is continuously amplified. After a certain number of round trips (determined by the energy storage time and the time needed to reach saturation) the Pockels cell turns the polarization again and the amplified pulse is coupled out by reflection from polarizer P.

The gain medium is pumped by a Q-switched Nd:YAG laser (ORC 1000). The Pockels cell system (DT 505) is synchronized by a diode signal from the oscillator and provides the timing for the amplifier pump laser and the amplifier itself resulting in a pulse repetition rate of 1 kHz. The average power of the amplifier output is around 0.6 W, resulting in pulse energies of 0.6 mJ. The central wavelength of 804 nm is determined by the oscillator. The temporal profile of the pulses is characterized with an autocorrelator (AC 150) based on the non-collinear sum-frequency generation. The typical FWHM of the autocorrelation trace for amplified pulses is 80 fs.

## 2.3 Optical parametric generators

Spectroscopic experiments often require tunable sources of radiation in order to exploit various resonances of the system under investigation. One possibility for the frequency conversion of amplified fs laser pulses is optical parametric interaction in a non-linear crystal. If frequency- and phase-matching conditions

$$\omega_s + \omega_i = \omega_p \quad (2.1)$$

$$\mathbf{k}_s + \mathbf{k}_i = \mathbf{k}_p$$

are satisfied for *pump*, *signal* and *idler* waves, signal and idler waves will be amplified in a medium with high quadratic non-linearity ( $\chi^{(2)}$ ).

Optical parametric light converters built in a traveling-wave configuration permit the generation of coherent fs pulses with a conversion efficiency as high as 35% and a tuning range limited only by the infrared absorption of the the used crystal [18]. For all experiments presented here, two 'traveling-wave optical parametric amplifiers of

superfluorescence' (TOPAS, Light Conversion) were used employing three operation stages arranged in a single BBO crystal. The first stage serves as a seed emitting broad-band superfluorescence (SF). In the second stage only the collinear part of the SF is preamplified and the seed spectrum is narrowed. The last stage that is pumped by 90% fraction of the available pump boosts the energy of the parametric pulse [19]. The operation wavelength range of the TOPAS is 1160 to 1620 nm for the signal and 1600 to 2320 nm for the idler wave. In order to obtain light pulses in the visible range, a second BBO crystal is placed directly after the output of the TOPAS. This offers several possibilities for wavelength conversion. Doubling of the signal frequency allows for radiation from 560 to 780 nm to be obtained. Mixing of signal or idler with residual pump through sum-frequency generation allows for tuning from 470 to 620 nm. Thus, the whole visible spectrum can be covered (however with different efficiency). UV wavelengths are accessible by additional frequency doubling the visible light. In order to compensate GVD gained inside the TOPAS, a double prism compressor in the standard configuration [20] is placed behind each OPG.

Finally, pulses of 70–100 fs duration and energy of 10–20  $\mu\text{J}$  tunable via the whole visible range can be obtained.



Part I

Nonlinear frequency  
conversion of femtosecond  
pulses



The intense growth of laser light applications during the last years (in medicine, industry, communications, etc.) revealed the interest of exploitation of additional laser wavelengths. New spectral ranges can be covered by new laser active media or by means of nonlinear effects in optical materials (gases, dyes, crystals, nanostructures, structured glass fibers) that are used for conversion of laser radiation frequencies.

Nonlinear optical conversion techniques firstly involve the use of elastic processes such as second and higher harmonics generation, sum frequency and difference frequency generation, and optical parametric generation and amplification. Many various configurations and optical materials have been utilized employing these nonlinear processes, resulting in range of wavelengths accessible with today's devices extending from the ultraviolet to the far infrared. Another important group of nonlinear optical effects is formed by inelastic scattering processes, which main representatives are stimulated Brillouin and stimulated Raman scattering. Stimulated Raman scattering is widely used as an effective and flexible mechanism for the frequency conversion in the whole range of laser operation regimes – from continuous-wave to femtosecond.

Combination of various non-linear optical processes can result in spectral superbroadening of intense laser pulses, termed to as a *white light* generation or a *supercontinuum* generation. Spectral superbroadening allows for the construction of coherent light sources with the spectrum spanning from UV to IR, which finds its use in a range of applications, like, e.g. generation of ultrashort pulses of the duration in the range of the few optical cycles or pump-probe transient absorption spectroscopy.



## Chapter 3

# Raman conversion of fs pulses

Stimulated Raman scattering (SRS) can be used to shift the laser emission wavelength over a fixed frequency shift, gaining access to additional laser lines. The spectral areas reachable with SRS extend from ultraviolet to infrared, depending on the pump laser and Raman material used. SRS can therefore be used as a supplement or an alternative to other nonlinear techniques. Very efficient frequency conversion of up to 92% quantum efficiency was recently demonstrated in gas-filled hollow core photonic crystal fibers [21].

Solid state materials, possessing favorable features for stimulated Raman scattering, have been subject to intense investigation by several research groups over the last years. The high density of solids ( $10^{22}$ – $10^{23}$  cm<sup>3</sup>) results in high Raman gains. The restricted motion of the atoms and the local symmetry in crystals minimizes line broadening and decreases the competition between various vibrational modes. This leads to an enhancement of the Raman effect in crystals compared to gases and liquids. The higher peak Raman cross sections in crystals result in lower SRS thresholds, higher Raman gain, and greater Raman conversion efficiency. A great variety of crystals, both natural and artificially synthesized, have been investigated for Raman scattering characteristics over the last 30 years [22].

For laser pulses with durations of tenths of femtoseconds, a time-scale being close to a vibrational period of most Raman-active media, the transient SRS regime is termed *impulsive stimulated Raman scattering* (ISRS) [23,24]. Until now ISRS has been successfully used as a time-resolved spectroscopic method [25], while Raman conversion in gaseous SF<sub>6</sub> has been investigated in this regime only very recently [26–29]. These experiments mainly focused on the generation of phase-locked Raman sidebands [27–29].

The efficient Raman conversion of picosecond laser pulses in a barium tungstate crystal [30] and of femtosecond pulses stretched to picosecond durations in a barium nitrate crystal were demonstrated recently [31]. One of the main problems to be solved in these experiments is the elimination of processes such as self-phase modulation and continuum generation competing with SRS. Usually Raman-conversion experiments are performed such that the Gaussian pump and the generated Stokes beams propagate on the same trace as superimposed beams. During propagation in a nonlinear media, pulses are subject to all changes that are due to Raman and competing effects. Therefore, SRS is strongly suppressed under such conditions [32].

Some years ago the strong suppression of the effects competing with SRS was demonstrated in a liquid Raman medium being pumped with a Bessel beam [33]. Additional advantage of Bessel compared with Gaussian pumping in SRS experiments is the possibility of generating axial Stokes radiation, which is spatially separated from the pump Bessel beam [34]. The possibilities of using Raman conversion under ISRS conditions and the generation of super-broadband laser radiation, which were discussed theoretically in Ref. [35], make Bessel pumping a very attractive approach.

In this chapter the theoretical description of SRS in different regimes (from steady-state to impulsive) is presented along with the description of the first experiments on the Raman conversion of 70-fs pulses in a solid-state medium (potassium gadolinium tungstate crystal) in the ISRS regime using the Bessel pumping scheme [36].

### 3.1 Theory

The phenomenon of combination (Raman) scattering was theoretically predicted by Smekal in 1923 [37] and in 1928 it was simultaneously and independently observed by two Russian scientists, Landsberg and Mandelshtam, investigating light scattering in crystals [38] and two Indian scientists, Raman and Krishnan [39], who made their observation performing light scattering experiments in liquids.

Raman scattering is a process, in which the incident light, termed the pump wave, is scattered into light of longer wavelength, termed the Stokes wave, with the energy difference between the incident ( $\omega_L$ ) and scattered ( $\omega_S$ ) photons being taken up in excitation of the appropriate mode of the material ( $\omega_R = \omega_L - \omega_S$ ). Raman scattering, in which the incident light is scattered to a light wave at a shorter wavelength, accompanied by a de-excitation of an internal mode of the medium, is termed to as anti-Stokes scattering.

Raman scattering can occur in spontaneous and stimulated regimes. In the spontaneous regime, the powers of the Stokes and anti-Stokes waves are proportional to the power of the pump wave. The entire manifold of Raman-active internal modes is present in the scattered spectrum, with the relative intensities of the Stokes components being determined by the relative Raman scattering cross sections for the various modes. The intensity of anti-Stokes modes is reduced from that of the Stokes modes for the same internal level by the factor  $e^{-\hbar\omega_R/kT}$ , originated from Boltzman population distribution of internal modes of the medium. Spontaneous Raman scattering is used primarily for spectroscopic studies, particularly for the investigation of vibrational modes. Stimulated Raman scattering occurs when the intensity of the incident pump wave is strong enough to initiate a positive feedback effect in the medium, resulting in an exponential growth of the scattered wave in forward (and backward) direction within a light beam of small angular divergence [40, 41].

SRS was discovered shortly after the advent of the laser [42, 43], and a laser is able to provide the sufficiently high peak powers required for nonlinear processes, like SRS. There have been a great number of theoretical descriptions of SRS presented in the literature, and the process has been treated classically, semi-classically and

quantum-mechanically. For the case of large photon flux the various theories give similar results [41].

### Electric fields

The total electric field relevant for the process of SRS consists of an incident laser field and a Stokes field, generated in the Raman active medium. The propagation of the light pulses through the sample and the interaction with the vibrating molecules are described by Maxwell's equations, which lead to the well known wave equation [44]:

$$\Delta \mathbf{E} - \frac{n^2}{c^2} \frac{\partial^2 \mathbf{E}}{\partial t^2} = \frac{4\pi}{c^2} \frac{\partial^2 \mathbf{P}}{\partial t^2}. \quad (3.1)$$

Here  $n$  denotes the refractive index of the medium under investigation. The polarization of the medium  $\mathbf{P}$  contains linear and nonlinear parts in the most general case. Nonlinear polarization  $\mathbf{P}^{\text{NL}}$  represents the macroscopic change in the polarization connected with the coherent material excitation of the stimulated Raman process:

$$\mathbf{P}^{\text{NL}} = N \frac{\partial \alpha}{\partial Q} Q \mathbf{E}, \quad (3.2)$$

where  $N$  is the number of molecules per  $\text{cm}^3$  and  $\partial \alpha / \partial Q$  is the derivative of the oscillator polarizability with respect to a given normal coordinate.

In the following the usual assumption is made, that the total light field consists of plane waves of different frequencies and time-dependent amplitudes:

$$\mathbf{E}_{L,S} = 1/2 [E_{L,S}(z, t) e^{-i(\omega_{L,S}t - k_{L,S}z)} + c.c.]. \quad (3.3)$$

Here  $E_{L,S}$  are the slowly varying amplitudes,  $\omega_{L,S}$  are the optical frequencies, and  $k_{L,S}$  are the wave vectors of pump and Stokes waves, respectively.

For simplicity, stimulated light scattering is considered to occur only in the forward direction. The short duration of the pulses ( $\sim 10^{-13}$  s) used in the experiment and the resulting short interaction length for stimulated backward scattering make this process negligible [44].



### Molecular system

The molecular vibrations are described by equations for  $Q$  and  $\Delta N$ , the normal mode coordinate and the difference in the population between the lower and upper Raman transition levels, respectively (Bloemberger-Shen model for a nonlinear oscillator [45]):

$$\frac{\partial^2 Q}{\partial t^2} + \Gamma_R \frac{\partial Q}{\partial t} + \omega_R^2 Q = -\frac{1}{2m} \frac{\partial \alpha}{\partial Q} \mathbf{E}^2 \Delta N \quad (3.4)$$

$$\frac{\partial \Delta N}{\partial t} = \frac{1}{\hbar \omega_R} \frac{\partial \alpha}{\partial Q} \mathbf{E}^2 \frac{\partial Q}{\partial t} + \Gamma'_R (1 - \Delta N). \quad (3.5)$$

It has been assumed in equations 3.4 and 3.5 that the energy levels of the molecule are well represented by a two level system. The parameters in equations 3.4 and 3.5 are defined as follows:  $m$  is the reduced mass associated with the vibration,  $\omega_R$  is the resonance frequency of the vibration. The damping constant  $\Gamma_R$  equal to the line width  $\delta\omega_R$  has been introduced phenomenologically. It corresponds to  $1/T_2$  in the Bloch equations, where  $T_2$  represents the dephasing time of the vibrational amplitude.

The damping constant  $\Gamma'_R$  corresponds to  $1/T_1$ , the inverse of the lifetime  $T_1$  of the vibrational state. The equilibrium value of  $\Delta N$  is assumed to be below 1, since  $\hbar\omega_0 \gg kT$  and in most cases the laser and Raman intensities are not high enough to change the population difference appreciably.

The amplitude of the normal mode of the material excitation is defined by:

$$\mathbf{Q}_i = 1/2 [Q_i(z, t)e^{-i(\omega_R t - k_R z)} + c.c.]. \quad (3.6)$$

The relation between frequencies and wave vectors is chosen to satisfy the conditions corresponding to conservation of energy and momentum, respectively:

$$\begin{aligned} \omega_R &= \omega_L - \omega_S \\ k_R &= k_L - k_S. \end{aligned} \quad (3.7)$$

## Rate equations

The following system of the parametrically coupled equations describes the evolution of the Stokes wave [46]:

$$\begin{aligned}\frac{\partial Q}{\partial t} + \Gamma_R Q &= -i\kappa_1 E_L E_S^* \\ \frac{\partial E_S}{\partial z} + \frac{1}{\nu_{gS}} \frac{\partial E_S}{\partial t} &= -i\kappa_2 Q^* E_L,\end{aligned}\quad (3.8)$$

where  $\nu_S$  is the group velocity of the Stokes wave. The parametric coupling constants  $\kappa_1$  and  $\kappa_2$  are given by:

$$\kappa_1 = \frac{1}{4\omega_R m} \frac{\partial \alpha}{\partial Q}, \quad \kappa_2 = \frac{N\omega_S}{4n_S c} \frac{\partial \alpha}{\partial Q}. \quad (3.9)$$

The form of equations 3.8 does not take into account the effect of a finite beam diameter in the  $xy$  plane. It is also assumed that diffraction, level saturation, pump depletion, anti-Stokes and higher order Stokes radiation can be neglected. A more general form of rate equations for SRS can be found in Ref. [40].

### 3.1.1 SRS in steady-state regime

If the time variation of the wave envelopes is slow compared to the dephasing time  $T_2$ , time derivatives in equations 3.8 can be neglected. Assuming that the ground state population is unchanged, neglecting the transverse spatial derivative and solving the resulting simplified rate equations, the Stokes intensity can be obtained as [40]:

$$I_S(z) = I_S(0)e^{g_{SS}I_L z}, \quad (3.10)$$

where  $z$  is the length of the interaction region and  $g_{SS}$  is the steady-state Raman gain coefficient, given by

$$g_{SS} = \frac{N\omega_S}{4\Gamma_R n_S n_L m \omega_R c^2 \epsilon_0} \left( \frac{\partial \alpha}{\partial Q} \right)^2. \quad (3.11)$$

In the absence of an injected Stokes beam, or 'seed', the growth of the Stokes wave is due to spontaneously scattered Stokes photons ( $I_S(0) = I_{SN}$ ). Equivalent noise input is given by

$$I_{SN}(\omega_S) = \frac{\hbar\omega_S^2 n_S^3}{8\pi^3 c^2} \Delta\Omega. \quad (3.12)$$

Here  $\Delta\Omega$  is the solid angle of the gain column [47].

The classical Raman cross section is related to the Raman gain by [40]

$$g_{SS} = \frac{16\pi^2 N c^2}{n_S^2 \hbar \omega_S^3 \delta \omega_R} \frac{\partial \sigma}{\partial \Omega} \quad (3.13)$$

From equation 3.13 it can be seen that the gain coefficient essentially depends on two parameters,  $\partial\sigma/\partial\Omega$  and  $\delta\omega_R = \Gamma_R$ , the scattering cross section and the spontaneous Raman line width, respectively. In the transparent regions of the spectrum, the Raman cross section scales as  $\omega_S^4$  and the Raman gain coefficient scales as  $\omega_S$ .

Initially, stimulated Raman gain coefficients were calculated from measurements of the spontaneous Raman scattering cross section or estimated from measurements of the Raman threshold. The most accurate determination of Raman gain coefficients are now made with steady-state amplification measurements in the low-gain regime. The conditions for steady-state Raman amplification are encountered when both the pump and the incident Stokes radiation are either cw or narrow-band pulses, which contain no rapid internal temporal variations and with pulse durations longer than the steady-state time given by

$$t_{SS} = G_{SS} T_2, \quad (3.14)$$

where  $G_{SS}$  is the total steady-state Raman gain,

$$G_{SS} = g_{SS} I_L z. \quad (3.15)$$

The line width of the Raman transition is readily measured in the small-signal regime, e.g. using spontaneous Raman spectroscopy. The Raman gain is highest at the line center, and thus spectral narrowing is expected to occur as the gain is increased. The spectrally narrowed line width for a Gaussian pulse which propagated a distance  $z$  through an amplifying medium with a Raman gain is given by [48]

$$\delta\omega_R(z) = \delta\omega_R(0) \left(1 + \frac{2g_R I_p z}{\ln 2}\right)^{-1/2}. \quad (3.16)$$

### 3.1.2 SRS in the transient regime

When the laser pulse duration reaches values shorter than the dephasing time  $T_2$ , Raman conversion occurs in a transient regime. The dephasing times observed in most Raman media lies in the picosecond range. Therefore SRS generated in these media by pulses with durations of hundreds of femtoseconds is achieved under transient conditions.

Transient SRS in  $H_2$  and other gases was first observed by Hagenlocker et al. in 1967 [49] and since then has been widely investigated experimentally and theoretically [32,50,51]. The decrease in Raman gain in going from the steady state to the transient regime, the dependence of Raman gain on pulse energy rather than on pump intensity [50,51] and strong competition with other nonlinear optical effects such as self-phase modulation, cross-phase modulation, and continuum generation, that arise as a result of high intensities, have been demonstrated [32].

When the temporal structure of the pump wave varies on a time scale comparable to or shorter than the steady-state time given in equation 3.14, transient effects must be taken into account. Physically, when  $\tau_L \approx t_{SS}$ , the inertia of molecular response leads to a damping of the stimulated vibrations and the efficiency of stimulated scattering is reduced [52]. On the other hand, the difference in group velocity results in distortion of the relative phase between pump and Stokes wave therefore leading to their temporal separation, thus limiting the effective interaction length [33].

In the extreme transient regime, when  $\tau_L \ll T_2$  and when the incident Stokes pulse has the same functional form as the pump, an analytic expression for the Stokes intensity can be found [40]:

$$I_S(z, t) = I_S(0, t) I_0^2(u(z, t)) \quad (3.17)$$

where  $I_0$  is a modified Bessel function and

$$u(z, t) = \sqrt{2g_{SS}\Gamma_R z \int_{-\infty}^t I_L(t') dt'}. \quad (3.18)$$

The steady-state gain  $g_{SS}$  is given by equation 3.11.

When the conditions for equation 3.17 are valid, the solution can be approximated for values of  $u$  greater than about 3, corresponding to an intensity amplification of about 24, within the first term in the asymptotic expansion [40]:

$$I_S(z, t) = I_S(0, t) \frac{e^{2u}}{2\pi u}. \quad (3.19)$$

This solution is useful for modeling the approximate properties of transient interactions. However, in most practical situations the incident pump and Stokes pulses do not have the same functional form, and the more general integral solution of equations 3.8 must be used for accurate results, taking into account the specific variation of the Stokes phase and amplitude and the relative timing between the incident pump and Stokes pulses.

The main conclusion is that a transient gain, in opposite to the steady-state gain, *does not* depend on the inverse of the line width for the Raman transition, but depends on the Raman cross-section. It follows that for transient Raman scattering, a high value of integrated Raman cross-section is desirable. Furthermore, transient Raman amplification is proportional to the square root of the integral intensity of the pump pulse, and not to the instantaneous pump intensity.

### 3.1.3 Impulsive SRS

If the duration of the laser pulse is comparable or shorter than the molecular vibrational period  $\tau_L < T_R = 2\pi\omega_R^{-1}$ , a very specific behavior of the SRS process is observed. The nature of the non-stationarity originates from the transient character of the buildup of the vibrational response itself. Within the short time  $\tau_L$ , a quantum oscillator has no time to exhibit its vibrational properties, and therefore it cannot be resonantly driven by the laser field. On the other hand, the spectrum of the pulse initially contains frequency components necessary for the SRS process to occur, and thus a sort of nonlinear self-conversion can take place in the forward direction at field intensities much lower than the threshold values for SRS buildup starting from spontaneous noise.

Experiments on frequency conversion in the regime of impulsive SRS (ISRS) in

gaseous SF<sub>6</sub> [26] showed that the scattering process is not sensitive to the Raman line structure. A continuous (pressure-dependent) shift of the pulse central frequency towards lower frequencies was observed. The self-frequency conversion results from the transient process induced by a sudden excitation of nuclear motion and depends on the entire laser-molecule interaction history.

For an insight into the physics underlying the ISRS process, the regime, where the pulse duration  $\tau_p \ll T_R$ , is considered [26]. Under these conditions the terms  $\omega_R^2 Q$  and  $\Gamma_R \frac{\partial Q}{\partial t}$  in equation 3.4 can be neglected in comparison to the rapidly changing term  $\frac{\partial^2 Q}{\partial t^2}$ . Assuming that the laser pulse appears at the moment  $t = 0$  and is nonzero within the time interval  $0 < t < \tau_p$ , the vibrational coordinates change as

$$Q(t) \approx \frac{1}{2m} \frac{\partial \alpha}{\partial Q} \int_0^t dt' \int_0^{t'} dt'' E^2(t'') \quad (3.20)$$

and show a very slow response to the field. After the interaction, e.g., for  $t > \tau_p$ , the nuclear coordinate exhibits freely damped oscillations,

$$Q(t) \approx Q_0 \exp(-t/T_2) \sin(\tilde{\omega}_R t), \quad (3.21)$$

with a frequency  $\tilde{\omega}_R^2 = \omega_R^2 - (1/T_2)^2$ , and an amplitude  $Q_0 = (2\pi M c \omega_R) (\frac{\partial \alpha}{\partial Q}) W$  proportional to the pulse full energy  $W = (c/4\pi) \int_{-\infty}^{\infty} E^2 dt$ .

In the regime of ultrashort-pulse-molecule interaction described by the molecular response 3.20, the change of the pulse instant frequency  $\dot{\phi}(z, \tau)$  with the propagation length  $z$  is described by the following equation:

$$\frac{d\dot{\phi}}{dz} = -\beta_{electr} \frac{\partial I}{\partial \tau} - \beta_{Raman} \int_{-\infty}^{\tau} I(\tau') d\tau', \quad (3.22)$$

where  $\beta_{electr} = 2\pi N \omega \chi_{electr}^{(3)} / cn$ ,  $\beta_{Raman} = 4\pi^2 N \omega (\partial \alpha / \partial Q)^2 / mc^2 n^2$ , and the laser pulse intensity  $I = (cn/8\pi) |E|^2$  is introduced.

As can be seen, the contribution due to the impulsive vibrational excitation (the second term in equation 3.22) appears as an additional red shift which increases monotonically from the leading to the trailing edge in proportion to the laser energy

passed through a given cross section. This picture leads to two characteristic features. First, the center of gravity of the pulse spectrum experiences a frequency down-shift with the propagation distance. Second, the combined action of the electronic Kerr effect, which produces the redshift at the leading edge and the blue shift at the trailing edge, and the inertial Raman contribution results in an enhancement of the red and suppression of the blue spectral components.

### 3.1.4 Competition of SRS with other nonlinear processes

The high intensity threshold of transient SRS favors the competing process of self-phase modulation (SPM), the efficiency of which is, in contrast to SRS, inversely proportional to the pulse duration. The efficiency of Raman conversion of short pulses is even more reduced by the group velocity mismatch between pump and Stokes waves caused by dispersion of the Raman medium. As a result, the dominant non-linear process in condensed media, when pumping with a usual Gaussian beam is femtosecond continuum ('white light') generation [33].

Focusing ultrashort laser pulses of high peak power ( $\sim 10^5$  W) into the medium with a positive intensity-dependent refractive index coefficient ( $n_2 > 0$ ) very often results in self-focusing process (or *Kerr-lensing*) [32]. This effect causes a spatial collapse of the laser beam (filament formation) when it propagates through the transparent optical materials and can lead to optical damage. Self-focusing is a consequence of the nonuniform spatial profile of the laser beam. In thick media self-lensing of a Gaussian beam overcomes diffraction for a distinct threshold power (self-focusing threshold), approximately given by equation 3.23 [53]:

$$P_{cr} \approx \frac{a\lambda^2}{8\pi n_2 n_0}. \quad (3.23)$$

For fused silica and pump pulses of 594.5 nm,  $P_{cr}$  is about  $5 \cdot 10^5$  W [32].

In the filaments efficient longitudinally phase-matched, transversally non-phase-matched parametric four-photon interaction (self-phase modulation), stimulated Raman scattering, laser and Raman induced parametric four-photon interaction (cross-phase modulation) and cascading frequency conversion occur [32], leading, as men-

tioned above, to spectral superbroadening of femtosecond pulses (white-light generation)

A method for overcoming the problem of SRS suppression in the presence of competing processes is presented in the next section.

### 3.1.5 Bessel beam pumping

One of the striking features of a Bessel beam [54] is its superluminal group velocity [55–57]. A Bessel beam can be viewed as a set of infinitely plane waves with wave vectors crossing the propagation axis under a given angle  $\gamma$  thus forming a cone. The mutual interference of these plane waves yields an intensity maximum which propagates along the cone axis with a group velocity  $U = c/\cos\gamma$ , exceeding the group velocity  $c$  of light in the same medium. Consequently, by adjusting the cone angle,  $U$  can be tuned to match the group velocity of a red-shifted pulse in a medium with normal dispersion.

Another important advantage of a Bessel pump beam upon a Gaussian beam is its robustness to SPM [58]. For any nonlinear process pumped by a Bessel beam the interaction of partial plane waves, constituting the beam, is non-collinear and is confined to a narrow and extended diffractionless region around the cone axis. One can expect that with this interaction geometry, SPM will be greatly reduced as the narrow high-intensity region around the axis is traversed obliquely by the partial plane waves. Consequently, the interaction length where the pumping radiation undergoes SPM is very small, typically a few tens of micrometers.

In order to analyze the tunability of the group velocity of a Bessel beam, it is important to note that the cone angle  $\gamma$  depends on the frequency. The group velocity  $U$  of a Bessel pulse can be defined as  $U = \partial\omega/\partial\beta$  where  $\beta = k \cos\gamma$  is the propagation constant of the Bessel beam [54] the wavenumber being defined usually as  $k = \omega/c$ . The group velocity of a Bessel pulse in the vacuum is thus

$$U = \frac{c}{\cos\gamma[1 - (\omega\partial\gamma/\partial\omega)\tan\gamma]}. \quad (3.24)$$

The term  $\omega\partial\gamma/\partial\omega$  in the denominator represents the tilting of the pulse front –



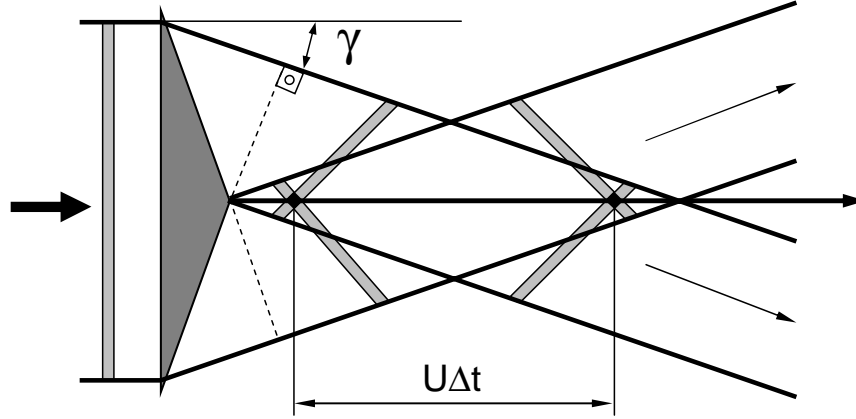


Figure 3.1: Group velocity of a Bessel pulse for a refractive axicon. Snapshots of the interference maximum on the axis produced by two tilted pulses for two instants separated by  $\Delta t$  are shown. Dashed lines perpendicular to the propagation directions indicate the phase fronts.

defined as the surface coinciding with the peak of the pulse – with respect to the phase front [59]. Tilting is caused by the angular dispersion, the tilting angle being given by  $\tan \alpha = -\omega \partial \gamma / \partial \omega$ . Equation 3.24 can be then written as

$$U = \frac{c \cos \alpha}{\cos(\gamma + \alpha)}. \quad (3.25)$$

For a refractive axicon [60] being characterized by a wedge angle  $\delta$  and a refractive index  $n$  the cone angle of the Bessel beam is determined by Snell's law,  $n \sin \delta = \sin(\gamma + \delta)$ , and the angular dispersion is given by  $\partial \gamma / \partial \omega = (\partial n / \partial \omega) \sin \delta / \cos(\gamma + \delta)$ . Here, the angular dispersion is positive (assuming  $\partial n / \partial \omega > 0$ ) and the tilt of the pulse front results in a superluminal Bessel pulse: 3.25 yields  $U > c / \cos \gamma$  (see Fig. 3.1).

Equation 3.25 and its illustration are given for a Bessel pulse in the vacuum. Inside a dispersive medium, the picture is slightly modified by the refraction at the medium interface, but it is easily seen that the above mentioned conclusions concerning the peculiar behavior of the group velocity remains valid.

## 3.2 Raman media

Raman-active media include solids, liquids, gases and plasmas. Gases have long been preferably used as Raman media, mainly due to their higher threshold for self-focusing and low scattering losses. They are undoubtedly very attractive media when low repetition-rates (usually  $<50$  Hz) and high peak power pump sources are used, and when the requirement of a pressure vessel is not a practical problem. The mostly used Raman media gases are  $H_2$ ,  $D_2$  and  $CH_4$ . These media offer large Raman shifts (up to  $4150\text{ cm}^{-1}$  for  $H_2$ ) and are used in various configurations for effective frequency conversion, e.g. of high peak power pulsed lasers. Nevertheless, the application of gas-based devices is limited due to their poor repetition-rate scaling, low gain, optical breakdown and their large geometrical size.

In contrast, liquid Raman-active media are not widely used. However, there are very few reports of liquids being used for frequency conversion. Some reasons for this include toxicity of the materials, volatility and a high incidence of absorption bands in the visible and near infrared. Some of the best results using liquid media were obtained using liquid nitrogen.

Optical fibers are attractive media for SRS as they enable high pump intensities to be maintained over long interaction lengths. A major recent advance in SRS-based devices was the use of fiber Bragg gratings to produce Raman amplification at the telecommunication wavelengths of  $1.3$  and  $1.5\mu\text{m}$ . Optical fiber-based SRS is limited in its application by the transmission of silica fiber ( $<2\mu\text{m}$ ), the fixed frequency shift of silica ( $440\text{--}470\text{ cm}^{-1}$ ) and the lack of access to the resonator, e.g. for intracavity SHG. However, there are strong opportunities for applications in telecommunication, and diode-pumped fiber Raman laser sources in the near infrared are now available commercially [48].

The first observations of SRS in crystalline media were made in 1963, when Eckhardt et al. observed SRS in diamond, calcite and sulfur [61]. However, SRS in crystalline media remained a curiosity until around 1977 when Ammann et al. [62] reported very efficient (77%) frequency conversion of an Nd laser using SRS in crystalline  $LiIO_3$ . Now, with the availability of high-optical-quality Raman crystals, well

established all-solid-state laser technology, and the demand for practical sources with wavelengths not directly achievable from solid-state lasers, there is a great deal of scope both for investigating broad scientific issues and for developing practical, robust sources based on SRS in crystals (see, e.g, [63]). Recent advances show considerable potential for a new generation of laser devices based on SRS in crystals. A wide variety of experimental configurations have been used to demonstrate Raman frequency conversion.

The most promising crystals for Raman shifting which have been reported in the literature to date are  $\text{LiIO}_3$ ,  $\text{Ba}(\text{NO}_3)_2$  and a variety of tungstate crystals. Other solids in which SRS has been observed are listed in Refs. [64,65]. Of particular use is reference [65] which provides data on a wide variety of crystals for different orientations. In general, crystals with the highest Raman activity tend to contain molecular groups with strong covalent bonding such as carbonates, nitrates and tungstates [66]. Typically, the strongest Raman transitions correspond to totally symmetric "breathing" molecular vibrational modes.

The development of high gain solid state Raman materials results in the additional capability of intracavity solid state Raman lasers based on coupled resonator or shared resonator designs. Along with the obvious advantages of solid state technology (compact, rugged, low maintenance, etc.), the intracavity configuration can take advantage of the third-order nonlinear nature of the stimulated Raman process providing special operating characteristics such as spatial beam clean-up and pulse-width control through nonlinear cavity dumping [22].

In the experiments, presented within this work, Raman conversion in potassium gadolinium tungstate  $\text{KGd}(\text{WO}_4)_2$  (KGW) was observed. This crystal has a monoclinic structure and two optical axes. The vibrations of  $\text{WO}_4^{2-}$  ions result in strong Raman peaks at  $767.5 \text{ cm}^{-1}$  and  $901.5 \text{ cm}^{-1}$ . KGW has been widely used for frequency conversion, and is usually oriented for propagation along the  $b$ -axis (which corresponds to the optical  $N_p$ -axis). The  $901.5 \text{ cm}^{-1}$  mode is dominant in case of electric field of the Raman excitation laser  $\mathbf{E}$  being perpendicular to the  $c$ -axis and the  $767.5 \text{ cm}^{-1}$  mode is dominant for  $\mathbf{E}$  chosen to be perpendicular to the  $a$ -axis. The physical and optical properties of KGW are described in detail in Ref. [67], and some key properties are summarized in table 3.1.

Table 3.1: Material properties of a KGd(WO<sub>4</sub>)<sub>2</sub> crystal.

transmission range / $\mu\text{m}$	0.35-5.5	
density / $\text{g cm}^3$	7.17	
crystal symmetry	monoclinic	
orientations	p[mm]p	p[gg]p
refractive index at 300 K	1.986	2.033
Raman shift at 300 K / $\text{cm}^{-1}$	901	768
spontaneous Raman line width / $\text{cm}^{-1}$	5.9	7.8
Raman gain with 1064 nm pump / $\text{cm GW}^{-1}$	3.3	4.4

### 3.3 Experimental setup

To perform the Raman conversion experiments within this thesis the output of one of the OPG described in chapter 2.3 was used. The OPG output pulses were centered at  $\sim 570$  nm and had energies of typically  $\sim 10$   $\mu\text{J}$ , with a pulse duration of  $\sim 70$  fs. Raman generation was achieved by focusing the OPG beam by means of an axicon with an angle of  $\delta = 15^\circ$  in a KGW crystal of 4 mm length, oriented along the (010) crystallographic axis. The distance between the axicon edge and the crystal surface could be varied in order to obtain the best performance. Output radiation was collimated with a focusing lens and sent to a spectrometer equipped with a liquid nitrogen-cooled CCD camera for spectral analysis or to a powermeter for power measurements, respectively. Different spatial parts of the output radiation could be investigated separately by using a pinhole before the focusing lens (Fig. 3.2).

The OPG pump pulses were not exactly bandwidth limited. The pump spectrum was slightly asymmetric, with additional low-amplitude maxima evident on a logarithmic scale. The full bandwidth of this spectrum at the base was  $\sim 1700$   $\text{cm}^{-1}$  (see Fig. 3.3 and yellow curve in Fig. 3.6), which is larger than the highest Raman shift due to a vibration in a KGW crystal. This means that the conditions of the experiment are close to those deduced theoretically for ISRS.

The axicon, used in the experiments was manufactured in the optical workshop of the Institute of Physics in Minsk. A photo of the the axicon is presented in Fig. 3.4

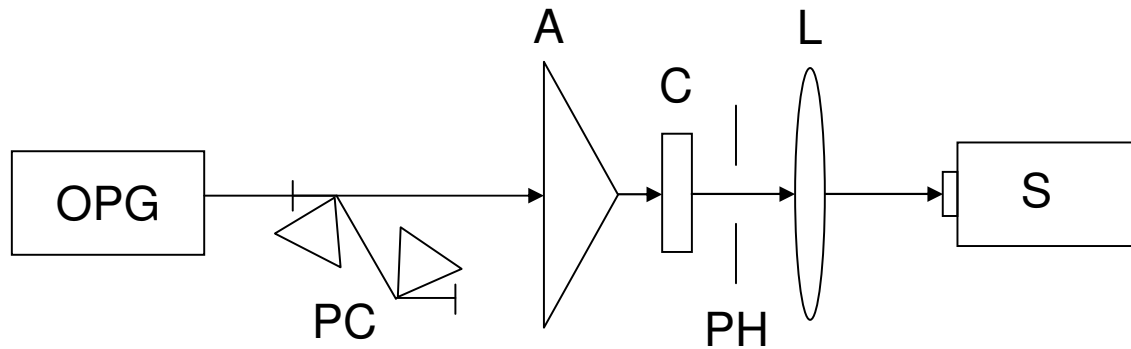


Figure 3.2: Scheme of the Bessel-pump ISRS experiment. PC: double-pass prism compressor; A: Bessel lens (axicon); C: KGW crystal, variable position along the optical axis; PH: pinhole; L: focusing lens; S: detector (spectrometer/powermeter).

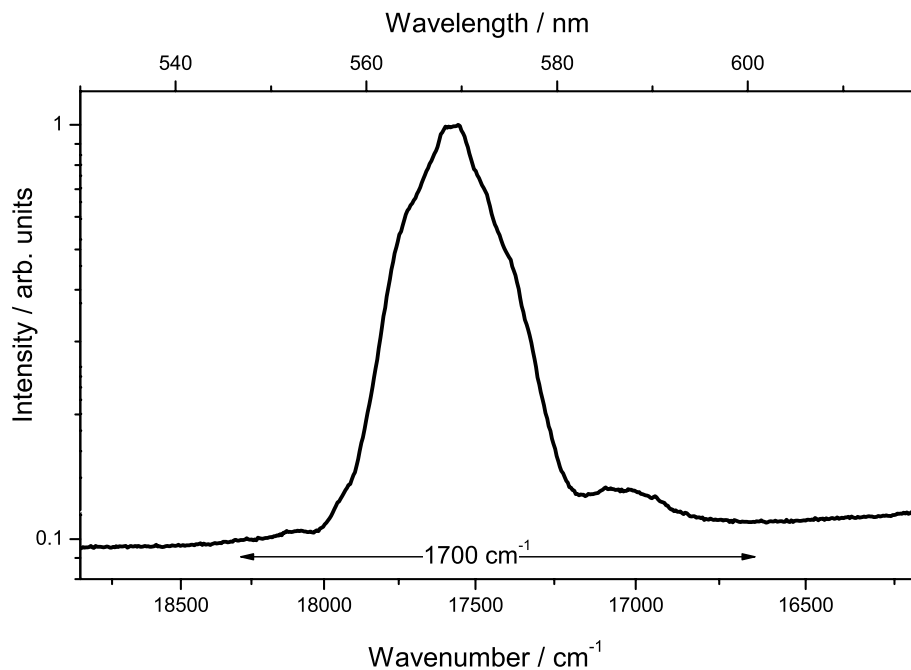


Figure 3.3: Spectrum of OPG radiation used in ISRS experiments. Intensity is shown in logarithmic scale.

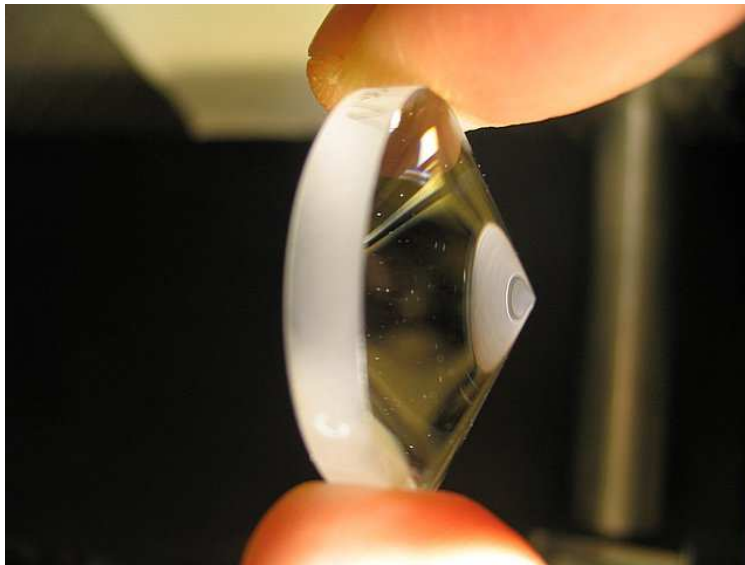


Figure 3.4: A photo of the axicon used in Bessel-pump ISRS experiments

### 3.4 Results and discussion

A beam picture observed on the screen, placed at the distance of around 1 m from the KGW crystal along the beam axis, contains rings and a central spot of different colors (Fig. 3.5). A red central beam (axial S) represents the generated Stokes radiation. This beam is spatially separated from the pump beam, which propagates as a cone. Spatial separation of the generated and the pump beams is especially useful in ISRS, where the broadband pump and Raman-converted radiation usually overlap spectrally. A yellow-red cone beam consists of an output pump P and Stokes-shifted contributions S overlapping in space. Two additional cone beams having green and blue colors that occur at larger angles could also be observed; in analogy to conventional SRS experiments they can be identified as the first and second anti-Stokes beams (1st aS and 2nd aS, respectively) that are due to spectral shifts towards wavelengths shorter than the pump spectrum (see also Ref. [68]). Although Stokes radiation is generated in the cone and the axis directions [34], only radiation generated along the axis was considered in our measurements.

The spectra of the input pump and of the Raman-converted axial radiation, the first and the second anti-Stokes cone radiation, are shown in Fig. 3.6.

The spectrum of the central beam is Stokes shifted relative to that of the pump beam. The distinguishing features of these results are the broad spectral bandwidth of the Stokes-shifted radiation ( $\sim 800 \text{ cm}^{-1}$  FWHM) and a strong deviation of the observed spectral Stokes and anti-Stokes maxima from the known Raman lines. These results are characteristic of Raman frequency conversion in the ISRS regime [26, 69]. The tendency of increasing the spectral bandwidth of the axial Raman-shifted radiation with increasing pump level is demonstrated in Fig. 3.7.

Taking the threshold energy value as a unity, the relative pump energies for the curves a, b, c, d, e, f, and g are 1, 1, 3, 4.5, 6.5, 10, and 11.5, respectively. Near threshold, when the ISRS generation is unstable, the spectrum is concentrated in the Stokes-shifted region, with a maximum (curve b) corresponding to a wave number shift of  $901 \text{ cm}^{-1}$ . Increasing the pump level results in a shift of the maximum position to longer wavelengths and impressive growth of the bandwidth with predominantly spectral broadening to the Stokes region.

The influence of the pump energy on the bandwidth value (full width at the base) for the axial radiation is shown in Fig. 3.8. The theory developed in Ref. [69] predicts a linear increase of the bandwidth for the Raman-converted radiation. As can be seen, the experimental data reproducing the initial part of the curve are well approximated by the linear dependence (solid line in Fig. 3.8). For energies of more than  $2.5 \mu\text{J}$  this dependence is saturated.

The inset of Fig. 3.8 shows the dependence of the Raman-converted axial radiation on the pump power in the KGW crystal. The maximum value for the power of the converted radiation is  $6 \mu\text{W}$ , which corresponds to a pulse energy of  $6 \text{ nJ}$ . The estimated maximum conversion efficiency obtained in our experiments for radiation converted in the axial direction was nearly 1%. The energy of the axial pulses was enough for second-harmonic generation in a  $\beta$ -barium borate crystal of  $0.5 \text{ mm}$  length. No white-light generation was observed in the experiments. Saturation of the Stokes power dependence on pump power shows that there is no operation near Raman threshold causing the low conversion efficiency in this experiment.

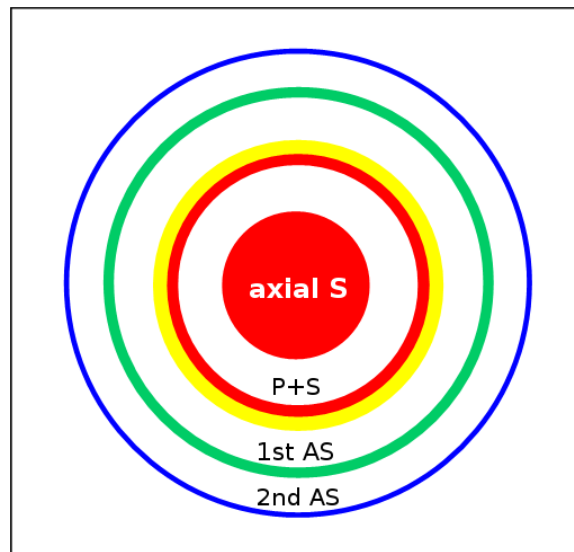


Figure 3.5: Output beams observed on the screen in the far zone of a Raman converter (schematic reproduction).

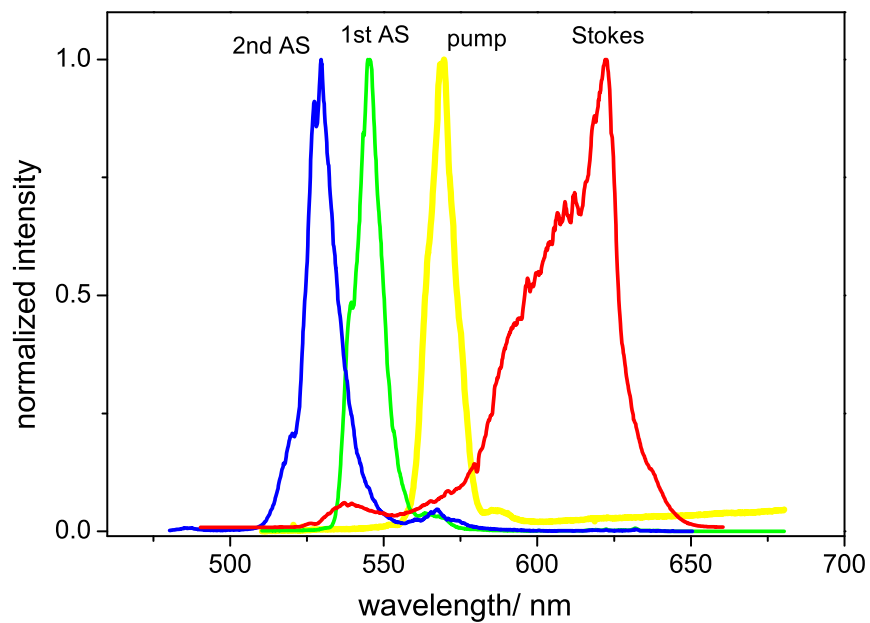


Figure 3.6: Measured spectra for the light beams participating in Raman conversion: pump, spectrum of the pump beam; Stokes, spectrum of Raman-converted radiation in the axial direction; 1st AS, spectrum of the ring generated first anti-Stokes beam; 2nd AS, spectrum of the ring generated second anti-Stokes beam.



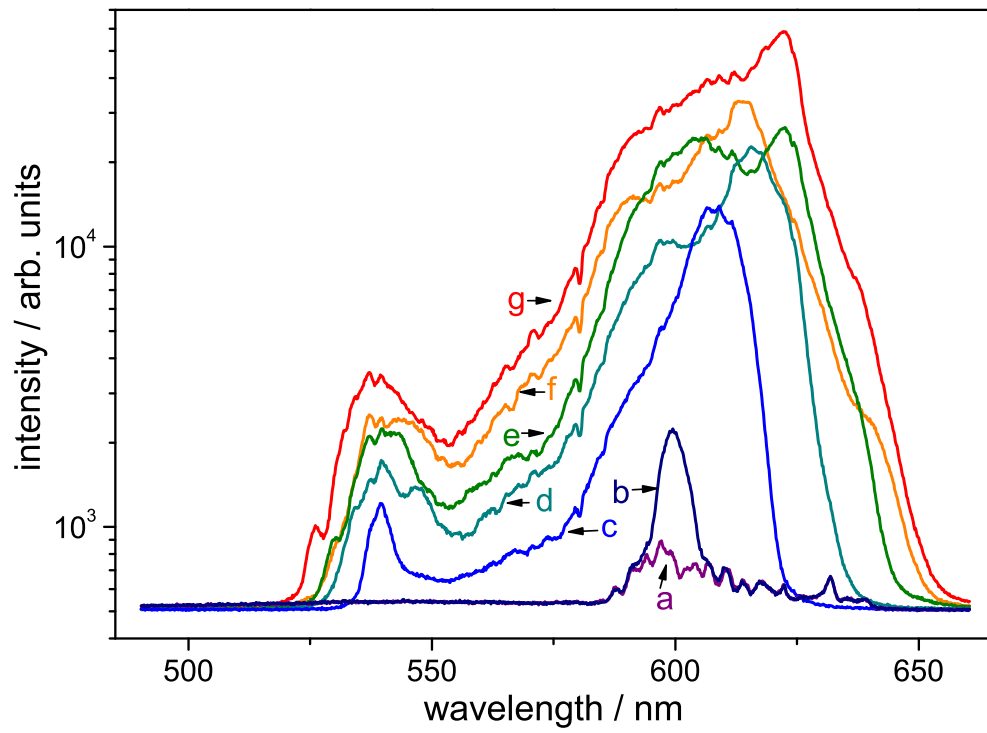


Figure 3.7: Spectral evolution of the axial Raman converted beam with increasing pump level.

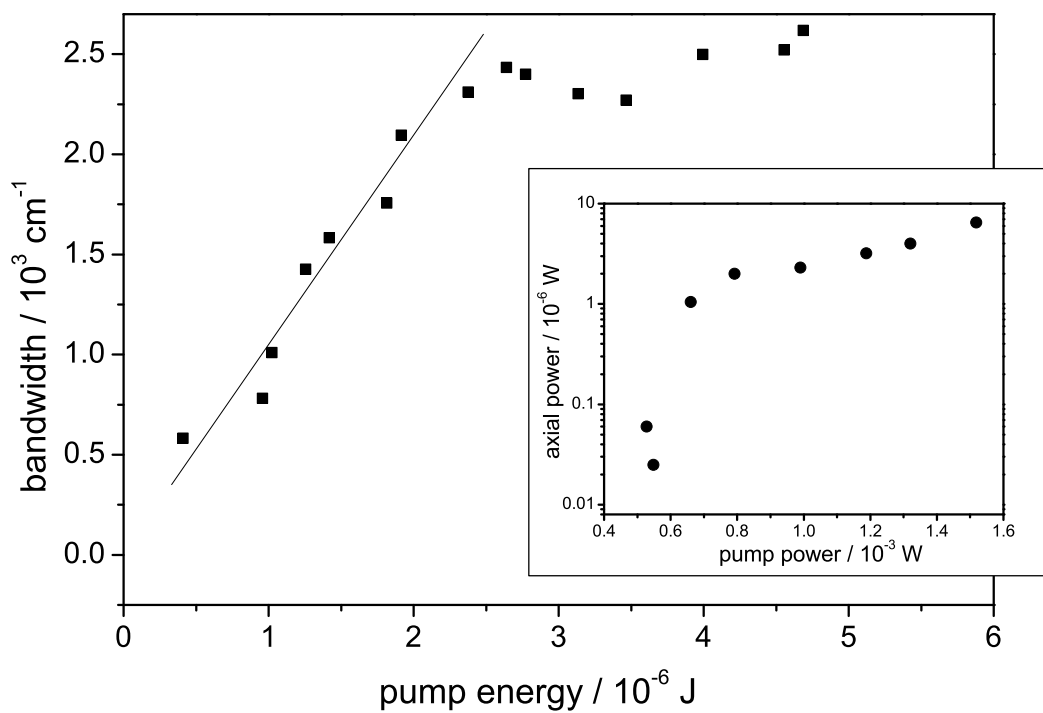


Figure 3.8: Dependence of the spectral bandwidth of the axial Raman-converted beam on pump energy. Inset, dependence of the axial Raman-shifted power on the pump power.

Temporal cross-correlation measurements for the axial Raman-converted radiation showed that the correlation trace has a complicated shape with a temporal pulse duration at the base  $\sim 200$  fs. It is expected, that by applying to the generated radiation conventional pulse compression and shaping techniques it could be possible to synthesize theoretically predicted by Nazarkin et al. [35] fs- and sub-pulse trains as well as single compressed pulses.

### 3.5 Conclusion

In this chapter the theoretical background of stimulated Raman scattering (SRS) on different time scales was presented along with the description of the first experiment for Raman conversion of femtosecond laser radiation in a solid-state medium (KGW crystal). The regime of impulsive SRS (ISRS) was achieved in the experiments presented here by using laser pulses with a temporal duration comparable to a vibrational period of the medium. Bessel-beam pumping allowed for suppression of continuum generation and compensation of the group velocity mismatch thus increasing efficiency of Raman frequency conversion.



## Chapter 4

# Spectral superbroadening of fs pulses in microstructure fibers

Microstructure (MS) [70–72] and tapered [73] fibers have opened a new phase in supercontinuum (SC) generation research, offering new approaches to study and to enhance this physical process and giving rise to numerous applications of SC emission in various areas of modern science [74]. Such fibers are ideally suited for controlling and transforming the spectra of ultra-short laser pulses, as they provide a large degree of light localization within the fiber core [75] and allow for dispersion to be tailored by modifying the geometry of the fiber cross section and changing the air-filling fraction of the fiber cladding [76]. The ability of microstructure and tapered fibers to enhance SC generation, leading to a considerable spectral broadening of even unamplified femtosecond pulses, has recently resulted in major breakthroughs in optical metrology, changing the paradigm of high-precision frequency measurements [77, 78]. Supercontinuum-generating microstructure and tapered fibers offer new elegant solutions in ultrafast [79] and biomedical optics [80], giving an access to the absolute phase of few-cycle laser pulses [81].

Investigations of the nonlinear optical processes contributing to supercontinuum generation have provided deeper insights into many fundamental aspects of classical

nonlinear optics, resulting in the demonstration of several interesting physical effects, such as soliton fission [82], Cerenkov-phase-matched third-harmonic generation [83], and multiply phase-matched wave mixing [84]. The analysis of supercontinuum-generating modes of microstructure-integrated fiber arrays has revealed the important role of mode coupling in MS fiber arrays employed to transform the spectra of ultrashort laser pulses [85]. These experiments lead to a better understanding of fundamental physical issues related to light localization in micro- and nanostructured matter. Potentially, broadband emission efficiently produced in such fibers, with the spectrum sometimes spanning a couple of octaves, is also very promising for numerous spectroscopic applications [86]. However, the spectral energy density of such a broadband emission source is usually too low to offer a practical alternative to much more expensive, but much more powerful, optical parametric amplifiers and dye lasers as far as spectroscopic, especially nonlinear optical, applications are concerned.

In this chapter, a new design of a multiple core microstructure fiber is demonstrated, suggesting an alternative approach to produce broadband emission with a higher output energy through simultaneous SC generation in several fiber cores [87]. Based on theoretical analysis, it is demonstrated here that the waveguide enhancement factor for a broad class of nonlinear-optical processes contributing to SC generation reaches its maximum at a certain optimal value of the fiber core size, corresponding to the maximum ratio of the fiber core-confined laser power to the fiber-core diameter. Such optimal values of the fiber-core size fall within the submicron range for fused silica- air MS fibers. The results of the experimental studies are fully consistent with theoretical predictions, showing that the efficiency of SC generation achieved with MS fiber cores with a diameter of  $0.8 \mu\text{m}$  is much higher than the SC generation efficiency attainable with  $3\text{-}\mu\text{m}$ -core-diameter MS fibers. It is also shown, that parametric four-wave mixing, phase matched and enhanced in higher-order modes of MS fibers can be used for efficient anti-Stokes frequency conversion of low-energy ultrashort laser pulses [88].

## 4.1 Theory

### 4.1.1 Spectral superbroadening of fs laser pulses

As mentioned in section 3.1.4, focusing of the ultrashort laser pulses of high peak power into the condensed medium can result in spectral superbroadening, also termed as *supercontinuum* generation or *white-light* generation. One of the first observations of spectral superbroadening from  $\sim 400$  to  $\sim 800$  nm in gases was performed in 1986 [89], where dye laser pulses of 70 fs and 2 ps duration centered at 600 nm were focused in Xe and N<sub>2</sub> gases at pressure of 30 atm.

Self-transformation of the pulse shape and spectral broadening are the result of the strong nonlinear-optical interaction of the light field with the medium, which takes place under the conditions of high localization of the radiation both in space and time. There might be several ways to localize the light field inside a medium. One possible way is to take advantage of an optical device. With such devices as capillaries, microstructured fibers, and photonic crystals it is possible to govern the mode dispersion and to achieve high localization of the light field at comparatively long interaction distances (see e.g. [90–92]).

One of the first explanations of ultrashort laser pulse spectrum transformation was achieved on the basis of a simple model, in which the maximum relative broadening  $\Delta\omega/\omega$  was directly proportional to the pulse intensity in the medium with instantaneous Kerr nonlinearity [93]. The frequency deviation

$$\delta\omega(\tau) = -kz\partial\Delta n/\partial\tau \quad (4.1)$$

is symmetric relative to the peak of the pulse. Here,  $\Delta n$  is the nonlinear contribution to the refractive index,  $\tau$  is the pulse duration,  $z$  is the propagation coordinate, and  $k$  is the wavenumber. Therefore, the spectral broadening is also symmetric relative to the laser central frequency. In this model the radiation is considered to be a plane wave with a given temporal distribution. The spatial distribution of the radiation in the transverse direction was not taken into account. Later on, it was concluded that self-focusing played an essential role in spectral superbroadening [89, 94].

Indeed, the simple self-phase-modulation model, which neglects spatial effects, could not explain the increase of the spectral width  $\Delta\omega$  up to several hundred nanometers, as observed in the experiments.

Further experimental studies have shown that not only self-focusing but also geometrical focusing of the pulse into the medium influences the width of the frequency spectrum [95]. At the same time, free-electron generation contributes essentially to the spectral transformation. The frequency deviation (4.1) is positive due to the negative contribution to the refractive index  $\Delta n$  from the free electrons, whose spacial density grows during the pulse duration. The spectral broadening is asymmetric and blue shifted relatively to the laser central frequency [96, 97]. Ionization and optical breakdown (the latter often follows the ionization in dense gases or condensed media) strongly depend on the pulse peak intensity.

In the conditions of tight focusing of the radiation into the medium, where the third-order nonlinear susceptibility is comparatively low (e.g. in the noble gases), the major contribution to the spectral transformation comes from the free electrons. Under the conditions of a strong localization of energy that enables one to obtain an efficient redistribution of input laser pulse energy into the supercontinuum energy, there exists an additional mechanism that enhances the blue part of the pulse spectrum [98]. This mechanism is temporal self-steepening of the radiation and shock-wave formation at the trailing edge of the pulse. As a result, the positive frequency deviation  $\delta\omega(\tau)$  at the back of the pulse is larger than the absolute value of the negative frequency deviation at the front of the pulse. The spectrum acquires a large blue pedestal due to a purely positive nonlinear contribution to the refractive index from the Kerr nonlinearity [99–101]. The effect is stronger when the input pulse duration is shorter. Self-steepening of the pulse can explain the formation of the blue spectral wing during the propagation of ultrashort pulses through microstructured fibers [102]. In these optical devices a steep trailing edge of the sub-pulse formed inside the fiber may originate due to the joint influence of higher-order dispersion terms ( $\geq 3$ ) and the Kerr nonlinearity.

In summary, the effect of various physical mechanisms on spectral broadening can be interpreted in terms of spatio-temporal self-phase modulation. Indeed, for the



instantaneous electronic Kerr response, the nonlinear phase is directly proportional to the intensity. In the case of free-electron generation, the electron density, growing as a function of the intensity, influences the nonlinear phase through the plasma contribution to the refractive index. Stimulated Raman scattering on rotational transitions in molecular gases results in the delayed response of the Kerr nonlinearity and also leads to the intensity-dependent phase of the pulse. Self-steepening increases the nonlinear phase gradients through the increase of intensity gradients on the pulse fronts. Such mechanisms as self-focusing and ionization not only affect the longitudinal but also the transverse electric field distribution and, therefore, the transverse spatial phase of the pulse. This gives rise to such phenomena as supercontinuum conical emission [103].

### 4.1.2 Limiting enhancement of nonlinear-optical processes in small-core microstructure fibers

Microstructure and tapered fibers owe their ability to enhance nonlinear-optical processes to dispersion tunability, high degrees of light confinement, and waveguide geometry factors, such as large interaction lengths and small pump-beam sizes attainable with these fibers. Figure 4.1 presents the group-velocity dispersion calculated as a function of radiation wavelength for fibers consisting of a small fused-silica core and air cladding. Such group-velocity dispersion profiles are typical of waist regions in tapered fibers [73]. This model allows for qualitative understanding of dispersion properties of submicron fused-silica thread-like cores in MS fibers used in the SC generation experiments. Many remarkable examples of dispersion tunability can be found in the recent literature on MS fibers (see e.g. [76]). Here, main attention will be paid to the issues related to light confinement and waveguide geometry factors leading to the enhancement of nonlinear optical interactions. In particular, the possibility of approaching the physical limit in waveguide enhancement of nonlinear optical processes using small-core high-refractive-index-step fibers will be demonstrated.

The use of optical fibers is a natural way to increase the interaction length and to reduce the beam diameter of the light fields involved in the nonlinear processes.

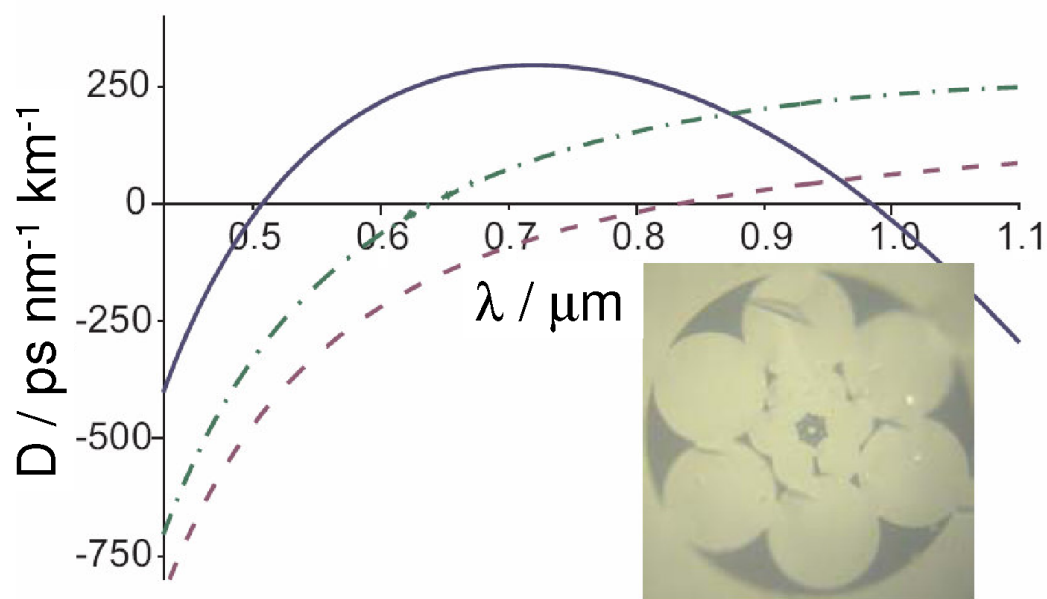


Figure 4.1: Group-velocity dispersion calculated as a function of radiation wavelength  $\lambda$  for fibers consisting of a fused-silica core with a diameter of (1) 0.8, (2) 1.5, and (3) 3  $\mu\text{m}$  and air cladding. The inset shows the cross section of a multiple-core microstructure fiber. The central core has a diameter of about 5  $\mu\text{m}$ . The diameter of six smaller thread-like cores surrounding the central core is 0.8  $\mu\text{m}$ .

These two factors underlie a successful and rapidly growing area of nonlinear fiber optics [104], substantially improving the efficiency of many nonlinear optical processes. The product  $Il_{eff}$ , where  $I$  is the light field intensity in an optical fiber, and  $l_{eff}$  is the effective interaction length, gives a figure of merit for the efficiency of a broad class of nonlinear optical interactions. These include self- and cross-phase modulation, stimulated Raman scattering, and certain types of parametric wave-mixing processes. The waveguide enhancement of a nonlinear optical process with respect to the regime of tightly focused pump beams can be estimated by calculating the ratio of the products  $(Il_{eff})_f$  and  $(Il_{eff})_t$  determined for these two cases. The standard approach [104] gives the following expression for the figure of merit as defined above:

$$\xi = \frac{(Il_{eff})_f}{(Il_{eff})_t} \approx \frac{\lambda}{\pi r_0^2 \alpha}, \quad (4.2)$$

where  $\lambda$  is the radiation wavelength,  $\alpha$  is the magnitude of fiber losses, and  $r_0$  is the radius of the guided mode.

From 4.2 it is straightforward to see that the waveguide enhancement factor scales as  $r_0^2$  as a function of the waveguide mode size. This simple argument, along with dispersion tunability, explains why microstructure and tapered fibers are so efficient in enhancing nonlinear optical processes. However, the mode size  $r_0$  cannot be made infinitely small by reducing the fiber core. The physical limit is, of course, determined by the radiation wavelength. As the fiber-core radius becomes smaller and smaller, less and less radiation power remains confined within the fiber core. This factor is quantified in the theory of optical fibers [105] through the parameter  $\eta$ , defined as the ratio of the laser power confined in the fiber core and the total laser power guided by a fiber mode. When the fiber-core radius becomes very small, as is often the case with MS and tapered fibers, the pump laser power confined to the fiber core decreases, reducing the efficiency of nonlinear-optical processes. To include this factor into the consideration, one can modify 4.2 for the figure of merit characterizing the waveguide enhancement of nonlinear optical processes by representing it as

$$\xi \approx \frac{\lambda \eta}{\pi a^2 \alpha}, \quad (4.3)$$

where  $a$  is the radius of the fiber core. The fact that the parameter  $\eta$  falls with a decrease in the fiber-core radius  $a$  implies that the factor  $\xi$  described by 4.3 may become a non-monotonic function of  $a$ , reaching its maximum at a certain value of the optimal fiber-core radius.

To estimate the figure of merit for the efficiency of nonlinear-optical processes provided by the central core and the smaller, thread-like cores of a microstructure fiber, a model of a fiber with a fused-silica core and air cladding will be considered. The approximation of a weakly guiding fiber will be used to provide some order-of-magnitude estimates, although this approach is not fully justifiable in the case of a fiber with a fused-silica core and air cladding (the parameter  $\Delta = (n_{co}^2 - n_{cl}^2)/2n_{co}^2$  is estimated to be approximately 0.26 for such a fiber). The dimensionless frequency  $V = ka(n_{co}^2 - n_{cl}^2)^{1/2}$ , with  $k = 2\pi/\lambda$ , ranges from 2.5 to 230 for fiber-core radii of 400  $\mu\text{m}$  and wavelengths falling within the range of 310  $\mu\text{m}$ . In the limiting case of  $V \gg 1$ , the factor  $\eta$  for the fundamental guided mode is given by the following asymptotic expression [105]:

$$\eta \approx 1 - \frac{u^2}{V^3}, \quad (4.4)$$

where  $u$  is the eigenvalue of the dispersion equation for the fiber mode.

Now, the optimal value of the fiber-core radius  $a_{opt}$  can be roughly estimated by inserting the factor  $\eta$  defined by 4.4 into 4.3, differentiating it with respect to  $a$ , and equating the resulting expression to zero. This procedure yields

$$a_{opt} = (5/2\kappa)^{1/3}\lambda, \quad (4.5)$$

where  $\kappa = u^2/[(2\pi)^3(n_{co}^2 - n_{cl}^2)^{3/2}]$ . With  $u \approx 2.4$ , one finds that  $a_{opt} \approx 0.37\lambda$ .

Equation 4.5 can give, of course, only a very rough, order-of-magnitude estimate of the optimal value of the fiber-core radius. Moreover, this expression has been derived using 4.4, which is a good approximation only in the limiting case of  $V \gg 1$ , when diffraction effects are weak and most of the guided radiation energy is concentrated in the fiber core. The accuracy of equation 4.5 can be judged by comparing its prediction for the waveguide enhancement factor  $\xi$  with the results of a full analysis of light

confinement in the fiber core [106], performed with the use of a more accurate, but much more complicated and, therefore, less illustrative expression for the factor  $\eta$ . Such a comparison is provided in Fig. 4.2.

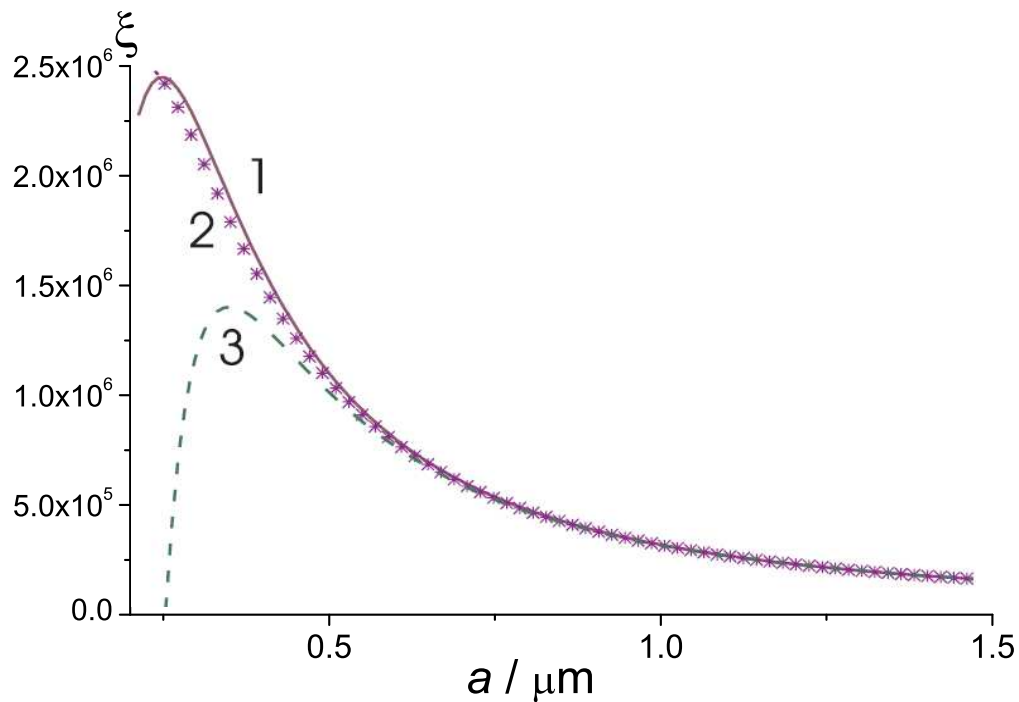


Figure 4.2: The factor  $\xi$ , characterizing the waveguide enhancement of nonlinear optical processes for radiation with the wavelength of  $1 \mu\text{m}$ , calculated as a function of the fiber-core radius  $a$  for a fiber with the refractive index of the fiber core  $n_{co} \approx 1.45$  and the refractive index of the cladding  $n_{cl} \approx 1$ : (curve **1**) the result of a full analysis of light confinement in the fiber core with no simplifying assumptions on the factor  $\eta$  and (curves **2** and **3**) predictions of equations 4.3 and 4.4 with the mode parameter  $u$  found by solving the mode characteristic equation (curve **2**, asterisks) and with  $u \approx 2.4$  (curve **3**).

One exciting consequence that follows from equations 4.3 and 4.5 is that submicron threads of silica surrounded by air, providing maximum  $\Delta$  values for fused-silica fiber structures, allow the limiting waveguide enhancement factors  $\xi$  attainable with fused-silica fibers to be attacked. This result is physically clear and instructive as higher refractive-index steps provide higher degrees of light localization, leading to

smaller optimal core sizes (see equation 4.5) and higher radiation intensities confined to the fiber core, eventually enhancing nonlinear-optical processes. Formula 4.5 also shows that fibers with submicron cores would be necessary to approach the limiting values of the figure of merit  $\xi$  for the efficiency of nonlinear-optical processes. This consideration of the waveguide figure of merit  $\xi$ , supplemented by the analysis of fiber-dispersion properties (Fig. 4.1), provides a basis for the optimization of nonlinear fiber-optic components, including MS and tapered fibers for SC generation. With the  $a_{opt} \approx 0.4\lambda$  estimate in mind, supercontinuum generation was studied in MS fibers with multiple cores in the form of fused silica threads with a typical diameter of  $0.8 \mu\text{m}$ . In the following sections, the results of the experiments will be presented, providing the experimental evidence of SC generation enhancement in submicron-core MS fibers and confirming the expectations based on the theoretical analysis presented above.

## 4.2 Experimental setup

The experiments on supercontinuum generation were performed with a set of multiple-core fused-silica microstructure fibers having six submicron-diameter cores surrounding a larger central core with a diameter of 2 to  $5 \mu\text{m}$  (see the inset in Fig. 4.1), designed and fabricated in the group of Prof. A.M. Zheltikov. The technology employed to fabricate these MS fibers was similar to the standard procedure developed by Knight et al. [70] and described in details elsewhere [107].

Microstructure fibers combine the ideas of a holey fiber and a tapered fiber by integrating several small-core high-refractive-index-step fibers into a bundle as demonstrated in this work. This microstructure-fiber approach not only allows the total energy of SC emission to be increased, but also offers a very practical way to fabricate microstructure-integrated bundles of small-core high-index-step fibers with very large lengths, thus allowing one of the serious problems of tapered fibers (where taper waist lengths are typically limited to tens of centimeters) to be solved by means of fiber microstructuring. The larger central core of microstructure fibers demonstrated in this work can be used to guide laser pulses of higher intensities that would control

the process of SC generation in multiple small-core fibers surrounding this central fiber core through guided-mode coupling. Fibers as long as 100 m could be fabricated with no deviation from the above-described fiber design with multiple submicron thread-like cores, offering new possibilities in nonlinear optics and ultra-fast science.

The air-filling fraction of the microstructure part of the cladding in the created fibers, as shown in the inset of Fig. 4.1, is very high, providing a high-refractive-index step between the core and the cladding of the fiber. A system of smaller auxiliary air holes in the cladding of these fibers increases the refractive-index step between the fiber core and the fiber cladding and prevents the guided modes from leaking into the cladding. It also adds to the confinement of the light field in the fiber core and reduces optical losses of fiber modes. An array of submicron-size fused-silica channels in the form of threads, bound by the system of air holes in the fiber cladding (Fig. 4.1), serves as additional multiple cores of the fiber, providing a high degree of light confinement due to the high refractive-index step. Optical losses have been determined for microstructure fibers of this type from the results of measurements [108] performed on  $\sim 100\text{m}$  MS fiber segments. The magnitude of optical losses was estimated to be 23 dB/m for fibers with a single hexagonal cycle of air holes in the cladding and 0.405 dB/m for fibers with two cycles of air holes.

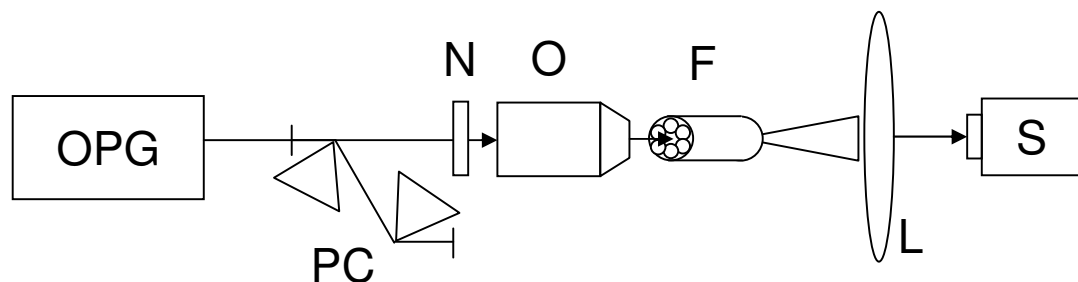


Figure 4.3: Schematic of the experiment. PC: double-pass prism compressor; N: neutral density filter; O: 40x micro-objective; F: piece of MS fiber; L: focusing lens; S: spectrometer.

Spectral broadening and supercontinuum generation in these MS fibers were studied using femtosecond laser pulses produced by an OPG. The pulses were recompressed by a double-pass prism compressor to typical pulse durations of 70 to 80 fs

and coupled into the MS fibers with a x40 micro-objective (0.65 N.A.) (Fig. 4.3). Neutral-density filters were used to vary the energy of the laser pulses coupled into the MS fibers.

### 4.3 Results and discussion

Two strategies of SC generation with multiple-core MS fibers are shown in Fig. 4.4. The first strategy (Fig. 4.4a) implies that femtosecond laser pulses are coupled into one or several submicron fused-silica threads surrounding the central core of a MS fiber. In the second scheme (Fig. 4.4b), pump pulses are coupled into the central fiber core. The spectra of radiation transmitted through a MS fiber in the first or second scheme are analyzed and the efficiency of spectral broadening and SC generation are compared.

When pulses with a duration of 80 fs produced by the OPG were coupled into the 0.8  $\mu\text{m}$  cores of a MS fiber (Fig. 4.4a), efficient SC generation was observed with a 2.5 cm long fiber section starting with pump-pulse energies as low as several hundreds of picojoules (Fig. 4.5, a). The spectra of SC emission produced in such fibers were studied as functions of the pump-radiation wavelength and energy. With the pump wavelength  $\lambda_p$  lying far from the wavelength of zero group-velocity dispersion  $\lambda_0$  (estimated as 510 nm in our case), a noticeable gap between the Stokes and anti-Stokes parts of SC spectra was observed within the spectral range around the point of zero group-velocity dispersion (the lower panel in Fig. 4.5a). Tuning the pump wavelength closer to  $\lambda_0$ , the merging of the Stokes and anti-Stokes parts into a broad continuous spectrum was observed (the middle panel in Fig. 4.5, a). These features of SC emission are similar to the properties of white-light generation observed in other microstructure-fiber experiments and simulations [82, 109, 110] and are indicative of parametric wave-mixing, stimulated Raman scattering, and soliton-fission scenarios of SC generation.

High values of group-velocity dispersion, characteristic of fibers with a high-refractive-index step and a small core radius (Fig. 4.1), are one of the most important physical factors limiting the efficiency of nonlinear-optical interactions of ultra-short



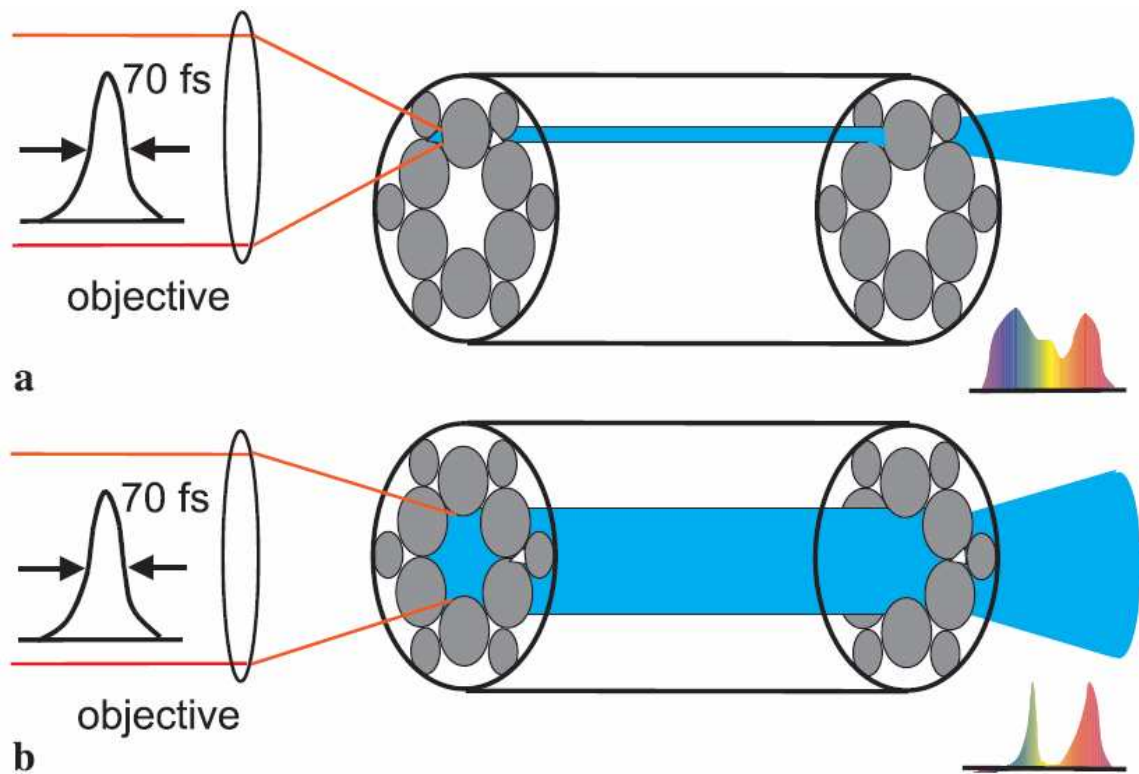


Figure 4.4: Two strategies of supercontinuum generation with multiple-core microstructure fibers: **a** fs laser pulses are coupled into one or several submicron fused-silica threads surrounding the central core of a MS fiber, **b** pump pulses are coupled into the central fiber core with a diameter ranging from 2 up to 5  $\mu\text{m}$ .

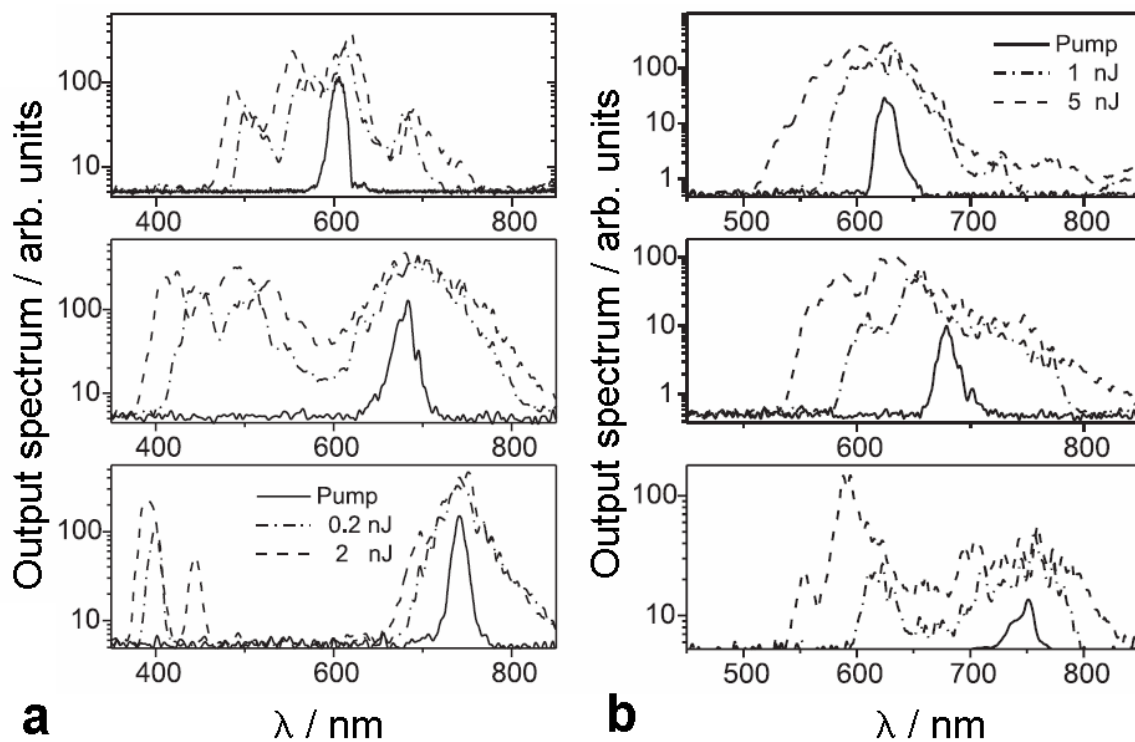


Figure 4.5: Spectra of supercontinuum emission produced by **a** 80 fs pulses of an OPG radiation with a wavelength tuned from 750 to 600 nm in a  $0.8 \mu\text{m}$  core of a microstructure fiber with the cross-section structure shown in the inset of Fig. 4.1 and a length of 2.5 cm, **b** 80 fs pulses of the OPG radiation with a wavelength tuned from 750 to 620 nm in a  $3 \mu\text{m}$  central core of a microstructure fiber with the cross-section structure shown in the inset of Fig. 4.1 and a length of 37 cm.

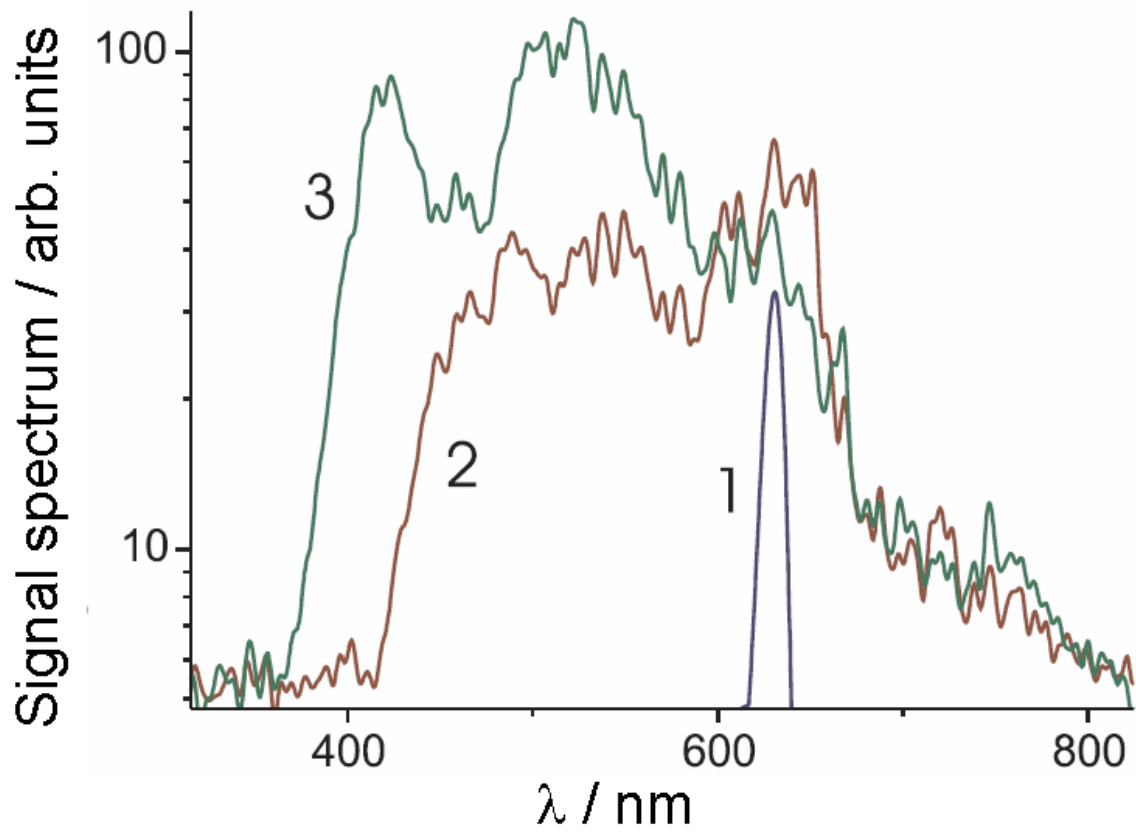


Figure 4.6: The spectra of chirp-controlled supercontinuum generated in a submicron core of a microstructure fiber: (1) the input pulse, (2) SC produced with a transform-limited pulse, (3) SC produced with a positively chirped pulse.

pulses in such fibers. For fused-silica threads with a diameter of  $0.8 \mu\text{m}$ , the group-velocity dispersion at a wavelength of  $800 \text{ nm}$  is estimated to be  $D \approx 270 \text{ ps}/(\text{nm km})$ . The dispersion length for  $70 \text{ fs}$  pulses is about  $5.5 \text{ cm}$  under these conditions. Initially chirped pulses were used in the experiments to increase the dispersion length and to improve the efficiency of supercontinuum generation. The results of the experiments carried out with transform-limited and chirped laser pulses are presented in Fig. 4.6. Laser pulses with an initial positive chirp, which experience compression in the regime of anomalous dispersion, implemented with submicron fused silica fiber threads (curve 1 in Fig. 4.1), allowed broader SC spectra to be generated under identical experimental conditions (cf. curves 2 and 3 in Fig. 4.6).

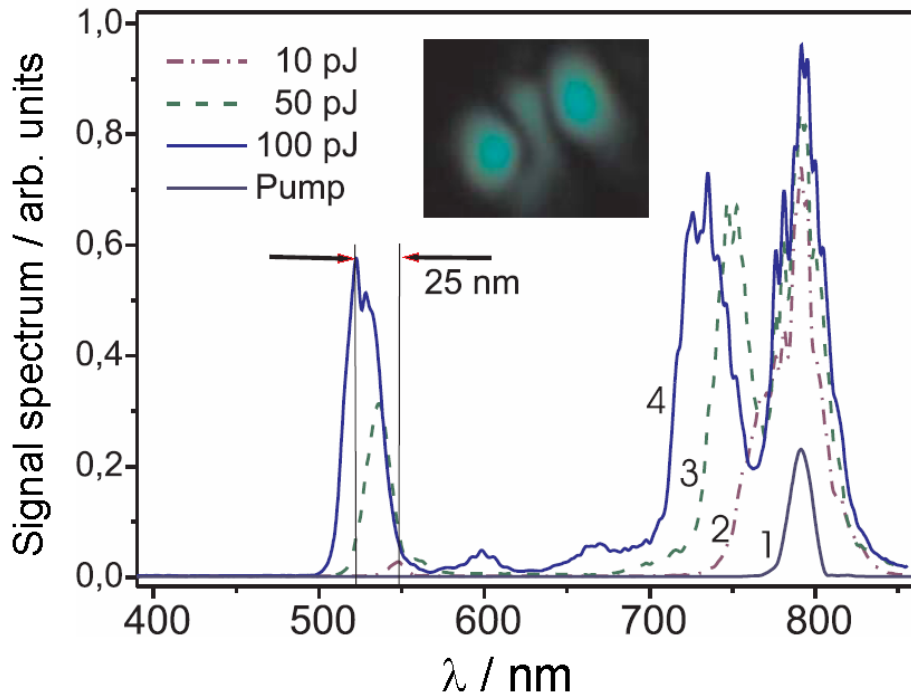


Figure 4.7: Spectral transformation of a  $70 \text{ fs}$  pulse of  $790 \text{ nm}$  pump radiation in a microstructure fiber with a  $3\text{-}\mu\text{m}$ -diameter central core. The spectrum of the input pulse is shown by line **1**. The input pulse energy is **(2)**  $10$ , **(3)**  $50$ , and **(4)**  $100 \text{ pJ}$ . The inset shows the emission pattern at the output of the fiber.

Supercontinuum generation in a larger central core of the microstructure fiber (Fig. 4.5, **b**) was characterized by a much lower efficiency. This is seen from a com-

parison of Fig. 4.5, **a** with the results of Fig. 4.5, **b**, which presents the spectra of SC emission produced by 80 fs pulses of the optical parametric amplifier with different energies coupled into the 3  $\mu\text{m}$  central core of a microstructure fiber with the same design and the length of 37 cm. This regime of nonlinear-optical interactions, however, proved to be advantageous for the generation of an isolated spectral component around 520 nm (Fig. 4.7) in the field of 790 nm pump pulses as a result of wave-mixing processes involving higher-order waveguide modes (see the inset in Fig. 4.7) in the MS fiber. The ratio of the amplitude of the signal at 520 nm to the amplitude of the 790 nm pump exceeded 0.6 for a pump-pulse energy of approximately 0.1 nJ.

### Anti-Stokes generation

The MS fibers employed in these experiments had a core diameter of 4.8  $\mu\text{m}$  and supported several guided modes. Insets 2 and 3 of Fig. 4.8 show the fundamental and one of the higher-order modes of the fibers. These modes have small longitudinal field components and can be considered approximately linearly polarized in the transverse plane. The wavelength of zero group-velocity dispersion,  $\lambda_0$ , was 1.22  $\mu\text{m}$  for the fundamental mode (Fig. 4.8, inset 2) and 790 nm for the first higher-order mode (Fig. 4.8, inset 3). Four-wave mixing process (FWM) was analyzed with a scalar approach. A modification of the approach to MS-fiber analysis proposed by Monro et al. [111] was employed to calculate the mismatch of propagation constants  $\delta\beta$  for the  $2\omega_p = \omega_s + \omega_a$  parametric FWM process ( $\omega_p$  is the frequency of the pump radiation and  $\omega_s$  and  $\omega_a$  are the frequencies of the Stokes and the anti-Stokes signals, respectively) in the fundamental (inset 2 of Fig. 4.8) and higher-order (inset 3 of Fig. 4.8) waveguide modes. These calculations have demonstrated the possibility of phase-matched FWM with a pump near 800 nm and anti-Stokes radiation generated at 520 to 530 nm in higher-order waveguide modes. The propagation constant mismatches  $\delta\beta$  for such FWM that involves 800 as well as 790 nm radiation as a pump are shown in curves 1 and 2 of Fig. 4.8. With the nonlinear coefficient  $\gamma = (n_2\omega/(cA_{eff}))$ , where  $n_2$  is the nonlinear refractive index,  $\omega$  is the pump frequency,  $c$  is the speed of light, and  $A_{eff}$  is the effective mode area, which is estimated to be  $1.3 \times 10^{22}$  and  $1.4 \times 10^{22}$

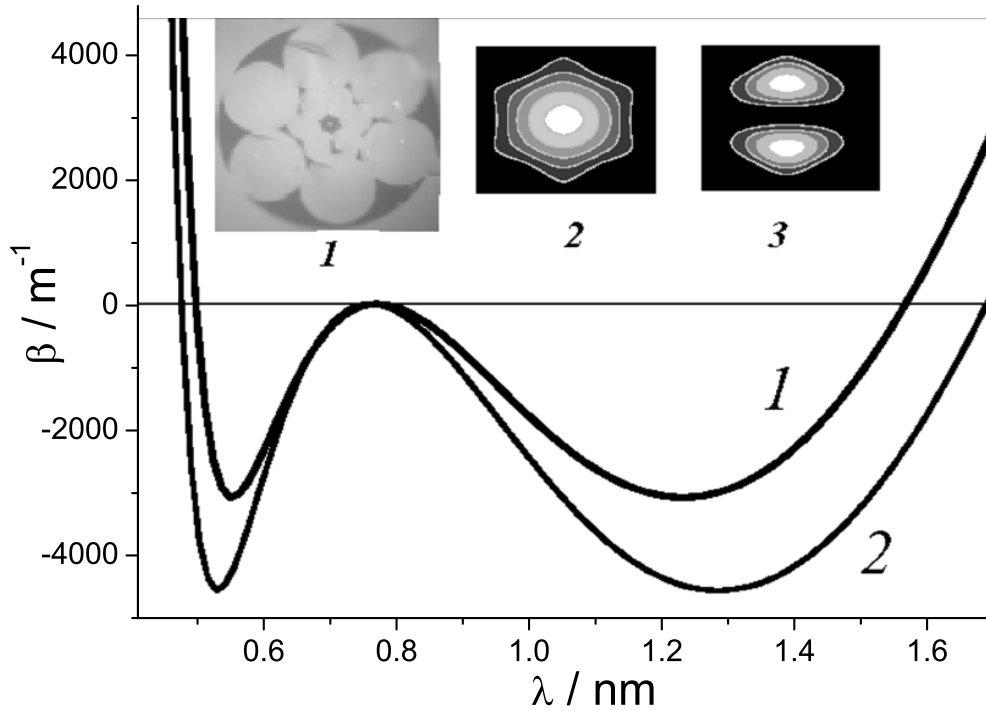


Figure 4.8: Mismatch of propagation constant  $\delta\beta$  of higher-order waveguide mode involved in the four-wave mixing process in a fused-silica MS fiber. The pump wavelengths are 800 nm (curve 1) and 790 nm (curve 2). Inset 1, cross-section view of the MS fiber. Insets 2 and 3, field intensity distributions in the fundamental and higher-order guided modes.

W/m for the fundamental and the first higher-order modes, respectively, the nonlinear contribution to the phase mismatch was negligible. The birefringence of fiber modes varied from  $10^6$  to  $10^5$  for the lowest-order modes and had virtually no influence on the observed phase matching.

Coupling 70 fs laser pulses of 790 nm radiation with an energy of 0.01 to 3 nJ into a 37 cm MS fiber with a cross-section structure shown in Fig. 4.8, inset 1, and a core diameter of  $4.8 \mu\text{m}$ , an efficient generation of the anti-Stokes signal centered at 520–530 nm (Fig. 4.9) could be observed. An analysis of the beam pattern of this signal (Fig. 4.9, inset) reveals a two-lobe structure that is characteristic of a higher-order waveguide mode, which permits, as shown by calculations presented in Fig. 4.8,

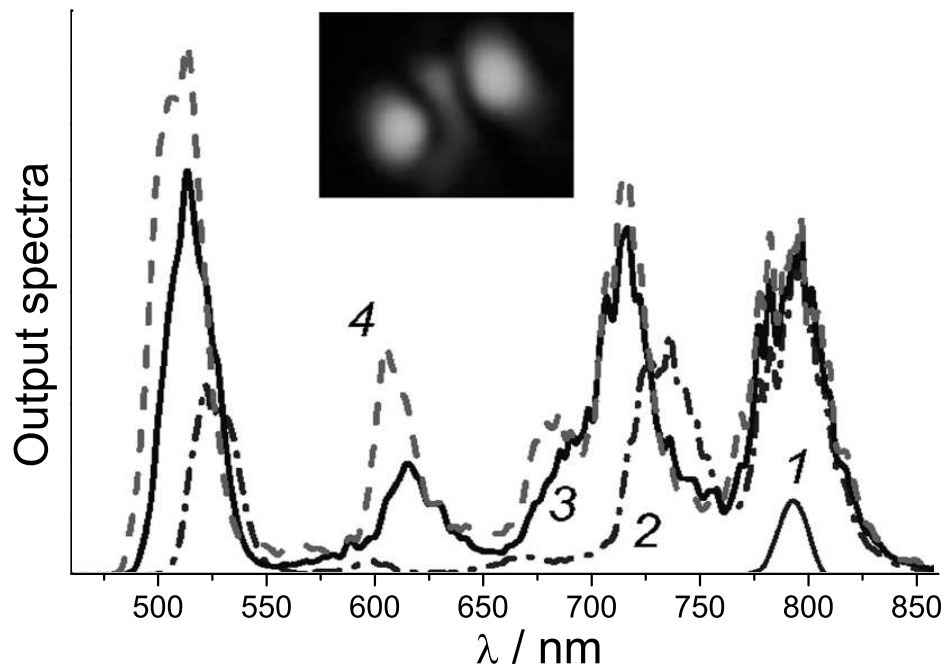


Figure 4.9: Spectral transformation of a 70 fs pulse of 790 nm pump radiation in a microstructure fiber. The spectrum of the input pulse is shown by curve 1. The input pulse energy is 0.1 (curve 2), 0.5 (curve 3), and 1 nJ (curve 4). Inset, emission pattern at the output of the fiber.

phase-matched generation of the anti-Stokes signal at 520-530 nm by a 790 nm pump through parametric FWM. The amplitude of the anti-Stokes component increased for higher pump pulse energies (see curves 2-4 in Fig. 4.9). The anti-Stokes signal amplitude, as can be seen from Fig. 4.9, starts to exceed the amplitude of the pump component in the output spectrum for an input pump pulse energy of less than 0.5 nJ. The maximum ratio of the anti-Stokes signal energy  $W_a$  to the energy  $W_p$  of the pump component in the output spectrum was estimated to be  $W_a/W_p \approx 1.7$ .

As the pump pulse broadens for higher pump energies, shorter-wave-length components appear in the spectrum of the pump pulse (curves 2-4 of Fig. 4.9). These components of the pump are phase matched with higher-frequency anti-Stokes wavelengths, leading to a blue shift of the anti-Stokes signal. This effect can be employed to tune the wavelength of the anti-Stokes signal.

The Stokes signal generated through the FWM process described here falls within the range of high radiation losses and is weak. The other spectral bands in the visible, that are blue shifted from the pump (Fig. 4.9), originate from mixed-mode parametric coupling and Raman processes. Energy transfer to the fundamental mode through mixed-mode parametric coupling is also shown in the inset of Fig. 4.9.

The structure of the MS fibers used in the experiments allows ultrashort laser pulses to be efficiently spectrally transformed (through both anti-Stokes generation and SC emission) by coupling laser radiation into the submicrometer-sized thread-like fused-silica channels in the cladding of this fiber (Fig. 4.8, inset 1) to serve as additional multiple fiber cores. Although the idea of phase matching FWM in the fundamental and higher-order guided modes in such channels is essentially the same as for the central core of the fiber, these submicrometer fused-silica threads permit frequency conversion to spectral ranges other than those accessible with the central core of the same fiber. These peripheral fiber cores also provide much higher efficiencies of SC generation owing to their small sizes and high refractive-index steps.

Femtosecond pulses of 750 nm radiation coupled into 0.8  $\mu\text{m}$  cores of the MS fiber (Fig. 4.8, inset 1) efficiently generated an anti-Stokes signal near 400 nm (Fig. 4.10, bottom) in the fundamental guided mode, with a frequency interval between the anti-Stokes and pump signals of  $\sim 350$  THz. For 1.5 nJ pump pulses coupled into a submicrometer core of a 2.5 cm long MS fiber, the ratio of the anti-Stokes signal amplitude to the amplitude of pump radiation exceeded 0.5.

With the pump wavelength  $\lambda_p$  lying far from the wavelength of zero group-velocity dispersion  $\lambda_0$  ( $\sim 510$  nm for the fundamental mode of 0.8  $\mu\text{m}$  core fibers), a noticeable gap between the pump and the anti-Stokes parts of the output spectra was observed (Fig. 4.10, bottom). Under these conditions the emission of anti-Stokes components near 400 nm agrees well with the example of soliton fission SC generation and is most likely related to dispersive waves, that result from soliton fission. Tuning the pump wavelength closer to  $\lambda_0$ , merging of the pump and the anti-Stokes parts of the spectrum into a broad continuous spectrum was observed (Fig. 4.10, top and middle). These properties of SC emission are similar to those of white-light generation observed in other MS-fiber experiments and simulations.



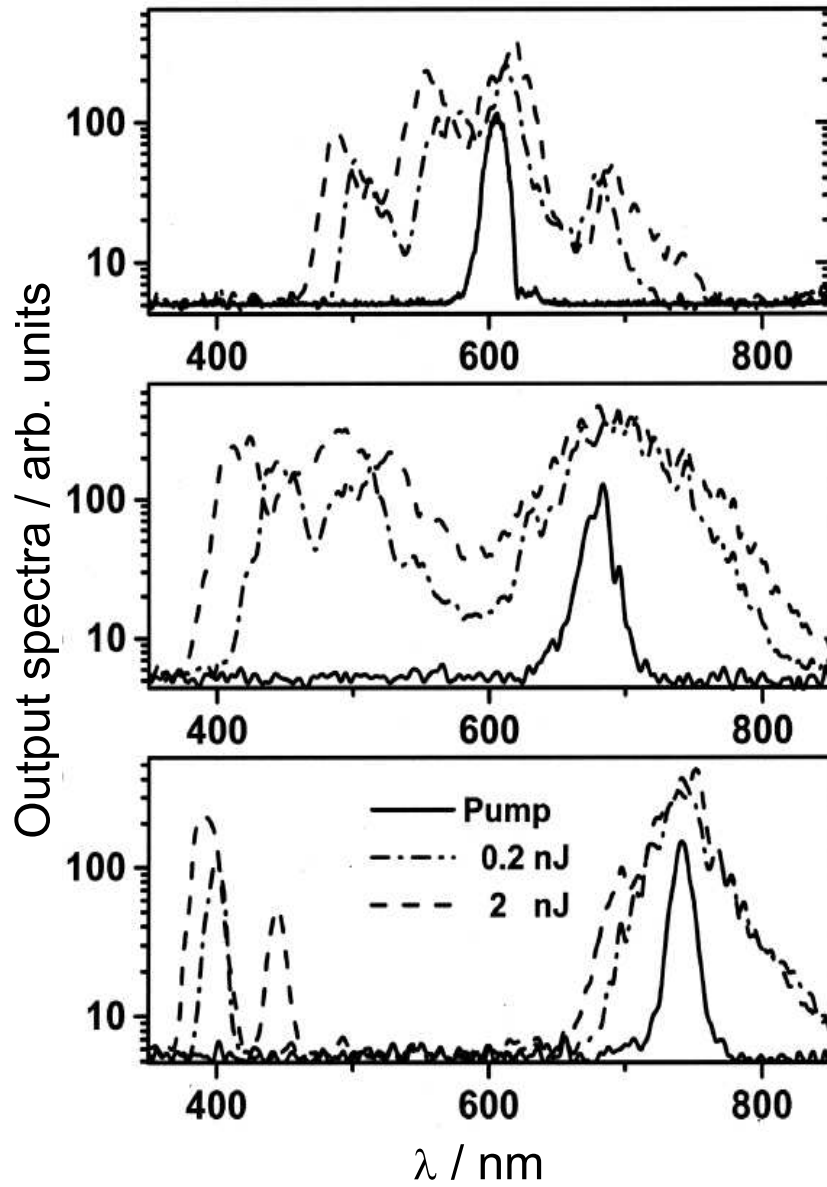


Figure 4.10: Spectra of supercontinuum emission produced by 80 fs pulses with a wavelength tuned from 750 to 600 nm in a  $0.8 \mu\text{m}$  peripheral core of a microstructure fiber with the cross-section structure shown in the inset 1 of Fig. 4.8 and a length of 2.5 cm

## 4.4 Conclusion

Supercontinuum generation in microstructure fibers of new design was demonstrated, with a broadband emission produced in six submicron-diameter cores in the form of fused-silica threads surrounding a larger central core with a diameter of 2 to 5  $\mu\text{m}$ . It has been shown that submicron-core fused-silica MS fibers allow to maximize the ratio of the fiber-core-confined laser power to the fiber-core diameter. Therefore, such fibers are ideally suited to provide limiting waveguide enhancement factors for a broad class of nonlinear-optical processes contributing to supercontinuum generation. The results of the presented experimental studies are fully consistent with theoretical predictions, showing that the efficiency of SC generation achieved with MS fiber cores with a diameter of 0.8  $\mu\text{m}$  is much higher than the SC generation efficiency attainable with MS fibers of 3  $\mu\text{m}$  core diameter.

It has been also shown that phase-matched four-wave mixing process in higher order modes of a MS fiber allows extremely high efficiencies of anti-Stokes frequency conversion to be achieved for subnanjoule, femtosecond laser pulses. The amplitude of the anti-Stokes signal generated by 70 fs pulses of 790 nm radiation in a higher-order mode of a MS fiber with a 4.8  $\mu\text{m}$  core exceeded the amplitude of the pump component in the output spectrum starting with input pump pulse energies near 0.5 nJ. Femtosecond pulses of 750 nm radiation coupled into submicrometer fiber cores generate an anti-Stokes signal near 400 nm with an amplitude comparable with the amplitude of the pump component.

## Part II

# Time-resolved spectroscopy on excited-state dynamics of polyatomic molecules



Information about the structure and the dynamics of polyatomic molecules in excited (non-equilibrium) states is of great importance, since it provides an understanding of the initial steps in photoinduced processes such as photosynthesis and vision. Modern sources of coherent radiation facilitates the application of nonlinear optical spectroscopy allowing for elementary dynamics events in microscopic systems to be probed selectively with high temporal and spatial resolution. Four-wave mixing (FWM) processes in the form of coherent anti-Stokes Raman scattering and photon echo provide excellent examples of nonlinear optical interactions successively utilized in time-resolved spectroscopy. FWM techniques have their advantages in coherent properties of the generated signal and in a great number of available degrees of freedom.



## Chapter 5

# Spectroscopic techniques

### 5.1 Pump-probe transient absorption

The understanding of photochemical reactions and processes is based on the information about the sequence of events that occur following the absorption of a photon. Metastable or *transient* species, for instance excited electronic states and radicals, formed in course of many reactions are very short-lived by their nature and under conventional reaction conditions their concentration is vanishingly small. If a reaction is being triggered by a short, intense pulse of light, relatively high concentrations of the intermediates is produced and these species can be detected by conventional spectroscopic techniques. This method was proposed by Porter, who shared with Eigen the 1967 Nobel Prize for Chemistry 'for their studies of extremely fast chemical reactions, effected by disturbing the equilibrium by means of very short pulses of energy'. Progress in generation of ultrashort light pulses have changed the meaning of the term 'fast reactions'. Nowadays, pump-probe has become the most widely used technique for monitoring reactions on a time-scale down to  $10^{-15}$  s, allowing an insight into the dynamics at the most fundamental level.

Pump-probe method exists in various modification, e.g. time-resolved resonance Raman, fluorescence up-conversion or photoelectron spectroscopy, etc. [112, 113]. A simple form of a pump-probe method utilizing linear material response to electric field is represented by the transient absorption spectroscopy. Here, the absorption spectra

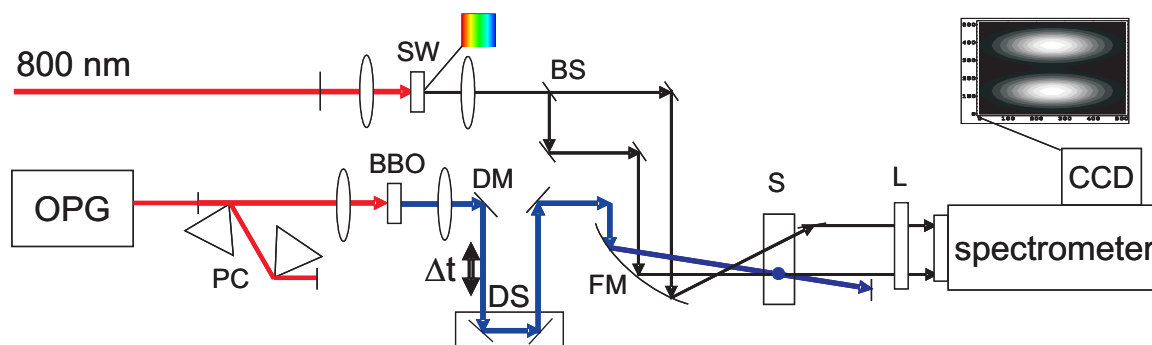


Figure 5.1: A schematic diagram of the pump-probe transient absorption setup in the form used for the experiments presented in the work. For details see text.

and the kinetic behavior of transient species are studied by monitoring electronic absorption spectra of the disturbed sample as a function of time passed after an impulsive perturbation. A schematic diagram of the pump-probe transient absorption setup is depicted in Fig. 5.1 in the form used for experiments presented in this work.

For the generation of the UV pump pulse, the visible OPG output is recompressed by means of a double-prism compressor PC and sent through a frequency doubling stage, consisting of two focusing lenses with a BBO crystal between them. The generated UV light is separated from the visible by means of a dichroic mirror, DM and passes an electro-mechanical delay stage, DS, capable to introduce time delays of up to 650 ps. For the generation of the probe and reference pulses, a small fraction of the CPA-1000 output (wavelength of  $\sim 800$  nm), is focused in a Sapphirine window, SW of 3 mm thickness. The generated supercontinuum is collimated by a focusing lens and split into two equal parts by means of a broadband beam-splitter BS. The resulting beams are focused into a sample, S by means of a focusing mirror, FM in such a manner, that the pump and the probe beams overlap within the sample space (blue dot in Fig. 5.1). The reference beam passes through the sample without being overlapped with any other beam. The UV pump beam is blocked right after the sample whereas the probe and reference beams are sent into a spectrometer. Before they enter the spectrometer slit, they are made parallel and focused on the slit by means of a cylindric lens, L. The picture observed on the CCD is presented schematically as an inset in Fig. 5.1. Here, the ordinate represents the wavelength



of the detected signal and the abscissa represents the geometric size of the beam, intensity increases from black to white. The two spots correspond to the two beams separately detected on the single CCD chip.

The evaluation of the obtained data is established and includes the integration of the signal across the beam diameter for every wavelength in order to obtain the spectrum. Probe and reference spectra are recorded as functions of the delay time between the pump and probe pulses. For every delay time  $\Delta t$ , the absorption spectrum of the transient species is approximately given by a difference absorption spectrum  $A^{\Delta t}(\lambda)$ , calculated as  $A^{\Delta t}(\lambda) = 1 - I_{probe}^{\Delta t}(\lambda)/I_{ref}(\lambda)$ , where  $I_{probe}^{\Delta t}(\lambda)$  is the detected intensity spectrum of the probe and  $I_{ref}(\lambda)$  is the detected intensity spectrum of the reference (which is independent of  $\Delta t$ ). In the calculated difference absorption spectrum, the positive regions correspond to photoinduced non-equilibrium (excited) states absorption, whereas negative regions are due to photoinduced bleach of the equilibrium (ground) state absorption or to stimulated emission (see, for example sections 6.3.2 and 7.3.1).

The time resolution of the pump-probe transient absorption method is defined by the cross-correlation of the pump and probe pulses, which in the presented experiments was on the order of 1 ps. The sensitivity of the method is restricted due to non-background-free detection and, in some degree, due to instability of the supercontinuum generation. The way to overcome these problems is the exploitation of the coherent modification to the pump-probe, namely the transient population gratings technique.

## 5.2 Transient population gratings

Time-resolved transient grating spectroscopy is a four-wave mixing technique which involves third order optical nonlinear processes. The name 'transient grating' is used here to highlight the fact that most of the information obtained from such experiments derives from the time ordering of various ultrashort pulses and not from high-resolution frequency tuning [114,115].

Over the past twenty years, the transient grating (TG) technique has been intensively applied to study many physical processes [114] such as electronic energy transport [116], the optical Kerr effect [117], studies of diffusion in liquids [118], photoinduced electron transfer [119], nonadiabatic transitions [120] and excited state dynamics [121]. In a transient grating experiment, the sample is excited by two spatially crossed and time coincident laser pulses producing an interference pattern. The interaction between the light field and the sample results in a spatial modulation of the complex refractive index of the sample in the crossing region. The amplitude of this grating like distribution is measured by a third laser pulse, which is delayed in time, striking the grating under the Bragg angle. The intensity of the diffracted light depends on the modulation amplitude of the complex refractive index grating, i.e. on the variation of absorbance and refractive index in the sample. Therefore, TG can be used as an alternative to the more conventional transient absorption spectroscopy. As the TG signal has no background, this technique is much more sensitive than transient absorption. It allows the detection of transient species with low extinction coefficients without using too high excitation intensities which would induce undesired nonlinear optical effects. The superior sensitivity of the grating detection over transmission has been very clearly demonstrated in spectral hole-burning spectroscopy by Wild and co-workers [122].

Figure 5.2 shows a potential energy diagram for the realization of the TG scheme in the form used for the experiments with azulene described in section 6.3.2. The first two laser pulses ( $\mathbf{k}_{\text{pu1}}$  and  $\mathbf{k}_{\text{pu2}}$ ) interacting with the sample possess the same color and are referred to as *pump* lasers, while the third laser ( $\mathbf{k}_{\text{pr}}$ ) is variable in its color and is referred to as the *probe* laser. In the transient grating scheme, the first two pump pulses ( $\mathbf{k}_{\text{pu1}}$  and  $\mathbf{k}_{\text{pu2}}$ ) interact simultaneously with the sample, preparing a transient grating of the electronic excited state molecules. The probe pulse ( $\mathbf{k}_{\text{pr}}(\Delta t)$ ) is delayed in time by  $\Delta t$  relative to the pump lasers, in order to interrogate the dynamics of the transient population. By choosing the color of the probe pulse to be in resonance with an electronic transition that can only be accessed starting in an excited state, it is possible to selectively observe the development of the excited state population, while the dynamics of the electronic ground state do not contribute to the transient signal.

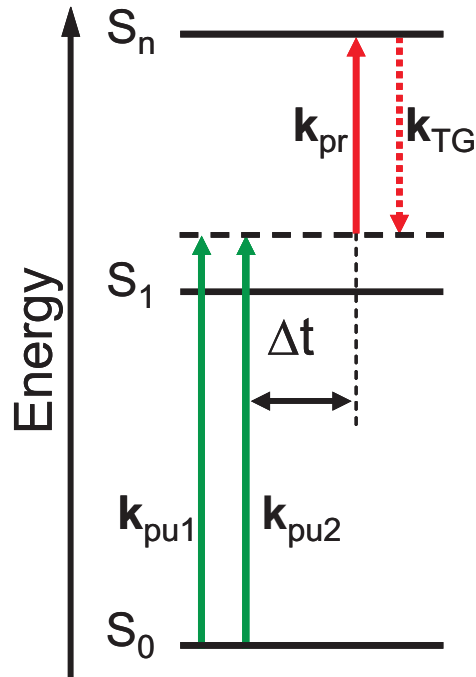


Figure 5.2: Potential energy diagram illustrating a TG experiment.

The fundamental difference between TG and the classical pump-probe scheme is rooted in the preparation of an excited state population grating by the two pump lasers rather than the simple population transfer by the single pump laser in a pump-probe scheme. The probe pulse is scattered elastically off the excited state population grating under Bragg conditions and an optically coherent signal is detected. Here, the homodyne detection leads to a quadratic proportionality of the population to the signal intensity, whereas in the pump-probe scheme the incoherent signal is linearly proportional to the population [114, 123].

The intensity of the light scattered off the induced grating can be expressed as [124]:

$$I_{TG}(\Delta t) = |A \cdot c_{S_1}^*(0)c_{S_1}(0)|^2 \exp(-2\Delta t/T_{1,S_1}). \quad (5.1)$$

Here,  $\Delta t$  is the time delay between the pair of pump pulses and the probe pulse,  $A$  is an amplitude factor and  $c_{S_1}(0)$  is the time-independent coefficient for the excited state probed at  $\Delta t = 0$ .  $T_{1,S_1}$  is the characteristic decay time of the investigated state.

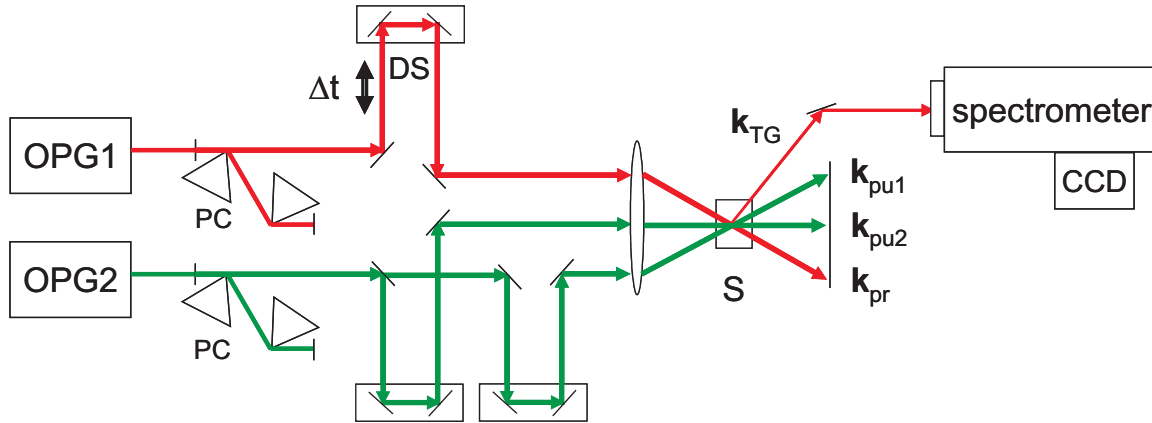


Figure 5.3: Scheme of a TG experiment setup as used for experiments described in section 6.3.1. For details see text.

The scheme of the transient grating setup in the form used in the experiments with azulene (section 6.3.1) is presented in Fig. 5.3. Here, the BOXCARS geometry is exploited for spatial separation of the four-wave mixing signal from the incoming laser beams. The output beam from the OPG2 is split by means of 50/50 beam-splitter in order to obtain two beams of the same color (*pump* beams  $\mathbf{k}_{\text{pu1}}$  and  $\mathbf{k}_{\text{pu2}}$ , see Fig. 5.2), which are utilized to induce the transient population grating in the sample, S. This is achieved by making them parallel and focusing in the sample space by means of a focusing lens, while the time delay between the two pump pulses is set to zero.

The pulses from OPG1 (*probe* beam  $\mathbf{k}_{\text{pr}}$ ) pass the delay stage, DS, to introduce a variable time delay ( $\Delta t$ , see Fig. 5.2). After that the probe beam is also focused so that it overlaps in the sample space with both pump beams. The four-wave mixing signal  $\mathbf{k}_{\text{TG}}$ , which is the result of the coherent *elastic* scattering of the probe on the induced population grating, is separated from the incoming beams and directed to the spectrometer. The signal intensity is detected by the CCD camera.

Figure 5.4 shows the cross-section, perpendicular to the optical axis of the beams participating in the four-wave mixing process related to the TG method (BOXCARS arrangement). One of the pump beam wave vectors  $\mathbf{k}_{\text{pu1}}$  lies in the same plane as the probe beam wave vector  $\mathbf{k}_{\text{pr}}$ . The probe laser is variable in its color with respect

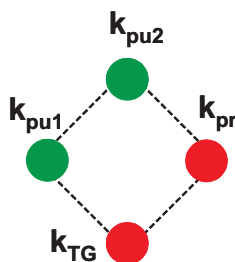


Figure 5.4: The BOXCARS arrangement of the beams as used for the TG experiments. For details see text.

to the pump laser and it is shown here spectrally red shifted. This forces the second pump laser ( $\mathbf{k}_{\text{pu2}}$ ) to be in the same plane as the signal, which is in its turn only phase matched for the elastic scattering of the probe laser:

$$\mathbf{k}_{\text{TG}} = \mathbf{k}_{\text{pu1}} - \mathbf{k}_{\text{pu2}} + \mathbf{k}_{\text{pr}}. \quad (5.2)$$

Therefore the TG signal has the same color as the probe laser.

As mentioned above, the TG technique is a sensitive and robust tool for monitoring electronic relaxation processes in polyatomic molecules. Although the TG method is capable of probing vibrational energy flow within different electronic states [120], it is not a vibrational-mode selective technique. For getting direct information about population dynamics of specific vibrational modes, the pump-CARS technique is highly valuable and will be described in the next section.

### 5.3 Pump-CARS scheme

Coherent anti-Stokes Raman scattering (CARS) offers a variety of degrees of freedom together with a substantial signal strength providing high flexibility and sensitivity. Application of the CARS process to the investigation of the vibrational dynamics in excited states of polyatomic molecules allows for selective observation of time-dependent changes in specific vibrational modes. This is accomplished by integrating the CARS process as a probe mechanism into a time-resolved pump-probe scheme. This type of configuration is referred to as a pump-CARS scheme, in analogy to the classical pump-probe scheme. The use of a complicated process such as CARS instead of single-laser probe that projects the time-dependent system into a

set of final states (see section 5.1) is justified by the possibility of tuning the CARS probe to the energy of a specific vibrational mode in the molecular system of interest. With this, the possibility of discriminating between the dynamics taking place within the individual vibrational modes of the system is introduced. Here, it is possible to extract information about the population dynamics of individual modes during vibrational energy redistribution processes such as intermolecular vibrational energy redistribution (IVR) and vibrational cooling and to gain direct insight into the precise mechanism of this type of transition. Payne et. al used picosecond CARS to attain information about the vibrational relaxation and isomerization of *trans*-stilbene upon photoinduced transition to the first electronic excited state [125]. Similar experiments were performed by Funk et al. on a nanosecond time scale, where the CARS probe extracted spectral information about triplet states of polycyclic aromatic systems, that were populated by pumping excited singlet states, that undergo intersystem crossing [126]. The femtosecond pump-CARS technique was successfully applied by Siebert et al. for exploring the influence of different normal modes on the rate of the  $S_0/S_1$  IC in  $\beta$ -carotene [127, 128].

As shown in Fig. 5.5, the pump-CARS scheme is characterized by the use of four pulsed laser fields, one of which plays the role of the initial pump (**P**), that initiates the dynamics in a molecular system by bringing it in a non-equilibrium state. Three further laser pulses, ( $\mathbf{k}_{\text{pu}}$ ,  $\mathbf{k}_{\text{S}}$  and  $\mathbf{k}_{\text{pr}}$ ) serve as a probe mechanism of the dynamics excited by the initial pump, participating in a CARS process. In order to achieve a time resolution, a variable time delay,  $\Delta t_1$  is introduced between the initial pump pulse and the three laser pulses of the CARS process. A constant time delay  $\Delta t_2 = 300$  fs between pump/Stokes pair of CARS pulses  $\mathbf{k}_{\text{pu}}/\mathbf{k}_{\text{S}}$  and the probe CARS pulse  $\mathbf{k}_{\text{pr}}$  can be introduced in order to suppress non-resonant electronic contribution to the CARS signal. The pump and probe lasers of the CARS process ( $\mathbf{k}_{\text{pu}}$  and  $\mathbf{k}_{\text{pr}}$  in Fig. 5.5) are tuned resonant with a  $S_n \leftarrow S_1$  optical transition. This allows for the enhancement of the CARS signal originated from the  $S_1$ -state versus the CARS signal from the  $S_0$ -state.

In order to monitor the population dynamics of a specific vibrational mode in the excited state potential, the wavelength of the Stokes laser ( $\mathbf{k}_{\text{S}}$  in Fig. 5.5) is adjusted

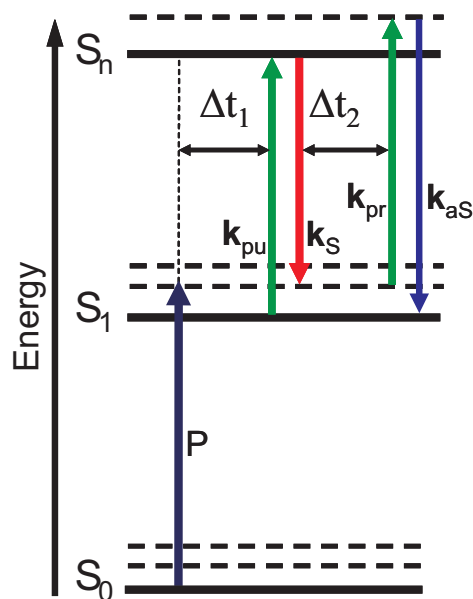


Figure 5.5: Potential energy diagram illustrating pump-CARS experiment.

so that the wavenumber difference,  $\Delta\tilde{\nu}$  between the pump and the Stokes lasers corresponds to the energy spacing of a specific vibrational mode. The mechanism with which the CARS process is able to selectively interrogate specific normal modes has its foundation in the strong enhancement of the CARS signal intensity in the case that the wavenumber difference,  $\Delta\tilde{\nu}$  between the pump and Stokes laser ( $\mathbf{k}_{\text{pu}}/\mathbf{k}_{\text{S}}$ , Fig. 5.5) corresponds to a Raman transition of a vibrational mode in the electronic excited state. The resonance enhancement by means of a Raman transition is the result of an effective projection of an initial population in a vibrational state of a particular vibrational mode (with the quantum number,  $(v = n; n = 0, 1, 2, 3\dots)$ ), into an intermediate vibrational state ( $v = n + 1$ ) through the interaction with **1** and **2**. In the case of a Raman resonance, an effectively prepared, intermediate vibrational state ( $v = n + 1$ ) of a specific mode will lead to a strong inelastic scattering of the probe laser  $\mathbf{k}_{\text{pr}}$ , and subsequently to the generation of an intense coherent anti-Stokes signal ( $\mathbf{k}_{\text{aS}}$  in Fig. 5.5). The lack of a Raman resonance forces the CARS process to go through a virtual intermediate state, making the generation of the CARS signal out of the initial state ( $v = n$ ) through the interaction with lasers  $\mathbf{k}_{\text{pu}}$ ,  $\mathbf{k}_{\text{S}}$  and  $\mathbf{k}_{\text{pr}}$  extremely ineffective. The effect of the Raman resonance enhancement allows the

CARS probe to act as a filter that only shows a significant signal intensity for the normal mode to which  $\Delta\tilde{\nu}$  is tuned to [124].

By tuning the wavenumber difference  $\Delta\tilde{\nu}$  between the pump ( $\mathbf{k}_{\text{pu}}$ ) and Stokes ( $\mathbf{k}_{\text{S}}$ ) lasers to a value that corresponds to the energy of a specific vibrational mode seen in the Raman spectrum of the system, the coherent anti-Stokes signal is observed with the corresponding energy shift on the blue side of the pump lasers. The broadband nature of the CARS signal results from the spectrally broad fs laser pulses ( $\mathbf{k}_{\text{pu}}$ ,  $\mathbf{k}_{\text{S}}$  and  $\mathbf{k}_{\text{pr}}$ ) that generate the signal. This broadband nature of the pulses allows for the relevant groups of Raman modes of stilbene-3 to be incorporated in one of the two coherent anti-Stokes spectra. The intensity of the CARS signal ( $\mathbf{k}_{\text{aS}}$ , Fig. 5.5) can be monitored at a spectral position characteristic for a specific vibrational mode as a function of the delay time,  $\Delta t_1$  between the initial pump and the CARS probe ( $\Delta t_2 = \text{const}$ ).

For a clear picture of the experimental procedure, the order of events with respect to the delay time are discussed in the following. For  $\Delta t_1 < 0$ , the CARS process interacts with the system before the initial pump laser. For this sequence of the lasers, the CARS process probes a system that is in its equilibrium state and a constant CARS signal, originating from the ground-state Raman resonances can be observed. At  $\Delta t_1 = 0$ , the initial pump laser and the CARS process interact simultaneously with the system. The transfer of population into the  $S_1$  state induced by the initial pump laser will lead to the generation of excited state molecules available for the CARS-probe process *resonant* with the  $S_n \leftarrow S_1$  optical transition. This generation shows itself in a rise of the CARS signal intensity, getting enhanced by the  $S_n \leftarrow S_1$  electronic resonances. For delay times  $\Delta t_1 > 0$ , a population redistribution between the vibrational states within the electronic excited state via the IVR and vibrational cooling brings the transient molecules to the lower vibrational levels. If the final levels possess poor Franck-Condon factors for the  $S_n \leftarrow S_1$  transition, a weakening of the electronic resonances will lead to a decrease of the CARS signal intensity. An increase in the resonance-CARS signal intensity will be observed in the case when the final states possess higher Franck-Condon factors for  $S_n \leftarrow S_1$  transition. This situation is possible when reorganization of the bonds correspondent to the monitored vibrational modes takes place.



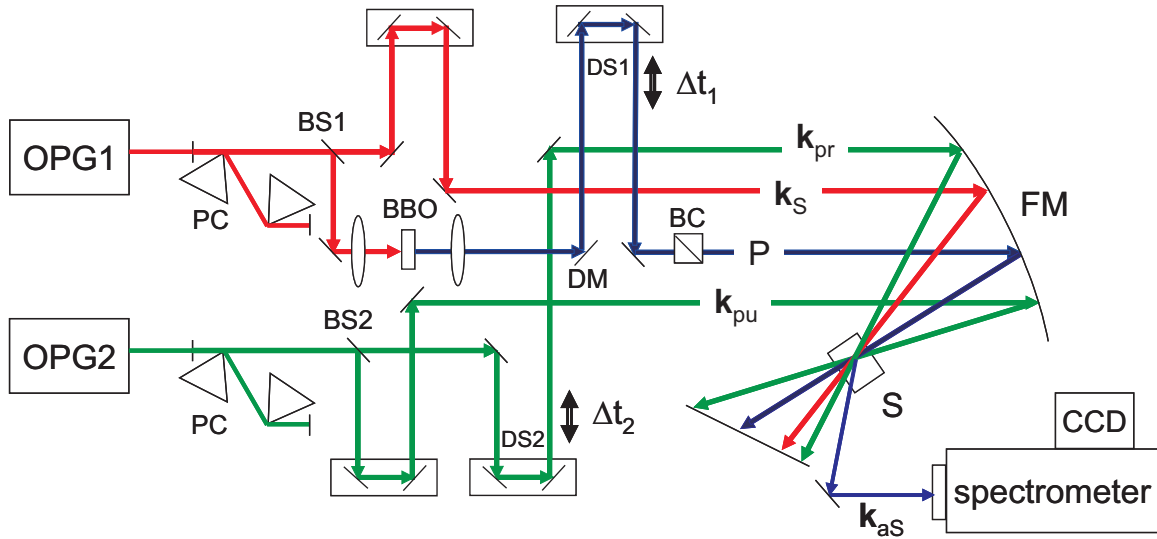


Figure 5.6: Scheme of pump-CARS setup as used in the experiments described in chapter 7. For details see text.

In the experiments presented in this work, the population dynamics was monitored for two characteristic groups of normal modes that possess enough spectral separation to be differentiated by the broadband laser pulses. For these vibrational modes, the transient behavior of the CARS signal at the corresponding spectral position was observed as a function of  $\Delta t_1$ . The pump-CARS setup as used in the experiments is presented in Fig. 5.6.

The output pulses from the OPG1 are divided into two parts by means of a 30/70 beam-splitter, BS1. The stronger beam is focused into the BBO crystal in order to generate the UV radiation, which is separated from the visible light by means of dichroic mirror, DM. The UV beam serves as an auxiliary UV-pump (**P** in Fig. 5.5) in the pump-CARS experiments. The delay stage, DS1, introduces a variable delay time ( $\Delta t_1$  in Fig. 5.5) for the UV-pump pulse. The weaker part of the splitted at BS1 beam serves as a Stokes beam within the CARS process (beam **k<sub>S</sub>** in Fig. 5.5).

The output beam from the OPG2 is split into two equally energetic beams by means of a 50/50 beam-splitter, BS2. One of the resulting beams is used further as a pump beam within the CARS process (beam **k<sub>pu</sub>** in Fig. 5.5). Another one is sent through the delay stage, DS2, in order to introduce variable delay time ( $\Delta t_2$

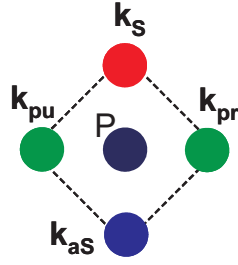


Figure 5.7: BOXCARS arrangement of the beams as used in pump-CARS experiments. For details see text.

in Fig. 5.5) and serves as a probe beam within the CARS process (beam  $\mathbf{k}_{pr}$  in Fig. 5.5). All four beams ( $\mathbf{k}_{pu}$ ,  $\mathbf{k}_S$ ,  $\mathbf{k}_{pr}$  and  $\mathbf{P}$ ) are brought into a parallel noncollinear arrangement and are focused by means of a focusing mirror, FM into the sample, S, so that they all overlap within the sample space. The anti-Stokes signal  $\mathbf{k}_{aS}$  is generated within the CARS process and results from the *inelastic* scattering of the probe pulse ( $\mathbf{k}_{pr}$ ) on the polarization grating formed by CARS-pump and -Stokes beams  $\mathbf{k}_{pu}$  and  $\mathbf{k}_S$ . The spectrum of the anti-Stokes signal is detected by means of nitrogen-cooled CCD camera attached to the spectrometer.

For the pump-CARS experiments, the CARS lasers ( $\mathbf{k}_{pu}$ ,  $\mathbf{k}_S$  and  $\mathbf{k}_{pr}$ ) are arranged in a BOXCARS configuration. The UV-pump beam goes in the middle of the imaginary rhombus formed by the four CARS beams (Fig. 5.7).

Fig. 5.7 shows that the pump ( $\mathbf{k}_{pu}$ ) and the probe ( $\mathbf{k}_{pr}$ ) laser beams lie in the same plane, and the Stokes beam ( $\mathbf{k}_S$ ) and the anti-Stokes signal ( $\mathbf{k}_{aS}$ ) in another plane, which is perpendicular to the plane of pump and probe. The red shifted wavelength of the Stokes laser relative to the pump and probe lasers only allows phase matching of the inelastic scattering of the probe in form of the blue shifted anti-Stokes signal. The phase-matching condition for the anti-Stokes signal has the form:

$$\mathbf{k}_{aS} = \mathbf{k}_{pu} - \mathbf{k}_S + \mathbf{k}_{pr}. \quad (5.3)$$

In summary, three types of time-resolved spectroscopy are presented in this chapter. The linear pump-probe transient absorption technique allows for measuring time-dependent absorption spectra of the short-living products in photochemical reactions, e.g. excited states and radicals. A simple experimental setup as well as a straightforward data evaluation procedure makes this technique a method of choice for a number of applications. Nonlinear spectroscopic methods, based on third-order interactions of the laser electric field with a sample, possess high sensitivity due to the coherent nature of the signal produced within the correspondent four-wave mixing (FWM) processes. Numerous degrees of freedom, available within the FWM schemes, such as transient population gratings (TG) and pump-CARS, allow for the utilization of electronic as well as Raman resonances and make these techniques highly selective with respect to the electronic and vibrational dynamical processes in polyatomic molecules.



## Chapter 6

# Excited-state dynamics of azulene and its derivatives

Molecular electronics is a rapidly growing field of science, seeking for possibilities to build complex electronic circuits from single molecules. Substitution of silicon transistors, wires, etc. by specially designed molecules will allow for scaling elements of electronic devices down to few nanometers. Integration of the elements together without losing their desired electronic properties is one of the main problems encountered currently by molecular electronics.

In order to understand photophysical properties of the basic elements such as nonlinear optical (NLO) chromophores and to design new effective materials for molecular electronics, it is important to investigate the dynamics of these elements and to determine the relationships between structure and dynamics.

Azulene molecule can be used as a basic building element in materials relevant for molecular electronics devices [129–131]. Azulene can be incorporated in complex nonlinear optical chromophores [132], as a part of their  $\pi$ -system, which is usually substituted with donor and/or acceptor groups [133,134]. Due to substantial change in the dipole moment upon the transition from the ground to the excited state, broad charge-transfer band is observed in the absorption spectrum of azulene. Charge-transfer is quite a common feature of NLO chromophores [135–137]. Usually, coordinate metal centers serve as redox centers in electron transfer systems [138], but in

some cases organic donor/acceptor groups are used [139–141].

Among the other donor/acceptor groups capable to enhance charge-transfer properties of the NLO chromophores, bis(triarylamino) species attracted particular attention [142–144]. Recently, Lambert and coworkers synthesized highly substituted azulene derivatives [144], where the azulene molecule plays the role of a  $\pi$ -bridge substituted in axial as well as in lateral positions with donor and acceptor groups, donor groups being represented by bis(triarylamino) species. These molecules possess substantial polarization in the ground electronic state and complex two-dimensional electron-transfer system. The properties of this type of nonlinear molecular chromophores make it very promising material for molecular electronics devices.

In this chapter experiments on electronic relaxation dynamics of azulene and three azulene derivatives are presented. Two spectroscopic methods sensitive to the electronic states dynamics were implemented in these experiments: transient population gratings (TG) and pump-probe transient absorption (TA). The TG technique is essentially background-free and hence possesses an extreme sensitivity to the changes in the population of the molecular electronic states. On the other hand, TA can provide reliable spectral information about the excited states.

## 6.1 Materials. Azulene and its derivatives

Azulene is the non-alternant aromatic isomer of naphthalene. Its photophysical properties have been widely investigated since in 1955 Beer and Longuet-Higgins found that azulene shows fluorescence from the  $S_2$  and not from the  $S_1$  state [145], thus being one of the rare examples violating Kasha's rule. In a recent study [146], the  $S_1$  decay time of azulene in cyclohexane solution was determined as a function of the excess vibrational energy above the  $S_1$  origin. The  $S_1$  lifetime was found to decrease from 1.7 ps at the origin, down to  $\sim 0.4$  ps for  $1300\text{ cm}^{-1}$  excess energy. The radiationless decay was related to the occurrence of the  $S_1/S_0$  conical intersection [147]. On the other hand, the fluorescent  $S_2$  state is relatively long-lived,  $\approx 1\text{--}1.6$  ns in common solvents [148]. The absorption spectrum of azulene is depicted in Fig. 6.1.

Three azulene derivatives were synthesized in the group of Prof. Dr. Lambert, Institut für Organische Chemie, Universität Würzburg.

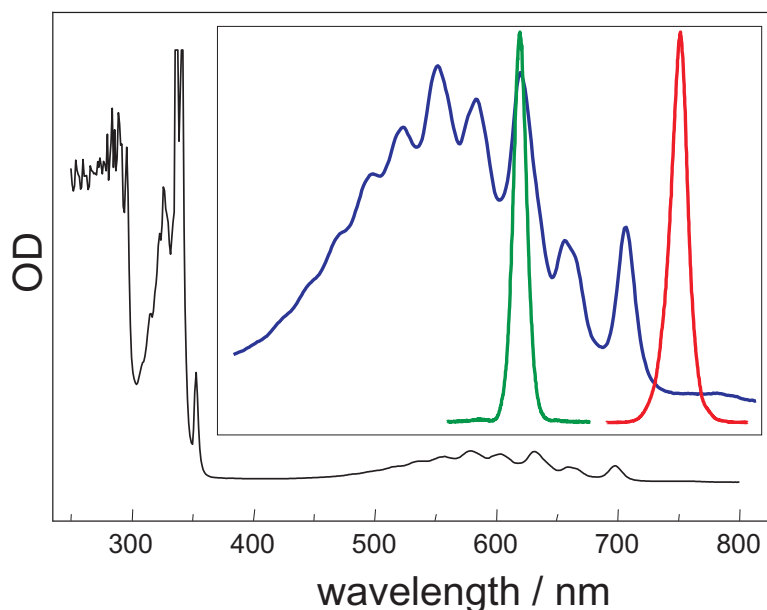


Figure 6.1: Absorption spectrum of azulene (black line). Inset shows the zoomed part of the spectrum corresponding to the  $S_1$  absorption (blue line) together with the spectra of pump (green line) and probe (red line) pulses used in the TG experiments described in this section.

In Fig. 6.2, the chemical structures of the three compounds investigated in this work are presented. Here, azulene is substituted by two donor groups along its axis (a dianysilamino group connected to the seven-membered ring and a triarylamino group connected to the five-membered ring). In the lateral positions three different substitutes with varying acceptor strength are connected symmetrically to the five-membered ring: (1) phenyl, (2) nitrobenzene, and (3) benzonitril groups. Owing to the intrinsic push-pull character of the central azulene moieties, the chromophores **1–3** are expected to display second-order nonlinear optical properties. The absorption spectra of the compounds dissolved in methyl tert-butyl ether (MTBE) are presented in Fig. 6.3. Each azulene derivative shows a very intense absorption band with a maximum between 430–480 nm. This band could be assigned to an intramolecular CT band, however it is difficult to attribute the donor and acceptor functions in this transition to particular groups [144].

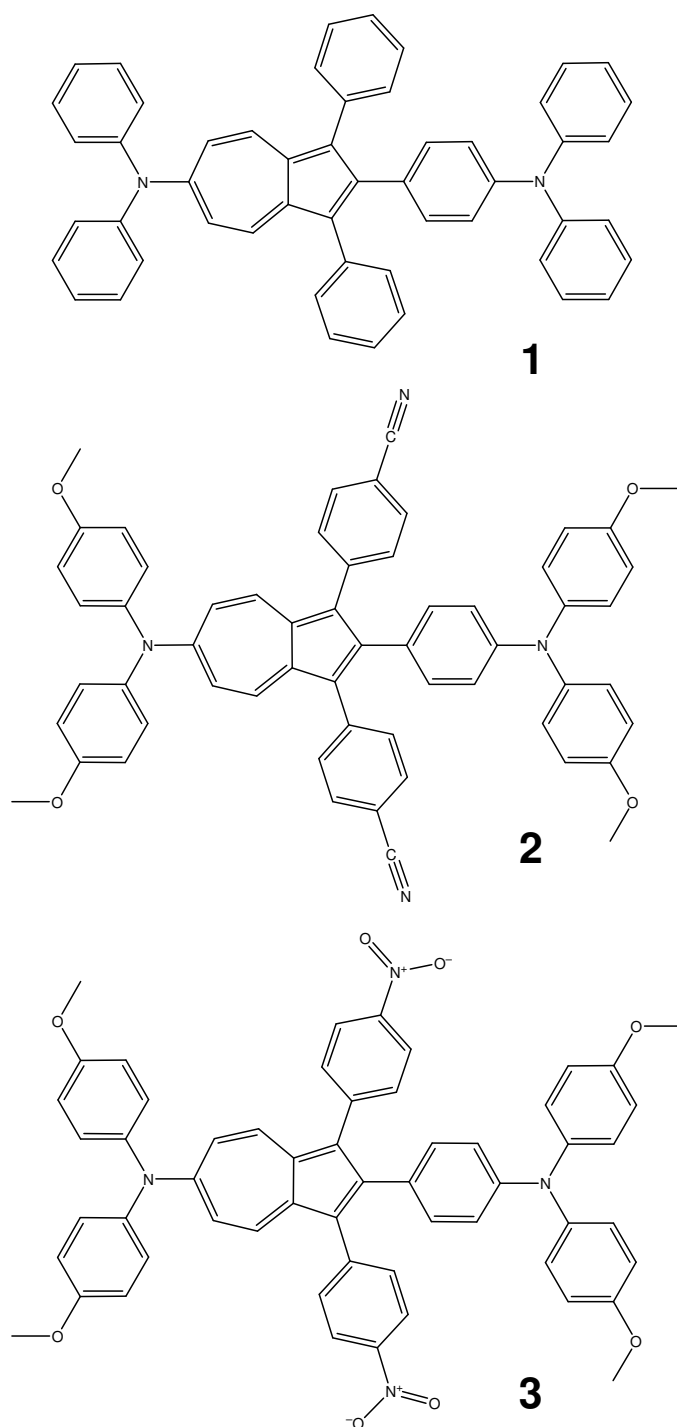


Figure 6.2: The chemical structures of the investigated azulene derivatives.



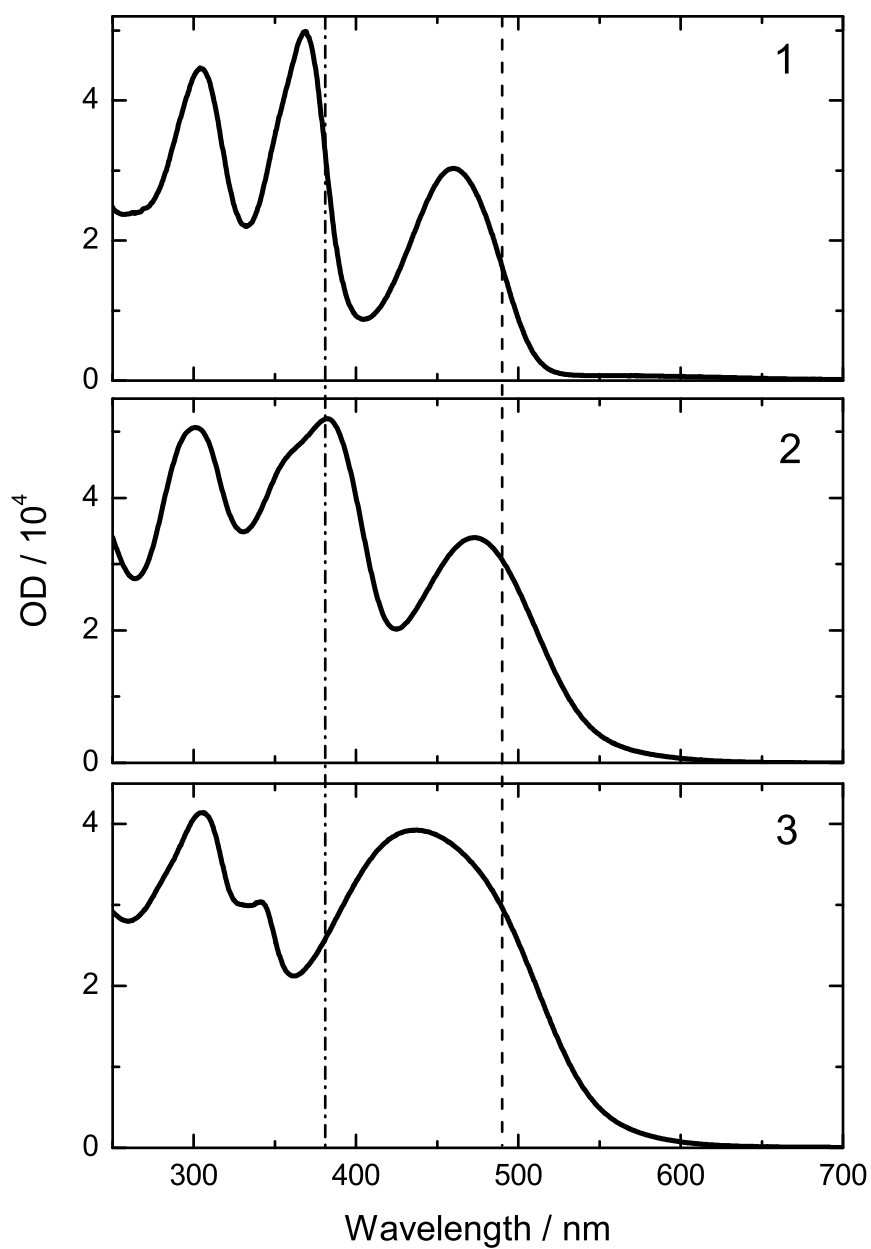


Figure 6.3: Absorption spectra of the investigated azulene derivatives shown in Fig. 6.2. Dashed line marks the position of the 490 nm pump, whereas dot-dashed line marks the position of 380 nm pump pulses.

## 6.2 Experimental details

### Transient gratings in azulene

In order to monitor the  $S_0 \leftarrow S_1$  internal conversion in azulene, an excited state population grating was prepared by focusing two pump pulses resonant with the first absorption band (620 nm, see Fig. 6.1) into the sample by means of an objective of 9 cm focal length. The third time delayed (probe) pulse at a wavelength of 760 nm, lies outside of the absorption band of azulene (Fig. 6.1). The cross-correlation of the pulses participating in the FWM process was measured as a nonresonant response in fused-silica glass, giving the time resolution of the experiment of about 100 fs. The scattered signal was separated from the incoming laser light by means of a pinhole and collimated by means of an objective of 9 cm focal length (see Fig. 5.3 for a complete layout of the experimental setup). The signal intensity was monitored by means of a CCD camera attached to the grating spectrometer. The spectrally integrated intensity of the TG signal was plotted as a function of the delay time  $\Delta t$  (Fig. 5.2).

Azulene (99%, Alrich) was dissolved in high-purity n-hexane (99%, Aldrich) at a concentration of  $\sim 100$  mM. The solution was placed in a 1-mm-thick sample cell with 0.1-mm-thick glass walls. During the experiment the cell was rotated with a frequency of about 20 Hz in order to avoid thermal effects.

### Transient absorption of azulene derivatives

The setup for performing the transient absorption measurements using the UV-pump pulses is described in section 5.1. Briefly, for the generation of the UV-pump pulses, centered at 380 nm, the output of one OPG was frequency doubled by a BBO crystal. The residual visible light (fundamental) was separated from the generated UV-light (second harmonic) by means of a dichroic mirror. The white light used as a probe and a reference beam was obtained by focusing a small fraction of the OPG output into a 3-mm-thick Sapphire window. The generated supercontinuum light was split into two equal parts (probe and reference beams) by means of a broadband beam-splitter. A spherical mirror with 20 mm focal length was employed to focus

the beams into the sample the way that pump (UV) and probe (supercontinuum) beams are overlapping within the sample volume, while the reference beam passes through the sample without being overlapped with the pump. For detection, the probe and the reference beams were sent to the spectrometer shifted vertically with respect to each other. The CCD camera, attached to the spectrometer, was split into two symmetric parts, thus allowing detection of the probe and the reference beams simultaneously. The difference absorption spectra were calculated from the recorded probe and reference spectra as a function of the delay time between pump and probe pulse.

A saturated solution of compound **2** (see Fig.6.2) in methyl tert-butyl ether (MTBE) was used for the experiments. The measurements were performed in a 2 mm thick rotating quartz-glass sample cell. The rotation frequency of the cell was about 20 Hz.

### Transient grating in azulene derivatives

For the investigation of the electronic relaxation pathways in the azulene derivatives, pump pulses of two different wavelengths were used. The first wavelength, 380 nm, was resonant with the second absorption band of compound **1** and **2** and with the blue side of the first absorption band of compound **3** (see Fig.6.3). The second wavelength, 490 nm, was resonant with the red flank of the absorption bands of all three investigated compounds (Fig.6.3). The probe pulses in all experiments were centered at 490 nm. The time resolution of the experiment determined by a cross-correlation measurement of the pump and probe pulses was for the UV pump pulse at 380 nm, 200 fs and for the visible pump at 490 nm, 150 fs.

For these experiments a saturated solution of the compounds **1–3** in MTBE was used. The same sample cell as described in the transient absorption measurements was also employed here.

## 6.3 Results and discussion

### 6.3.1 Coherent wave-packet motion during $S_0 \leftarrow S_1$ internal conversion in azulene

A strong oscillatory contribution to the pump-probe decay signal of azulene was observed by Riedle and coworkers for pumping with an excess vibrational energy of more than  $1300\text{ cm}^{-1}$  above the  $S_1$  origin [149]. The oscillation frequency was about 160 and  $200\text{ cm}^{-1}$  for all pump wavelengths. These wavenumbers do not appear as line spacings in the cw absorption spectrum of azulene measured by Ruth et al. [150]. This is consistent with the observation that the oscillations only emerge if the excess energy is above  $1300\text{ cm}^{-1}$  and the wavepacket is able to leave the spectroscopically accessible Franck-Condon region. The observed oscillations were claimed to manifest a coherent wavepacket motion in two vibrational modes. Here, the wavepacket represents a coherent superposition of eigenstates in a bound electronic potential, oscillating with a classical vibrational period. The preparation of a suitable wavepacket was suggested by Tannor and Rice to be the first step on the way to manipulate the course of a chemical reaction by selective interaction with light (quantum control) [151].

In the presented experiment, a coherent wave-packet motion during the  $S_0 \leftarrow S_1$  internal conversion in azulene was monitored by means of TG technique. The observed dependence of the spectrally integrated TG signal intensity on the delay time between the pump pair and the probe pulse is depicted in Fig. 6.4.

It can be clearly seen that the ultrafast decay of the signal is modulated by oscillations. A Fourier analysis of the measured signal showed a strong contribution of the oscillatory component around  $170\text{ cm}^{-1}$ . This is in partial agreement with the results obtained by Riedle et al. [149]. Apparently, the time resolution of our instrumentation was not sufficient to distinguish between the 160 and  $200\text{ cm}^{-1}$  components. Nevertheless, the oscillations are very pronounced (see Ref. [149] for comparison), confirming the high sensitivity of the TG technique.

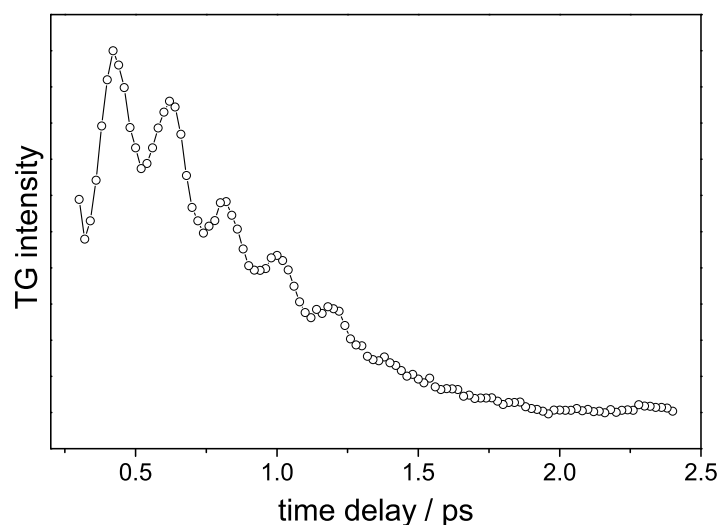


Figure 6.4: Transient grating signal of azulene rendering the  $S_1$  dynamics at a pump wavelength of 620 nm.

### 6.3.2 Transient absorption of azulene derivatives

The excited state absorption of one of the available azulene derivatives (Fig. 6.2, **2**) was measured in order to obtain information about the structure-dynamic relationship of electronically excited states in dianisylamino-triarylamine derivatives of azulene.

The time-dependent difference absorption data of **2** are shown in Fig. 6.5 for pumping at 490 nm and in Fig. 6.6 for pumping at 380 nm, respectively.

When compound **2** was excited into the red flank of the first absorption maximum (490 nm, see Fig. 6.3), a ground-state bleach could be observed in the region of 460–535 nm (Fig. 6.5). The maximum of the ground state bleach (500 nm) is 30 nm red-shifted from the first maximum of the steady-state absorption spectrum (cf. upper panel of Fig. 6.5 and Fig. 6.3, panel **2**). The ground-state bleach recovers almost completely within approximately 15 ps (see Fig. 6.5, lower panel, A). A transient absorption was observed in the region 500–630 nm. The red part of the transient absorption spectrum ( $>560$  nm) decays with approximately the same time constant as used to describe the ground-state bleach recovery (see Fig. 6.5, lower panel, D).

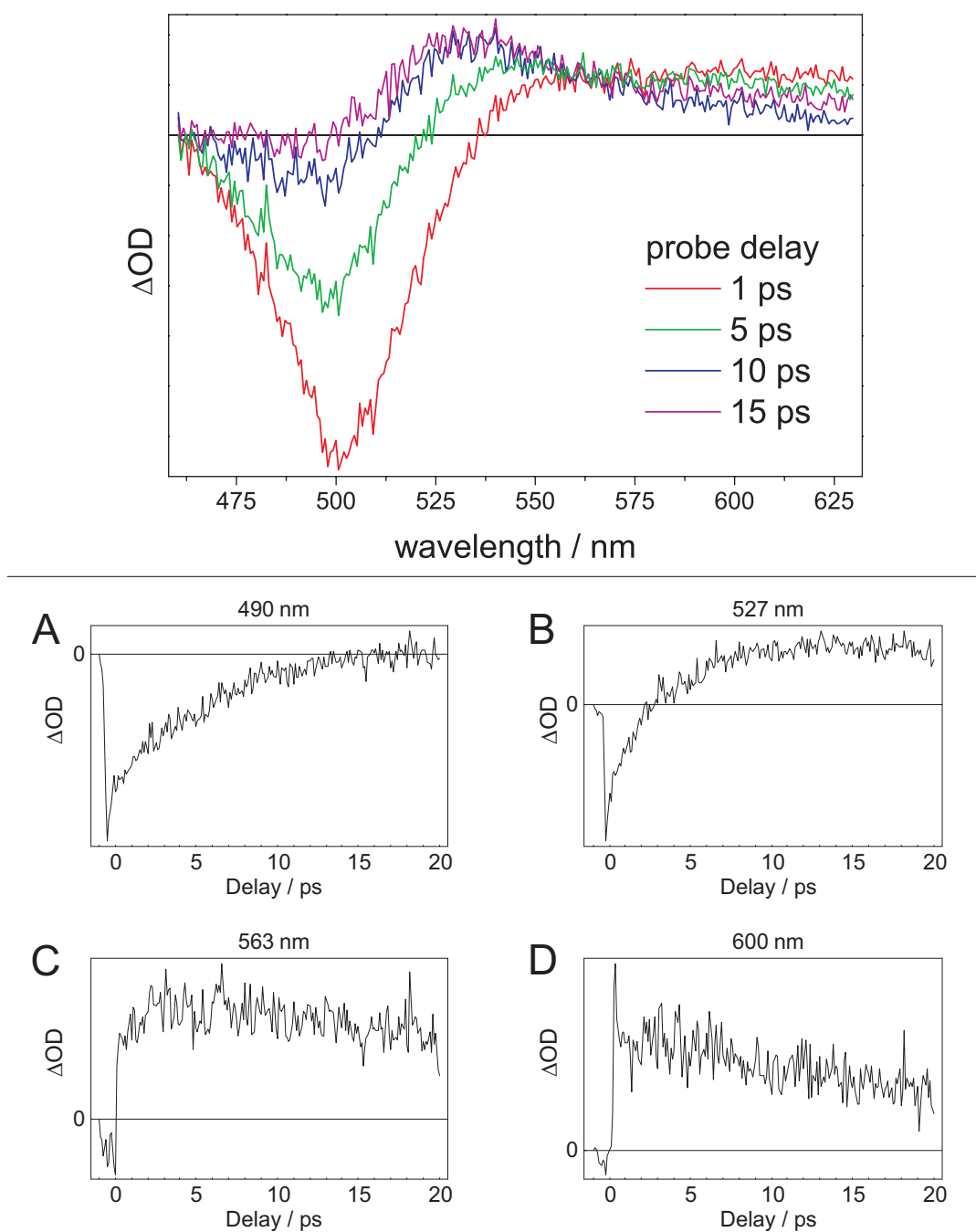


Figure 6.5: Upper panel, difference absorption spectra of compound **2** (Fig. 6.2) obtained for an excitation at 490 nm; lower panel, difference absorption of compound **2** plotted as a function of the pump delay time  $\Delta t$  for different wavelengths.

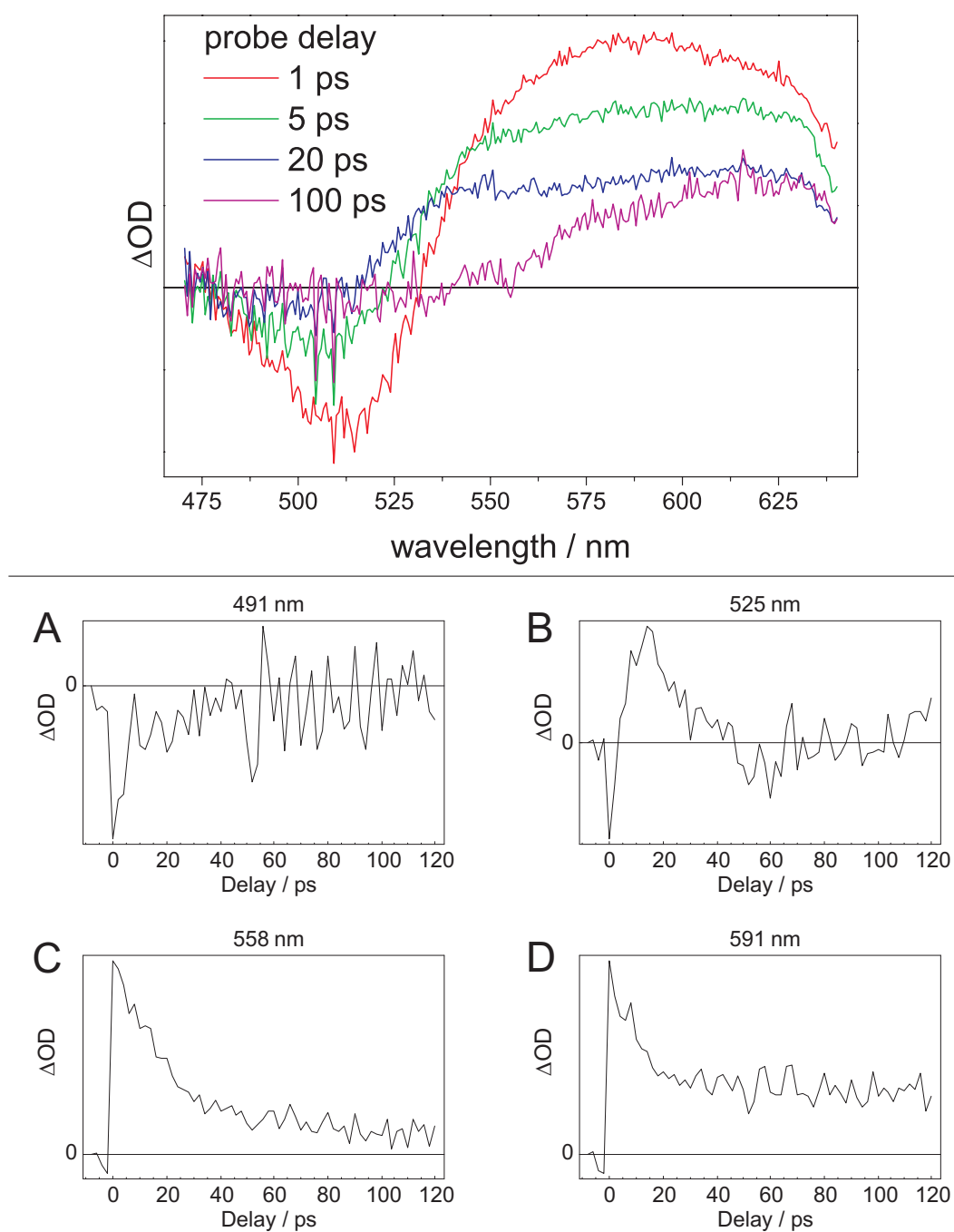


Figure 6.6: Upper panel, difference absorption spectra of compound **2** (Fig. 6.2) obtained for an excitation at 380 nm; lower panel, difference absorption of compound **2** plotted as a function of the pump delay time  $\Delta t$  for different wavelengths.

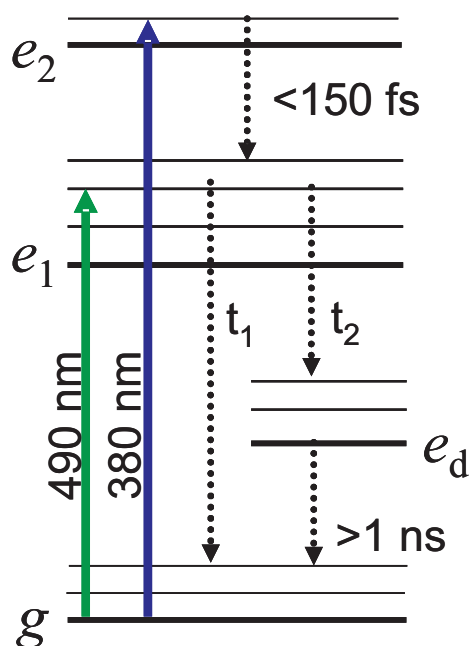


Figure 6.7: A model postulated for the relaxation pathways of the electronic excited states of the azulene derivatives. Here,  $t_1$  is the time constant of  $g \leftarrow e_1$  internal conversion,  $t_2$  is the time constant of  $e_d \leftarrow e_1$  IC. For further details see text.

The blue part of the transient absorption spectrum rises with a similar time constant (see Fig. 6.5, lower panel, B).

Pumping into the blue flank of the second absorption maximum of **2** (380 nm, see Fig. 6.3), a ground-state bleach was observed in the region of 460–535 nm (Fig. 6.6), which recovers after approximately 20 ps (see Fig. 6.6, lower panel, A). The maximum of the ground-state bleach at 515 nm is 45 nm red-shifted from the first maximum of the cw absorption (Fig. 6.3, **2**). In the transient absorption spectrum (510–630 nm) three regions could be distinguished. The blue flank (510–535 nm) rises first, then decays (Fig. 6.6, lower panel, B), the red flank (550–630 nm) decays first, then stays constant (Fig. 6.6, lower panel, D), whereas the middle part (535–550 nm) just decays (Fig. 6.6, lower panel, C).

Based on the results obtained, a model (Fig. 6.7) was formulated that includes the possible depopulation channels of the  $e_1$  potential, where  $e_1$  denotes the excited state of the azulene derivative, associated with the first absorption band. The existence of a long-lived 'dark' state, denoted as  $e_d$  was assumed, which could be a local state on



the azulene site of the molecule. With this, two processes can lead to the decay of the  $e_1$  population: internal conversion to the ground state  $g$  ( $g \leftarrow e_1$  IC) and internal conversion to the 'dark' state  $e_d$  ( $e_d \leftarrow e_1$ , see Fig. 6.7). The presence of the  $g \leftarrow e_1$  IC is confirmed by the disappearance of the ground-state bleach at 475–525 nm (see Fig. 6.5 and 6.5) and by the decay of the  $e_n \leftarrow e_1$  excited-state absorption (assuming that it is located in the spectral region of 500–620 nm). The time constant of the  $g \leftarrow e_1$  IC process was estimated to be about 15 ps, consequently the transient absorption in the region 540–630 was assigned to be due to a  $e_n \leftarrow e_d$  resonance. Limited stability of the red part of the white-light continuum used in these experiments prohibited the possibility to obtain spectral information about the long-wavelength part of the  $e_n \leftarrow e_d$  absorption.

Since no fluorescence was observed upon excitation to the state correspondent to the second absorption maximum (denoted as  $e_2$  in Fig. 6.7), relaxation of this state via an IC to the  $e_1$  state was assumed, with a characteristic time constant below 150 fs, the time resolution of our experimental setup. This assumption is supported by the similar behavior of the transient absorption of **2** for both cases of excitation, i.e. to the first and second absorption maximum, respectively.

### 6.3.3 Transient grating on azulene derivatives

In order to determine the time constants of the relaxation pathways of azulene derivatives with high precision, TG experiments were performed with MTBE solutions of the compounds **1-3** (Fig. 6.2). The kinetics of the TG signal is presented in Fig. 6.8 for the pump wavelengths of 490 nm (panel A) and 380 nm (panel B), respectively.

In order to evaluate the TG data, the model based on the levels scheme formulated in the preceding subsection was used to fit the obtained kinetics. The population of the  $e_1$ -state is characterized by the time constant of the  $g \leftarrow e_1$  internal conversion, ( $t_1$ ), and the time constant of the  $e_d \leftarrow e_1$  internal conversion, ( $t_2$ ) (see Fig. 6.7). Considering the time dependence of the transient grating intensity (equation 5.1), the following model is accepted:

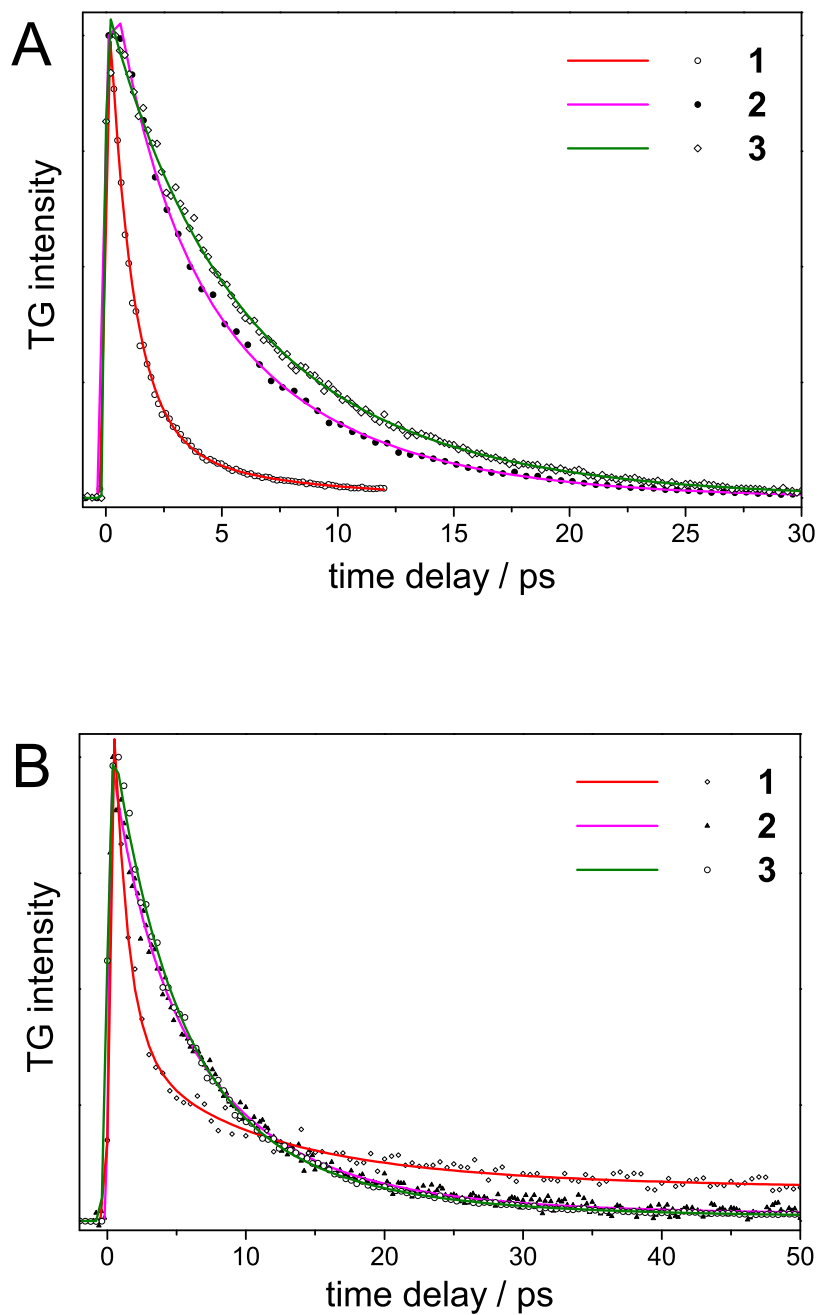


Figure 6.8: Spectrally integrated TG signals obtained for the azulene derivatives shown in Fig. 6.2 excited at 490 nm (panel A) and 380 nm (panel B), respectively.

$$I_{TG}(\Delta t) = |A \cdot \exp(-\Delta t/t_1) + (1 - A) \cdot \exp(-\Delta t/t_2) + C_{bg}|^2 \quad (6.1)$$

The model possesses four variable parameters describing the transient data, consisting of time constants  $t_1$  and  $t_2$ , the amplitude factor  $A$ , which describes the distribution between the  $g \leftarrow e_1$  and the  $e_d \leftarrow e_1$  channel of internal conversion, and the constant factor  $C_{bg}$ , being proportional to the population of the  $e_d$  level, the life-time of which is assumed to be infinite with respect to the time scales (650 ps) accessible in the experiments presented within this thesis. In order to increase the reliability of the values obtained in the fitting procedure, the number of parameters was restricted to three for both sets of data. In the case of 490 nm pumping, the constant background was negligible, hence  $C_{bg}$  was set to be equal to 0. For the set of data pumped with 380 nm, the time constant of the  $g \leftarrow e_1$  IC,  $t_1$  was assumed to be the same as in the case of 490 nm pumping. Indeed, the time constants of the  $e_d \leftarrow e_1$  IC obtained by fitting the second set of TG data are very close to those obtained for the first set of TG data. The results of the fitting procedure for both data sets are summarized in Tables 6.1 and 6.2, respectively.

	$t_1/ps$	$t_2/ps$
<b>1</b>	$12.1 \pm 0.9$	$1.4 \pm 0.2$
<b>2</b>	$12.4 \pm 0.6$	$3.0 \pm 0.4$
<b>3</b>	$15.2 \pm 0.7$	$4.6 \pm 0.7$

Table 6.1: Summary of the parameters obtained by fitting the TG data shown Fig. 6.8A according to equation 6.1.

	$t_1/ps$	$t_2/ps$	$C_{bg}$
<b>1</b>	12.1	$1.2 \pm 0.2$	$0.260 \pm 0.003$
<b>2</b>	12.4	$2.4 \pm 0.1$	$0.133 \pm 0.008$
<b>3</b>	15.2	$5.6 \pm 1.8$	$0.093 \pm 0.005$

Table 6.2: Summary of the parameters obtained by fitting the TG data shown Fig. 6.8B according to equation 6.1.

## 6.4 Conclusion

The capability of the TG method was examined for the example of the  $S_1 \leftarrow S_0$  IC in azulene. Oscillations of the TG signal superimposed on the ultrafast decay were observed for an n-hexane solution of azulene, which are manifestation of a coherent wavepacket motion on the  $S_1$  potential-energy surface. This observation proved the high sensitivity of the TG technique.

Transient absorption experiments were performed on one of the azulene derivatives in order to localize possible excited states in the investigated class of molecules. The existence of a long-lived 'dark' state was postulated based on the observed time-dependent behavior of the absorption spectrum of compound **2** (see Fig. 6.2). The relaxation of the state corresponding to the second absorption maximum was assumed to occur via an ultrafast internal conversion to a CT-state. Time constants of the proposed decay channels for the CT-state ( $e_1$ -state), namely internal conversion to the ground state and internal conversion to the 'dark' state, were determined with high precision by means of the TG technique.

## Chapter 7

# Vibrational energy redistribution in stilbene-3

A better understanding of the mechanism of vibrational energy redistribution taking place upon photoexcitation of molecular system is of great interest due to its crucial role within the pathway of photoinduced chemical reactions. Photoexcitation to a higher electronic state results in changes of the bonds which couple to the electronic transition and thus determine the initial time evolution of the system on the potential energy surface of the excited state. Non-adiabatic coupling of these initially populated modes to other intramolecular or environmental modes leads to a dephasing of the coherent vibrational motion, relaxation of vibrational population, and a deactivation of electronically excited states through radiationless processes such as internal conversion (IC). Processes involving changes in the population of different vibrational modes underlie vibrational energy redistribution (IVR) and, in the condensed phase, the transfer of excess vibrational energy to the environment (vibrational cooling) [152].

Investigation of the coupling between vibrational and electronic degrees of freedom requires implementation of time-resolved spectroscopic methods sensitive to the specific modes of the polyatomic system. A variety of relevant experimental schemes has been developed, many of them utilizing Raman transitions. One possible approach is the application of time-resolved linear Raman spectroscopy. Hartl et al., e.g., in-

investigated cooling processes in polyatomic molecules in solution on a femtosecond time-scale by pumping vibrational modes with infrared laser pulses that are resonant to the energy spacing of a specific vibrational mode of the molecular system [153]. These hot vibrational modes were probed with a second laser pulse, possessing a wavelength that allows for a resonant Raman transition out of the vibrationally excited states, resulting in an anti-Stokes signal. The time-scale of cooling processes for specific normal modes was determined, giving valuable information about the coupling between the molecular system and the bath. A similar experimental scheme on the picosecond time scale was used by Werncke et. al to explore the repopulation of vibrational modes after pumping para-nitroaniline into a charge transfer state [154]. They observed the time-dependent anti-Stokes signal from different vibrational modes in the electronic ground state, which was generated by a time-delayed probe laser, that is in resonance to the electronic ground state absorption. Here, the kinetics of the different modes allows for determining the mechanism with which different vibrational modes are populated. These kinetics show the time scale of internal vibrational energy redistribution among the different vibrational modes.

A number of experimental schemes are described in the literature, that utilize non-linear Raman interactions for exploring transient states and their vibrational dynamics. The recently developed technique of femtosecond stimulated Raman scattering (FSRS) proved to be a very powerful and highly valuable mode sensitive tool [155,156]. It combines the broadband nature of fs laser pulses with high spectral resolution, which is possible since the vibrational modes are excited by a narrow-band ps Raman pump-pulse and only the probe process utilizes a broadband fs pulse. Thus, the time resolution is defined by the cross-correlation time between the initial pump, which is used to prepare the transient species, and the Raman *probe* pulse, whereas the spectral resolution is governed by the bandwidth of the narrow-band Raman *pump* pulse. FSRS was successfully applied to monitor the temporal evolution of the  $S_1$  vibrational spectrum of  $\beta$ -carotene during the  $S_0/S_1$  IC [157,158].

Coherent anti-Stokes Raman scattering (CARS) offers a variety of degrees of freedom together with substantial signal strength providing high flexibility and sensitivity. Application of the CARS process to the investigation of the vibrational dynamics in

the excited state of polyatomic molecules allows for selective observation of time-dependent changes in specific vibrational modes [159].

A significant experiment for establishing third-order interactions as a probe mechanism of transient states in a pump-probe scheme was performed in the group of Zewail [160]. In the experiment, degenerate four-wave mixing (DFWM) was used as a probe mechanism for probing the dissociation dynamics of sodium iodide in the gas phase. Here, the mechanism and state selectivity with which third order interactions interrogate vibrational states in transient populations was established. This was accomplished by the comparison of pump-DFWM and pump-control-DFWM schemes with classical pump-probe experiments using laser induced fluorescence in the detection of the probe step.

There are also a variety of experimental schemes that do not use Raman transitions to obtain mode-specific information of transient states: e.g. time-resolved photoelectron spectroscopy [161] and transient infrared absorption spectroscopy [162] have proved to be powerful methods for observing internal conversion selectively with respect to the nuclear dynamics coupled to this type of electronic transition.

Recent advances in pulse-shaping techniques made it possible to vary the envelopes, polarization directions, durations, and time intervals, to tune the frequencies, and even to control the phases of optical pulses. By scanning these various parameters it is possible to custom design a multiple-pulse technique for a specific application (as is routinely done in nuclear magnetic resonance NMR). One option is to vary time-intervals between short pulses in analogy to conventional four-wave-mixing techniques, but any other choice of parameters is possible. Information concerning molecular structure and dynamics can be extracted from  $n$ -dimensional correlation plots, obtained by varying  $n$  parameters of a pulse train [163]. Time-resolved two-dimensional pump-probe infrared spectroscopy was applied by P. Hamm et al. to investigate in detail the structure and the femtosecond dynamics of the marker band of peptides and proteins, amide I band [164].

In this chapter, experimental work to characterize the dynamics of vibrational modes of stilbene-3 upon photoexcitation into the  $S_1$ -state is presented. In order to gain insight into the mechanism of the photoinduced structural rearrangement involving the C=C-bonds a femtosecond pump-CARS scheme was employed [165].

## 7.1 Experimental details

The pump and the probe pulses within the CARS-scheme having the same color are generated by dividing the output of one OPG into two independent beams of approximately the same intensity by means of 50/50 beam-splitter. The output of the second OPG is split by means of a 30/70 beam-splitter. While the beam having a lower intensity is employed as the Stokes pulse within the CARS-process, the beam with higher intensity is used to generate the UV-pump pulses through frequency doubling in a BBO crystal. A dichroic mirror is employed to separate the generated UV light from the residual fundamental light. In order to align the polarization of the auxiliary UV-pump beam parallel to the polarization of the CARS-pulses, it was rotated by  $90^\circ$  by passing through a Berek compensator. All beams were made parallel and focused into the sample by means of a spherical mirror of 20 mm focal length. The generated CARS signal was spatially separated from the laser beams transversing the sample by applying a folded BOXCARs beam geometry [166]. The CARS-signal was recollimated by means of an achromatic lens and coupled into a monochromator, where it was spectrally dispersed and detected by a CCD camera. The pulse energies used to perform the experiments presented here were typically  $0.3 \mu\text{J}$  for the initial-pump beam and less than  $0.1 \mu\text{J}$  for each of the CARS pulses at the sample volume. The wavelength of the auxiliary UV-pump was chosen to be 380 nm in all experiments, thus the color of Stokes-laser was set to be 760 nm throughout all CARS-experiments presented here. The wavelength of the CARS-pump and -probe pulses was varied from 600 nm ( $\Delta\tilde{\nu} = 3000 \text{ cm}^{-1}$ ) to 720 nm ( $\Delta\tilde{\nu} = 400 \text{ cm}^{-1}$ ), allowing for a complete coverage of the relevant part of the Raman spectrum of stilbene-3.

For performing transient absorption measurements the UV-pump pulse was also centered at 380 nm and was generated as described above. The white light used as a probe and a reference beam was obtained by focusing a small fraction (typically  $2 \mu\text{J}$ ) of the CPA-1000 output into a 3-mm-thick Sapphire window. The resulting supercontinuum pulses were approximately 1 ps in duration and possessed a spectral range that covered the entire visible spectrum. A spherical mirror with 20 mm focal



length was employed to focus the beams into the sample the way that pump and probe beams were overlapping within the sample volume while the reference passed through the sample without being overlapped with a pump beam. For detection, the probe and the reference beams were sent to the spectrometer, dispersed and vertically shifted with respect to each other. The CCD was split into two symmetric parts, thus allowing detecting the probe- and the reference-beam simultaneously. Difference absorption spectra were then recorded as a function of delay between pump- and probe-pulse.

The time-resolved measurements were performed on stilbene-3 (Lambda Physics) dissolved in a 1:1 water/ethanol mixture. The concentration was adjusted to have an optical density of 2 at 380 nm, i.e. at the wavelength used for the UV-pump pulses. The sample was placed in a rotating cell in order to avoid thermal effects. The rotation speed was adjusted to ensure that each pulse interacted with a fresh portion of the sample (approx. 20 Hz).

Cw Raman measurements of stilbene-3 dissolved in a 1:1 water/ethanol mixture were performed with an excitation wavelength of 514 nm (argon ion laser Spectra Physics Model 2085)

## 7.2 Materials. Stilbene-3 system

Stilbene-3 (stilbene-420; 4,4'-bis(2-sulfoethyl)biphenyl disodium salt) is a highly efficient photostable laser dye, soluble in water and alcohols. It consists of two stilbene-like parts, connected by single carbon-carbon bond (Fig. 7.1). By analogy with biphenyl, stilbene-3 possesses a twisted configuration around this bond in the electronic ground state. The order of the central bond increases upon the excitation from the ground to the first electronic excited state and both stilbene-like parts lie then in the same plane [167]. Stilbene-3 finds its application not only as conventional laser dye, but also as a fluorescent probe in optical fiber sensor arrays [168] or as multi-photon absorber for broadband optical limiting [169]. In all cases, it is the extremely high (multi-photon) absorption cross-section that makes this chromophore so useful.

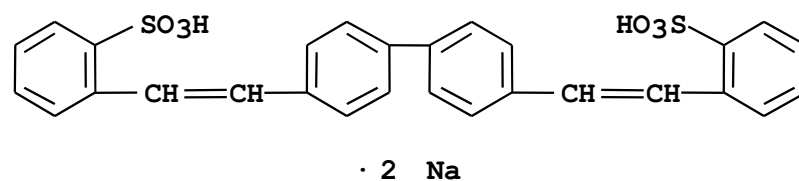


Figure 7.1: Chemical structure of stilbene-3.

### 7.2.1 Raman spectrum of stilbene-3

In order to obtain information about the vibrational modes in the electronic ground state of stilbene-3, non-resonant Raman measurements were performed. Cw Raman spectrum of an 1:1 ethanol/water solution of stilbene-3 is shown in Fig. 7.2. The spectrum is dominated by a group of C=C double bond stretching modes around  $1600\text{ cm}^{-1}$  and a group of deformation modes at  $1191\text{--}1333\text{ cm}^{-1}$  (see Table 7.1). The large wavenumber difference between these two groups of bands allows the use of broadband fs-laser pulses to separately investigate the dynamics of the different types of modes by adjusting the wavenumber difference between the Stokes and the pump laser of the CARS process to be Raman resonant with these modes. A detailed vibrational assignment can be found in Table 7.1 together with further vibrational data obtained by Werncke et al. [170] in resonant-CARS experiments, using pulses of 10 ns duration.

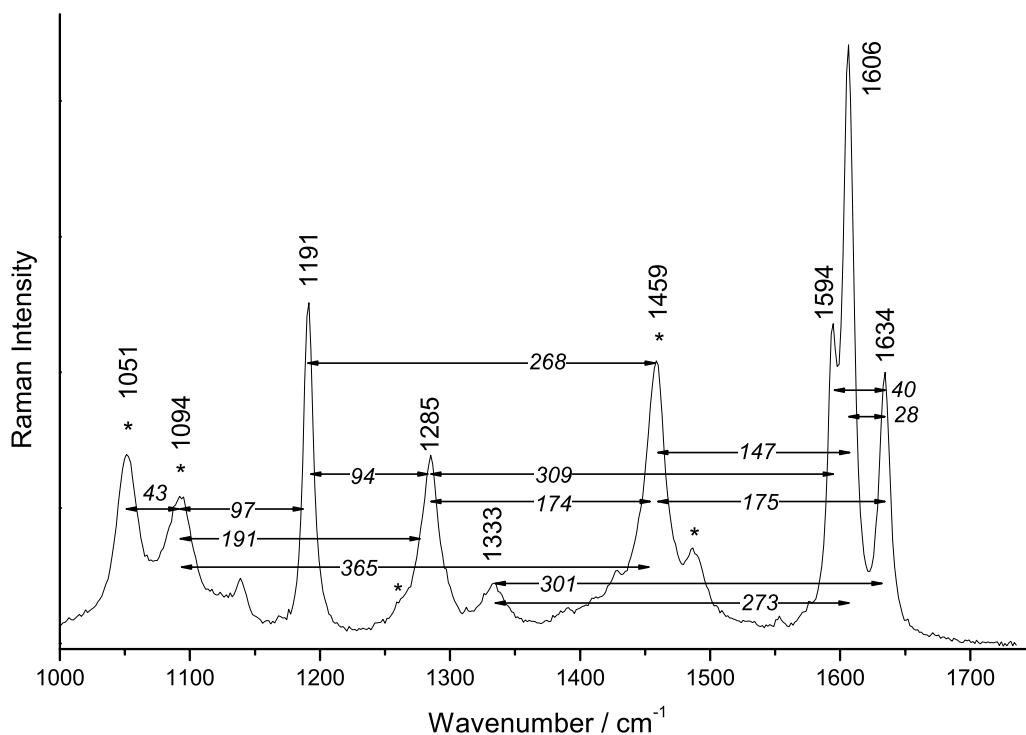


Figure 7.2: Raman spectrum of stilbene-3 dissolved in 1:1 ethanol/water mixture. Excitation wavelength 514 nm.

$\tilde{\nu}_{Raman} / \text{cm}^{-1}$	$\tilde{\nu}_{CARS}^{S_0} / \text{cm}^{-1}$ <sup>1)</sup>	$\tilde{\nu}_{CARS}^{S_1} / \text{cm}^{-1}$ <sup>1)</sup>	Assignment <sup>1)</sup>
1634	1620(m)	1587(vs)	C=C str olefin
1606	1593(vs)	-	C=C str ring
1594	1580(s)	1563(w)	-
1333	1340(m)	1335(m)	C <sub>O</sub> -C <sub>O</sub> -H bend
1285	1280(m)	-	-
1191	1189(s)	1199(s)	C-H def olefin + C <sub>O</sub> -Ø str

Table 7.1: Peak positions ( $\tilde{\nu}_{Raman}$ ) of ground-state Raman bands (see Fig. 7.2), CARS peaks positions for the ground ( $\tilde{\nu}_{CARS}^{S_0}$ ) and the excited ( $\tilde{\nu}_{CARS}^{S_1}$ ) states, and assignment for stilbene-3. The labels in brackets refer to the intensity of the respective mode: vs: very strong, s: strong, m: medium, w: weak. In assignment, Ø: phenyl ring, C<sub>O</sub>: olefinic carbon.

<sup>1)</sup> according to Werncke et al. [170]

## 7.3 Results and discussion

### 7.3.1 Transient $S_n \leftarrow S_1$ absorption

In order to selectively interrogate the population dynamics taking place in the ground as well as in the excited state, electronic resonance enhancement of the excited state CARS process can be particularly useful. To obtain information about the electronic resonances available in the first excited singlet state and in order to estimate the excited state lifetime, transient absorption spectra of stilbene-3 were measured as a function of delay time between a fs UV-pump pulse, on the red side (380 nm) of the ground-state absorption peak at 350 nm, and supercontinuum probe-pulse.

It was found, that the excited state absorption covers the whole visible spectrum showing a maximum in the transient absorption at around 650 nm (see upper panel of Fig. 7.3). Lower panel of Fig. 7.3 displays the ground state absorption of stilbene-3 dissolved in a 1:1 ethanol/water mixture. It can be clearly seen that the ground state absorption spectrum of stilbene-3 lies in the ultraviolet and is spectrally well separated from the maximum transient absorption of the  $S_1$ -state. Therefore, the signal obtained from the excited state CARS can be selectively enhanced by choosing the wavelengths of the lasers involved in the process to lie within the excited state absorption. Figure 7.3, lower and upper panels, show the spectra of the pulses used in pump-CARS experiments together with the absorption spectra of ground and excited state.

The lifetime of the excited state could not be determined from the transient absorption measurement due to limited time delay offered by the mechanical delay stages (650 ps maximum delay). Nevertheless, the  $S_1$ -lifetime of stilbene-3 could be estimated to be larger than 1 ns (see also [167]).

### 7.3.2 Pump-CARS

In the pump-CARS experiment, the pump- and the Stokes-pulses interact simultaneously with the molecular sample, whereas the probe pulse within the CARS-process is delayed by a constant time  $\Delta t_1 = 300$  fs (see Fig. 5.5) relative to the pump/Stokes

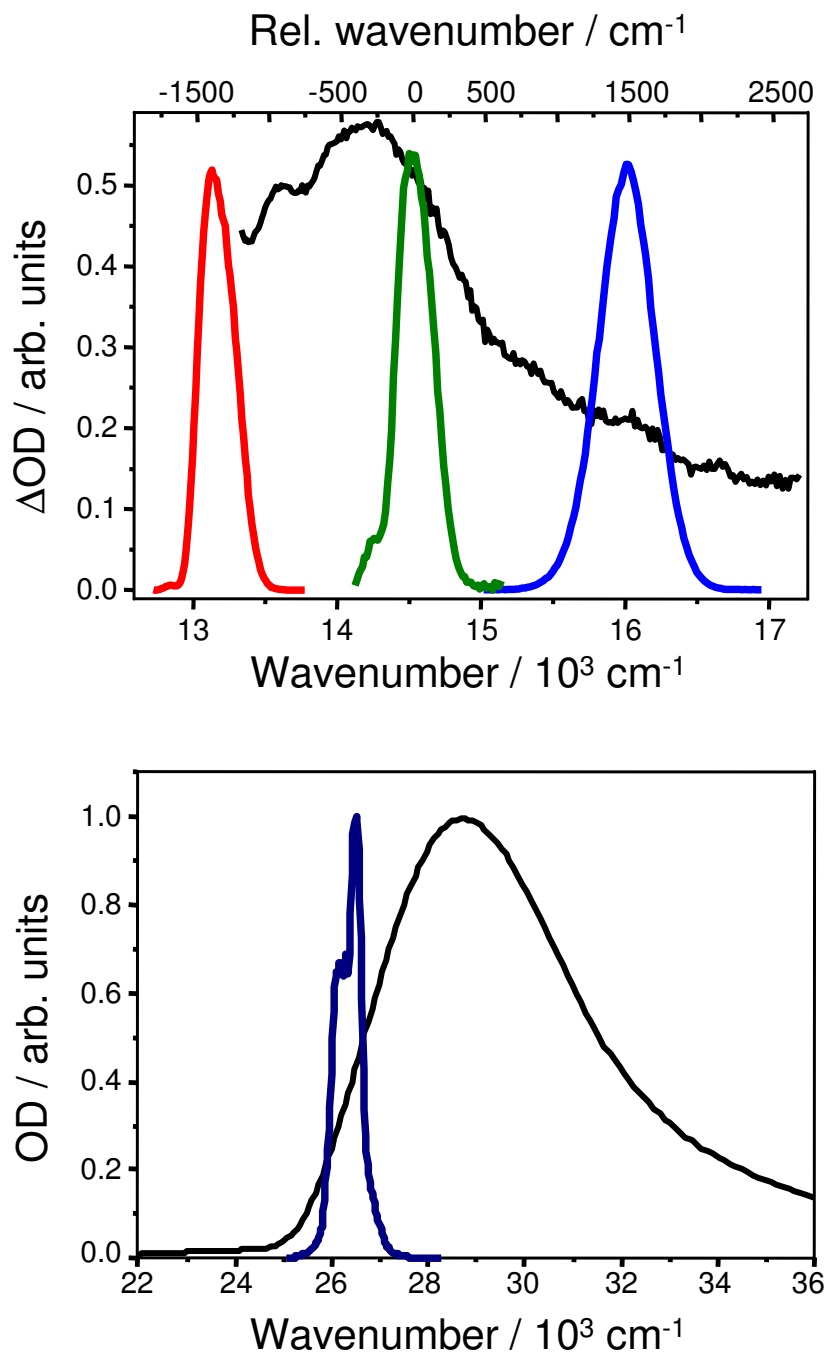


Figure 7.3: Lower panel, ground-state absorption spectrum of stilbene-3 (black line) together with the spectrum of the UV-pump pulse (dark blue line); upper panel, difference absorption spectrum of the  $S_1$  state of stilbene-3 (black line), spectrum of Stokes pulse (red line), spectrum of CARS-pump pulse (green line), spectrum of anti-Stokes signal (blue line).

pulse pair in order to suppress any electronically non-resonant contributions from the solvent and stilbene-3 species in the ground state. The intensity of the anti-Stokes signal is then recorded as a function of delay time  $\Delta t_1$  between the initial UV pump-pulse and the CARS pulses.

In Fig. 7.4 is shown the transient CARS signal recorded by tuning the pump and Stokes pulse to a wavenumber difference of approximately 1600 as well as 1200  $\text{cm}^{-1}$  and monitoring the integrated anti-Stokes signal correspondingly between 1510 and 1680  $\text{cm}^{-1}$  (panel **A**) as well as 1122 and 1290  $\text{cm}^{-1}$  (panel **B**) in the spectrally dispersed anti-Stokes signal. The long-time behavior of the two transients is very similar. Both show an exponential decay with a time constant of approximately 1.4 ns. This decay is attributed to the life-time of the electronically excited state [167]. The time-constant determined in this measurement is in good agreement with the results of the transient absorption measurements presented above.

However, the population dynamics show a substantially different behavior on a shorter time scale. When monitoring the CARS-signal integrated between 1122 and 1290  $\text{cm}^{-1}$ , a relatively fast decay component with a time constant of approximately 5 ps can be observed. In contrast to this, the CARS-signal integrated between 1510 and 1680  $\text{cm}^{-1}$  displays an exponential rise with approximately the same time constant of 5 ps.

### 7.3.3 Time-domain CARS

In order to clarify the origin of the difference observed in the dynamics, further experiments were carried out in which the evolution of the Raman bands in the ground and first excited state of stilbene-3 are recorded by resolving the CARS process in time. This is achieved by monitoring the CARS signal as a function of delay time between pump- and probe-pulses within the CARS process ( $\Delta t_2$  in Fig. 5.5), which corresponds to a classical time-domain CARS experiment [44, 171, 172]. By choosing the relative wavenumber difference between the broad band pump- and Stokes-pulses to overlap several vibrational modes, beats can be observed due to time-dependent phase shifts between different contributions to the CARS signal originating from

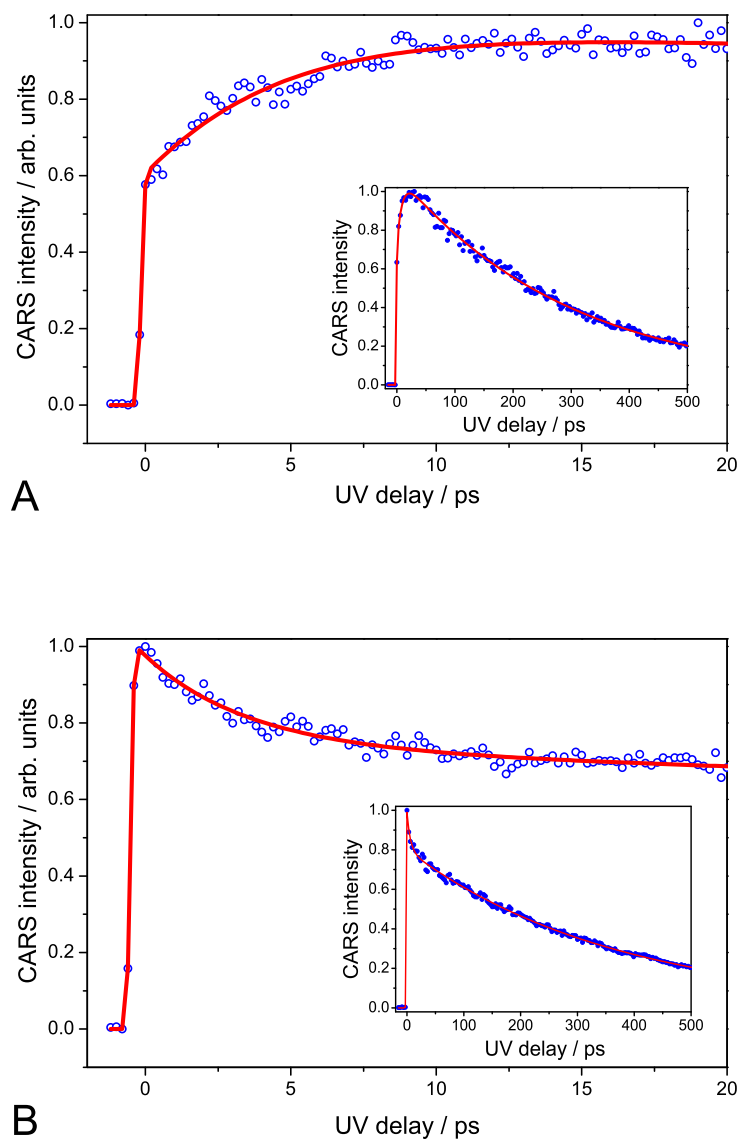


Figure 7.4: Transient CARS signal of stilbene-3 integrated between **A** 1550 and 1850  $\text{cm}^{-1}$  and **B** 1100 and 1350  $\text{cm}^{-1}$  relative shift to the maximum of the CARS-pump spectrum as a function of the delay to the UV-pump,  $\Delta t_1$  (see Fig. 5.5). Insets show the CARS intensity for longer time delays (up to 500 ps). Circles represent the experimental data, solid lines - the fitted data.

respective vibrational modes. The specific situation is considered in the work of Heid et. al. [173], where the anti-Stokes signal is recorded two-dimensionally, i.e., as a function of delay time and simultaneously spectrally dispersed, in order to achieve a detailed mapping of the vibrational dynamics of polyatomic molecules in solution.

In the experiments presented here, the relative wavenumber difference between the pump- and the Stokes-pulses was varied from 1100 to 1600  $\text{cm}^{-1}$  in order to span a wavenumber region of 1000–1700  $\text{cm}^{-1}$ , i.e. coherently excite all modes observed in the Raman spectrum shown in Fig. 7.2. For the excited-state measurements the delay between the UV-pump and the CARS pump/Stokes pair ( $\Delta t_1$  in Fig. 5.5) was set to 20 ps to ensure that vibronic relaxation is finished. The CARS lasers were in resonance with the  $S_1$ - $S_n$  transitions, in order to suppress any ground state contribution. In order to guarantee, that the observed mode beating exclusively originates from stilbene-3 molecules in the excited state the power of the CARS pulses was strongly reduced, so that no signal was observed in the absence of the UV-pump pulses. Figure 7.5 shows the CARS spectra as a function of the delay time  $\Delta t_2$ , obtained in the absence (panel **A**) as well as in the presence (panel **B**) of the UV-pump. Complex oscillating signals superimposed on exponentially decaying components are observed for both cases. The dependence of the CARS intensity at certain wavelength position on delay time  $\Delta t_2$  is shown for illustration as black curves in Fig. 7.5.

A Fourier analysis of the beating pattern allows for an extraction of the wavenumber differences between modes coherently excited in the CARS-process. A detailed description of this procedure can be found in the work of Heid et. al. [173] where it is pointed out that an assignment of the peaks to certain vibrational modes is possible because of the additional information about the CARS peak location along the CARS wavenumber axis in the FFT amplitude plot which is obtained by a spectrally resolved detection of the CARS signal. Briefly, a fast Fourier transformation (FFT) was performed for the CARS signal as a function of the delay time  $\Delta t_2$  at each wavelength position (see, e.g. black curves in Fig. 7.5). The exponential decay component of the original signal has been subtracted prior to the FFT transformation, retaining only the oscillating component. The wavelength position of the CARS signal was converted to the relative wavenumber position using the relation  $\tilde{\nu}_{CARS} = 10^7/\lambda_{CARS} - 10^7/\lambda_{pump}$ ,



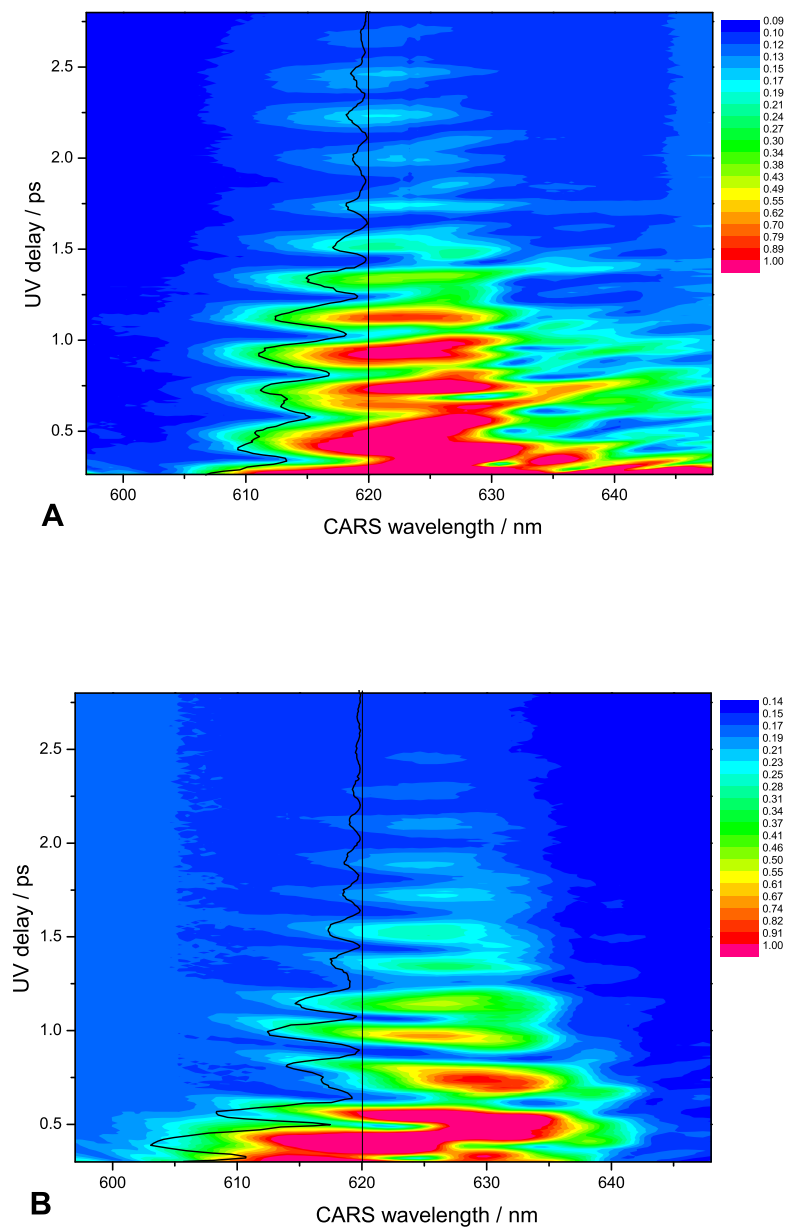


Figure 7.5: CARS spectra of stilbene-3 plotted as a function of the delay time  $\Delta t_2$  (see Fig. 5.5). Difference between pump and Stokes is tuned for both cases to approximately  $1400\text{ cm}^{-1}$  (680 nm). Panel **A**, ground state CARS (UV-pump is off), panel **B**, excited state resonance CARS (UV-pump is on,  $\Delta t_1 = 20\text{ ps}$ ). The black curves are cuts through the data at a CARS wavelength position of 620 nm.

where  $\tilde{\nu}_{CARS}$  is CARS wavenumber position in  $\text{cm}^{-1}$ ,  $\lambda_{CARS}$  is CARS wavelength position in nm, and  $\lambda_{pump}$  is CARS pump position in nm. The FFT amplitude spectrum was then plotted as a function of the CARS wavenumber (Fig. 7.6).

The spectral resolution of the time-resolved CARS is limited on the one hand by the cross-correlation time of the laser pulses involved in the CARS process (FWHM  $\approx 80$  fs  $\equiv \sim 420$   $\text{cm}^{-1}$ ) and also by the available scan length ( $\Delta t \approx 3$  ps  $\equiv \sim 11$   $\text{cm}^{-1}$ ) which is defined by the dephasing time of the coherent superposition of the excited vibrational modes.

Figure 7.6 shows the FFT amplitude plot calculated for the ground (panel A) and the excited (panel B) state CARS signals while tables 7.2 and 7.3 summarize the observed results. Table 7.2 compares the peaks locations of the FFT amplitude, calculated for the ground-state CARS signal with the data available from the cw-Raman measurements (see Fig. 7.2 and table 7.1). Positions of the peaks on two-dimensional FFT plot are defined as coordinates of the FFT amplitude local maxima. The peak position along the FFT wavenumber axis corresponds to the wave number differences of two coherently excited vibrational modes of stilbene-3 or ethanol, and the position of the peaks along the CARS wavenumber axis is approximately given by the arithmetic mean wavenumber position of the two beating modes.

The analysis of the presented data shows, that the main features of the ground state beating pattern are due to beatings of the strong ethanol band at  $1459$   $\text{cm}^{-1}$  with the 4 strong stilbene-3 bands at  $1634$ ,  $1606$ ,  $1285$  and  $1191$   $\text{cm}^{-1}$ . Low wavenumber beatings between the 3 strong bands at around  $1600$   $\text{cm}^{-1}$  are also clearly visible. Overall the very good agreement between the expected and measured FFT amplitude peaks confirms the reliability of the applied method.

Table 7.3 presents the peak positions of the FFT amplitude for the excited-state CARS signal. The following arguments were used to derive the wavenumber positions of the vibrational modes exciting the beating pattern observed in the first electronically excited state of stilbene-3: (I) The C-H deformation modes at  $1333$  and  $1191$   $\text{cm}^{-1}$  do not change their wavenumber positions upon photo-excitation from the  $S_0$  into the  $S_1$  state (see table 7.1) [170] and (II) only excited-state stilbene-3 modes and no solvent modes contribute to the CARS signal due to the strong  $S_1$ - $S_n$  resonant

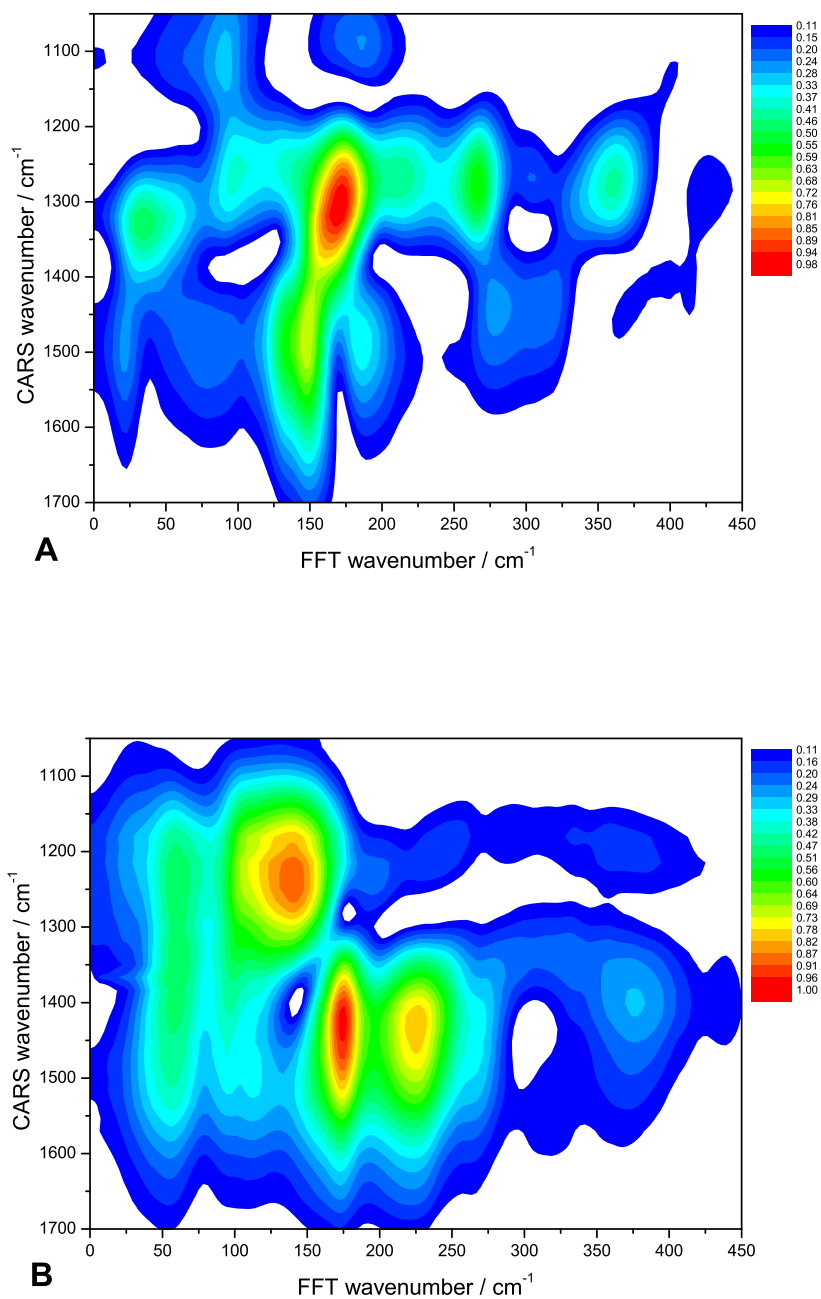


Figure 7.6: FFT amplitude of the oscillating contributions to the time-domain CARS signal from the (A) ground and (B) excited state stilbene-3 in an ethanol/water solution plotted as a function of the CARS signal relative wavenumber.

Table 7.2: FFT wavenumber ( $\tilde{\nu}_{FFT}$ ) and CARS wavenumber ( $\tilde{\nu}_{CARS}$ ) location of the peaks in the ground-state CARS FFT amplitude plot (Fig. 7.6, A). The peaks correspond to quantum beating between vibrational modes  $\tilde{\nu}_j$  and  $\tilde{\nu}_k$  of stilbene-3 and ethanol (see Fig. 7.2.)

$\tilde{\nu}_{FFT}/\text{cm}^{-1}$	$\tilde{\nu}_{CARS}/\text{cm}^{-1}$	$\tilde{\nu}_j/\text{cm}^{-1}$	$\tilde{\nu}_k/\text{cm}^{-1}$	$\tilde{\nu}_j - \tilde{\nu}_k/\text{cm}^{-1}$
149	1501	1606	*1459	147
189	1507	1634	*1459	175
176	1350	1285	*1459	174
269	1331	1191	*1459	268
363	1302	*1094	*1459	365
26	1584	1606	1634	28
305	1460	1333/1285	1634/1594	301/309
95	1255	1191	1285	94
274	1430	1333	1606	273
90	1121	1191	*1094	97
47	1573	1594	1634	40
186	1187	1285	*1094	191
50	1060	*1051	*1094	43

Table 7.3: FFT wavenumber ( $\tilde{\nu}_{FFT}$ ) and CARS wavenumber ( $\tilde{\nu}_{CARS}$ ) location of the peaks in the excited-state CARS FFT amplitude plot (Fig. 7.6, B). Positions of the excited-state vibrational modes  $\tilde{\nu}_m$  and  $\tilde{\nu}_n$  of stilbene-3 are recovered from the correspondent FFT peaks locations (for more details see text).

$\tilde{\nu}_{FFT}/\text{cm}^{-1}$	$\tilde{\nu}_{CARS}/\text{cm}^{-1}$	$\tilde{\nu}_m/\text{cm}^{-1}$	$\tilde{\nu}_n/\text{cm}^{-1}$	$\tilde{\nu}_m - \tilde{\nu}_n/\text{cm}^{-1}$
176	1433	1510	1333	177
231	1433	1570	1333	237
244	1225	1333	1089	244
380	1428	1570	1191	379
139	1261	1333	1191	142
483	1431	1570	1089	481
58	1421	1570	1510	60
428	1418	1510	1089	421
324	1335	1510	1191	319
98	1168	1191	1089	102

enhancement. Considering these facts the FFT analysis of the excited state beating pattern reveals that the three C=C double bond stretch modes around  $1600\text{ cm}^{-1}$  change their wavenumber position upon excitation to the  $S_1$  state. However two new bands at  $1510$  and  $1570\text{ cm}^{-1}$  due to stretch vibrations of the weakened C=C double bond in the excited state can be seen. The band at  $1570\text{ cm}^{-1}$  was also observed in the resonance Raman spectrum of trans-stilbene in the  $S_1$  state [174–176] and in the ps resonance CARS spectrum of stilbene-3 [170]. Additionally, the band at  $1089\text{ cm}^{-1}$  was assigned to a C-C-H bending motion. This assignment is based on excited state ps time-resolved Raman measurements of trans-stilbene performed by Gustafson et al. who observed a mode at  $1078\text{ cm}^{-1}$  in the  $S_1$  state Raman spectrum [174]. They assigned this vibration to a C-C-H bending mode which changes its wavenumber position from  $1028$  to  $1078\text{ cm}^{-1}$  upon photoexcitation from the  $S_0$  into the  $S_1$  state.

With the information gained from the experiments described above the following model for the population flow within stilbene-3 is proposed: for the deformation modes at  $1191$ – $1333\text{ cm}^{-1}$ , population flow occurs between different vibrational levels of the same mode. This vibrational cooling populates vibrational levels with lower Franck-Condon factors for the interrogation with the CARS probe and leads to the observed fast decay in the CARS signal. On the other hand, the behavior of the CARS signal recorded at around  $1600\text{ cm}^{-1}$  within the first 5 ps after photo-excitation reflects the change in the structure of vibrational modes with a high contribution of C=C symmetric stretch motion in stilbene-3. The rise of the CARS signal at the corresponding Raman wavenumber is a result of a higher value of Franck-Condon factors for the equilibrium geometry of these modes in the excited state and the dynamics observed within the first 5 ps after UV excitation show the geometrical rearrangement of the C=C double bonds on the excited state potential surface. This conclusion is also supported by the observed dynamics of the ethylenic bond wavenumber of trans-stilbene in the first excited state, reported by Qian et. al. [175].

## 7.4 Conclusion

In the presented experiments, the pump-CARS technique was applied to disentangling the dynamics of various vibrational degrees of freedom within the excited-state potential-energy surface of stilbene-3 following photo-excitation at 380 nm. In the experimental scheme described in this work, a CARS process serves as a probe mechanism for selectively monitoring the time-evolution of specific vibrational modes within an electronically excited state.

For attaining auxiliary information of the stilbene-3, a cw Raman spectrum of the ground state and the transient absorption spectrum of the first excited state of stilbene-3 were measured in order to obtain information about vibrational as well as electronic resonances of this molecular system. By choosing the color of the three fs lasers involved in the CARS process to be within the absorption profile of the  $S_1$ -state, the dynamics of excited state molecules could be separated from the CARS signal of the ground state. Adjusting the wavenumber difference between pump- and Stokes-laser allows for the separation of dynamics in specific vibrational modes within the CARS signal.

Substantially different short-time dynamics were observed for two main groups of modes. The CARS signal originating from deformation modes at 1189–1333  $\text{cm}^{-1}$  decays monoexponentially with a time constant of about 5 ps, reflecting vibrational cooling within the selected modes. In contrast, the CARS signal from C=C double bond stretching vibrations at 1600  $\text{cm}^{-1}$  rises with approximately the same time constant, showing the reorganization of the bonds coupled to the electronic transition from the electronic ground to the  $S_1$ -state.

Time- and wavenumber-resolved CARS measurements were performed to demonstrate changes in the vibrational level structure upon photo-excitation. A shift in the wavenumber positions of the C=C double bond stretch modes was detected proving the origin of the pump-CARS signal behavior at 1510–1680  $\text{cm}^{-1}$  to be due to bond rearrangement upon transition from the ground to the first excited state.

Finally, it could be shown that the technique of fs pump-CARS allows for selectively monitoring the time-dependent behavior of distinct vibrational modes within

the excited state PES of polyatomic molecules such as stilbene-3, directly after photoexcitation with fs-UV pulses. The excited state time-resolved CARS mode beating technique proved to be a highly capable method to reconstruct the vibrational level structure in the excited states of polyatomic molecules.





## Chapter 8

# Conclusion - Zusammenfassung

### 8.1 Conclusion

In the first part of the work presented within this thesis possibilities of nonlinear frequency conversion in solid state media of low-energy ultrashort laser pulses are investigated. As frequency conversion techniques impulsive stimulated Raman scattering (ISRS) in a potassium gadolinium tungstate ( $\text{KGd}(\text{WO}_4)_2$ , KGW) crystal and supercontinuum generation in micro-structured and tapered fibers are applied. In the second part applications of femtosecond time-resolved four-wave mixing spectroscopical methods for monitoring relaxation processes in photoexcited polyatomic molecules are demonstrated. In doing so transient population grating (TG) experiments to investigate the electronic relaxation pathways in azulene derivatives and coherent anti-Stokes Raman scattering (CARS) experiments to monitor the excited-state vibrational energy redistribution in stilbene-3 are applied.

The motivation underlying the first part of the work is given by the necessity for alternative methods of frequency conversion of a coherent radiation. Despite the possibility of generating the entire visible spectrum by means of different wave-mixing schemes, the characteristics of the produced radiation often do not meet the desired specifications or the efficiency is too low. In particular, effective nonlinear frequency

conversion of low energy laser radiation is hindered due to intensity thresholds for the majority of nonlinear processes. In the presented work, nonlinear frequency conversion in solid state media of low-energy fs laser pulses was investigated. The strategies of the frequency conversion used in the experiments presented in this work are the following: (I) suppression of the competing nonlinear processes by use of special pumping geometry (Bessel beam) allowing for an increased efficiency of the desired frequency conversion mechanism (ISRS); (II) a high level confinement of the electric field increasing the interaction with matter and relaxing phase matching conditions for nonlinear processes leading to a ultrabroadband supercontinuum generation. Applications of the proposed radiation sources can be found in optical metrology, ultrafast photonics, biomedical optics, etc.

Impulsive stimulated Raman scattering occurs when ultrashort laser pulses pass through Raman active media possessing high Raman cross-sections. As a result of the highly non-stationary field-matter interaction, stimulated scattering is observed which is frequency shifted and substantially broadened as compared to the initial (pump) pulses. The strong deviation of the observed spectral positions of the Stokes and anti-Stokes maxima from the spontaneous Raman lines of the investigated medium could be found. The nature of the scattered spectrum originates from the transient character of the buildup of the vibrational response. Within the short pulse duration, which is comparable to the vibrational period of the medium, a quantum oscillator has no time to exhibit its vibrational properties, and therefore it cannot be resonantly driven by the laser field. On the other hand, the spectrum of the pulse initially contains frequency components necessary for the stimulated Raman process to occur, and thus a sort of nonlinear self-conversion can take place at field intensities much lower than the threshold ones for the SRS buildup starting from spontaneous noise.

The efficiency of Raman conversion of short pulses is reduced by the group velocity mismatch (GVM) between pump and Stokes waves caused by dispersion of the Raman medium and by the competition with other nonlinear processes. As a result, the dominant non-linear process in condensed media, when pumping with a usual Gaussian beam is femtosecond continuum ('white light') generation. However a strong enhancement of the ISRS in a Bessel beam is achieved by a correction of

the GVM, resulting from the angular dispersion of the refracted Bessel beam, and a suppression of the self-phase modulation and other non-linear processes due to non-collinearity of the partial plane waves constituting the Bessel beam.

Theoretical and experimental premises were used to demonstrate Raman frequency conversion of 70 fs laser pulses in the regime of ISRS in a solid-state material (KGW crystal) for the first time. Bessel beam pumping proved to be an excellent solution for the enhancement of ISRS giving additional advantage of spatial separation from the incoming (pump) light.

Nevertheless white light generation is not always unwanted it finds a great number of applications in diverse fields. A cheap and effective way to produce femtosecond supercontinuum is provided by optical fibers, where a scope of non-linear processes get enhanced due to a confinement of the electric field. In order to increase the efficiency of SC generation, multiple-core microstructure fibers having six submicron-diameter cores surrounding a larger central core with a diameter of 2-5  $\mu\text{m}$  were used. Such a MS fiber design combines the ideas of a holey fiber and a tapered fiber by integrating several small core high-refractive-index-step fibers into a bundle, allowing the total energy of SC emission to be increased. Additionally, MS fibers of a very large length can be fabricated (in tapered fiber, e.g., taper waist length is typically limited to tens of centimeters).

Efficient SC generation in multiple-core MS fibers was compared for two experimental strategies. In the first case fs laser pulses were coupled into one or several submicron side-threads, in the second case the pulses were sent through the central core. Significant broadening of the transmitted radiation was observed in the first case, when the pump was tuned close to the zero-GVD wavelength of the investigated MS fiber. The features of the observed SC generation were indicative of parametric wave-mixing, stimulated Raman scattering, and soliton-fission scenarios. SC generation in a large central core was characterized by a much lower efficiency. Furthermore an isolated anti-Stokes component could be efficiently generated in the central core as a result of four-wave mixing processes involving higher-order wave-guide modes.

The goal of the second part of the presented work was to demonstrate the capabilities of various four-wave mixing (FWM) processes to investigate vibrational as

well as electronic relaxation pathways of photo-excited polyatomic molecules being important for a better understanding of the initial dynamics and the quantum control of photo-induced chemical reactions.

As an example of the capability of the transient grating (TG) technique to resolve low amplitude dynamical processes with high temporal resolution, an excited-state coherent wave-packet motion was observed during the  $S_1/S_0$  internal conversion in azulene.

The capabilities of the TG technique were further used to determine the characteristic time constants of the electronic relaxation pathways of azulene derivatives with high accuracy. Additionally the pump-probe transient absorption (TA) technique was used to retrieve spectral information about the excited-state species generated after initial photoexcitation. The existence of a long-living 'dark' state was proposed for the investigated class of molecules. The combination of TA- and TG-spectroscopy allows a comprehensive spectral and temporal characterization of the excited state dynamics.

The reorganization of chemical bonds in a polyatomic molecule upon excitation to an excited electronic state is accompanied by the changes in nuclear geometry. Changes in the equilibrium positions of the atoms, i.e. of the normal modes of the molecule, are orders of magnitudes slower than electronic rearrangements and can therefore be monitored and probably influenced by laser pulses of 100 fs duration. Femtochemistry is a correspondent branch of science, which deals with ultrafast dynamical processes in molecules.

Within this work the model system stilbene-3 was investigated by means of the fs pump-CARS technique, which allows one to monitor the population of specific vibrational modes upon initial photoexcitation. Raman-resonances are utilized to enhance the signal originating from the desired vibrational mode, making the CARS process to serve as mode-specific filter. Furthermore electronic resonances help to discriminate between the ground and excited state signals.

An analysis of the observed time-dependency of the CARS signal from the electronic excited state proved that for the stilbene-3 molecule the main relaxation mechanism of the C-C-H bending, C-H deformation and C-O stretching modes of Stilbene-

3 upon photoexcitation is vibrational cooling, with a characteristic time constant of around 5 ps. A reorganisation of the stilbene-3 C=C double bonds upon excitation to the electronic excited state could be monitored via the growth of the CARS signal tuned to the double-bond stretching modes. The time constant for this process was found to be also around 5 ps.

In summary, nonlinear frequency conversion in solid state media of low-energy fs laser pulses was investigated. Raman conversion in a white-light-free regime of impulsive stimulated Raman scattering was achieved by pumping a KGW crystal with a Bessel beam. Efficient supercontinuum generation was demonstrated for sub-microjule pulses focused into a MS fiber. The application of four-wave mixing techniques to monitor the excited-state dynamics in polyatomic molecules was demonstrated. Spectral as well as temporal properties of electronic relaxation pathway in azulene derivatives were explored by using transient population grating and pump-probe transient absorption techniques. The time constants of the processes related to vibrational energy redistribution upon initial photoexcitation of stilbene-3 were determined by means of pump-CARS technique, where the CARS process served as an effective mode-selective filter.

## 8.2 Zusammenfassung

In der vorliegenden Arbeit wurden Möglichkeiten der nichtlinearen Frequenzumwandlung niederenergetischer ultrakurzer Laserpulse in Festkörpern untersucht. Als Frequenzkonversionstechniken wurden zum einen die impulsive stimulierte Raman-Streuung in Kalium-Gadolinium-Wolframat-Kristallen (KGW) sowie die Erzeugung eines Superkontinuums in mikrostrukturierten Fasern gewählt. Des Weiteren wurde der Einsatz verschiedener Femtosekunden-zeitaufgelöster Vierwellenmischtechniken zur Untersuchung elektronischer Relaxationsprozessen in polyatomaren Molekülen erprobt. So wurden die verschiedenen elektronischen Relaxationskanäle in verschiedenen Azulenderivaten mittels transientser Populationsgitter ('TG = transient grating') erforscht. Außerdem wurde ein CARS-Prozeß als Probe-Schritt in ein Pump-Probe-Schema eingegliedert, was die Untersuchung der Schwingungsenergie-Umverteilung nach Photoanregung im elektronisch angeregten Zustand von Stilben-3 erlaubt.

Der erste Teil der Arbeit ist motiviert durch die Notwendigkeit alternative und neuartige Methoden zur Frequenzkonversion kohärenter Strahlung zu entwickeln.

Trotz der Tatsache, dass sich nahezu der gesamte sichtbare Bereich des elektromagnetischen Spektrums über verschiedene Wellenmischschemata generieren lässt, erfüllt die erzeugte Strahlung oft nicht die gewünschten Spezifikationen oder die Konversionseffizienz ist zu niedrig. Aufgrund der Tatsache, dass die meisten nichtlinearen Prozesse einen Intensitäts-Schwellenwert aufweisen, ist eine effektive Frequenzumwandlung von niederenergetischer Laserstrahlung ein Problem. In der vorliegenden Arbeit wird daher die Frequenzkonversion niederenergetischer Femtosekundenlaserpulse in Festkörpern untersucht. Dazu wurden die folgenden experimentellen Strategien verwendet: (I) Unterdrückung der konkurrierenden nichtlinearen Prozesse mittels spezieller Pumpgeometrien (Besselstrahl), was zu einer verstärkten Effizienz des gewünschten Frequenzkonversionsmechanismus (ISRS) führt; (II) 'Cofinement' des elektrischen Feldes, wodurch die Wechselwirkung mit der Materie erhöht und die Phasenanpassungsbedingungen für nichtlineare Prozesse gelockert werden, was zur Erzeugung eines Ultrabreitband-Superkontinuums führt. Die vorgeschlagenen

Strahlungsquellen können in der optischen Metrologie, der ultraschnellen Photonik, in der biomedizinischen Optik, etc., zum Einsatz kommen.

Impulsive stimulierte Raman-Streuung tritt auf, wenn ultrakurze Laserpulse ein Raman-aktives Medium mit großem Raman-Streuquerschnitt durchqueren. Aufgrund der nicht-stationären Feld-Materie-Wechselwirkung beobachtet man stimulierte Streustrahlung, welche frequenzverschoben und wesentlich verbreitert im Vergleich zum anfänglichen Pump-Puls ist. So wurde eine starke Abweichung der spektralen Positionen der beobachteten Stokes- und anti-Stokes-Maxima von denen die in spontanen Raman-Streuxperimenten gefunden werden, beobachtet. Der Charakter des Streuspektrums rührt von dem transienten Charakter des Aufbaus der Schwingungsantwort her. Innerhalb der kurzen Pulsdauer, welche vergleichbar mit der Schwingungsperiode des Mediums ist, hat ein quantenmechanischer Oszillator keine Zeit seine Schwingungseigenschaften auszubilden und kann daher nicht resonant durch das Laserfeld getrieben werden. Auf der anderen Seite enthält das Pulsspektrum anfangs Frequenzkomponenten, welche notwendig sind, damit der stimulierte Raman-Prozess stattfinden kann und somit kann eine Art nichtlineare Selbstkonversion für Feldintensitäten viel kleiner als der Schwellenwert für den SRS-Aufbau startend aus spontanem Rauschen stattfinden.

Die Effizienz der Raman-Konversion kurzer Pulse wird durch die Gruppengeschwindigkeits-Fehlanpassung zwischen Pump- und Stokes-Welle, erzeugt durch Dispersion im Raman-Medium und aufgrund der Konkurrenz mit anderen nichtlinearen Prozessen reduziert. Demzufolge ist der dominierende nichtlineare Prozess in kondensierten Medien, sobald mit einem normalen Gauß-förmigen Strahl gepumpt wird die Erzeugung eines Femtosekunden-Kontinuums (Weißlicht). Jedoch lässt sich eine starke Verstärkung der impulsiven stimulierten Raman-Streuung in einem Bessel-Strahl, durch Korrektur der Gruppengeschwindigkeits-Fehlanpassung erreichen, welche durch die Winkeldispersion des gebrochenen Bessel-Strahls und einer Unterdrückung der Selbstphasenmodulation und anderer nichtlinearer Prozesse aufgrund der Nicht-Kollinearität der ebenen Wellen des Bessel-Strahls herrührt.

Theoretische und experimentelle Ansätze wurden verwendet, um die Raman-Konversion von 70 fs Laserpulsen via impulsiver stimulierter Raman-Streuung in

einem Festkörpermateriale (KGW-Kristall) das erste Mal zu demonstrieren. Das Pumpen mittels eines Bessel-Strahls erwies sich als exzellente Lösung für die Verstärkung der impulsiven stimulierten Raman-Streuung mit dem zusätzlichen Vorteil der räumlichen Separierung vom einfallenden Pump-Strahl.

Die Erzeugung von Weißlicht ist nicht immer ein unerwünschter Prozess und findet eine große Anzahl von Anwendungen in diversen Forschungsfeldern. Ein Femtosekunden-Superkontinuum lässt sich preiswert und effizient mittels optischer Fibern erzeugen. Dabei wird der Wirkungsbereich nichtlinearer Prozesse aufgrund eines 'Confinement' des elektrischen Feldes verstärkt. Um die Effizienz der Superkontinuum-Erzeugung weiter zu erhöhen wurden Mehrfachkern-mikrostrukturierte (MS) Fibern mit 6 Submikron-Durchmesser-Kernen, welche einen zentralen Kern mit einem Durchmesser von 2–5  $\mu\text{m}$  umgeben, verwendet. Ein solches MS-Fiber-Design vereint die Idee einer Hohl-Fiber und einer konischen Fiber durch Integration mehrerer Fibern mit kleinem Kern und hohem Brechungsindex zu einem Bündel, was die Gesamtenergie der Superkontinuum-Emission erhöht. Des Weiteren lassen sich MS-Fibern großer Länge herstellen.

Es wurden zwei experimentelle Strategien zur Superkontinuumserzeugung in MS-Fibern verfolgt und deren Effizienz miteinander verglichen. Im ersten Fall wurde ein Femtosekunden-Laserpuls in ein oder mehrere Submikron-Kerne gekoppelt, während im zweiten Fall der Puls durch den zentralen Kern gesendet wurde. Im ersten Fall konnte eine signifikante Verbreiterung der transmittierten Strahlung beobachtet werden, falls der Pump-Puls nahe an die zero-GVD-Wellenlänge ( $\text{GVD} = \text{Gruppengeschwindigkeitsdispersion}$ ) der MS-Fiber angepasst wurde. Die Eigenschaften der beobachteten Superkontinuumstrahlung weisen auf Szenarien parametrischer Wellenmischung, stimulierte Raman-Streuung und Solitonen-Spaltung hin. Die Superkontinuumserzeugung in dem großen zentralen Kern zeigte eine viel geringere Effizienz. Zudem konnte eine isolierte anti-Stokes Komponente als Ergebnis eines Vier-Wellenmisch-Prozesses von Wellenleiter-Moden höherer Ordnung effizient generiert werden.

Das Ziel des zweiten Teils der Arbeit war es das große Potential von verschiedenen Vier-Wellenmisch-Prozessen zur Untersuchung elektronischer und Schwingungsrelaxations-Prozessen in polyatomaren Molekülen aufzuzeigen. Das Studium dieser Pro-



zesse ist von entscheidender Bedeutung für ein besseres Verständnis der anfänglichen Dynamiken und der Kontrolle photoinduzierter chemischer Reaktionen.

Das Potential der TG-Technik dynamische Prozesse mit niedriger Amplitude aufzulösen, wurde am Beispiel der kohärenten Wellenpaketbewegung in Azulen während der S1/S0 internen Konversion demonstriert. Des Weiteren wurde die TG-Technik dazu verwendet um die charakteristischen Zeitkonstanten der elektronischen Relaxationskanälen einiger Azulenderivate mit hoher Genauigkeit zu bestimmen. Zudem wurde die transiente Absorptionstechnik ('TA = transiente Absorption') angewandt, um spektrale Informationen über die durch Photoanregung generierten angeregten Zustandsspezies zu erhalten. Die Existenz eines langlebigen dunklen Zustands wurde dabei postuliert. Die Kombination aus TG- und TA-Technik erlaubt eine umfassende spektrale und zeitliche Charakterisierung der angeregten Zustandsdynamik.

Die Reorganisation chemischer Bindungen in polyatomaren Molekülen nach Photoanregung in einen elektronisch angeregten Zustand geht einher mit Änderungen der Kerngeometrie. Die Änderungen in den Gleichgewichtspositionen der Atome, d.h. der Normalmoden der Moleküle, sind um Größenordnungen langsamer als elektronische Umlagerungsprozesse und lassen sich mittels 100-fs-Laserpulsen beobachten bzw. auch beeinflussen. Femtochemie hat sich zu einem wichtigen Wissenschaftsbereich entwickelt, der die ultraschnellen dynamischen Prozesse in Molekülen untersucht.

Innerhalb der vorgelegten Arbeit wurde das Modellsystem Stilben-3 mittels der Pump-CARS Technik untersucht, welche es ermöglicht die Population einzelner spezifischer angeregter Schwingungsmoden nach anfänglicher Photoanregung zu verfolgen. Dabei werden Raman-Resonanzen ausgenutzt, welche das CARS-Signal der gewünschten Schwingungsmode selektiv verstärken und somit den CARS-Probeschritt zu einem Moden-selektiven Filter machen. Zusätzlich ermöglicht das Ausnutzen elektronischer Resonanzen eine Diskriminierung zwischen Grund- und angeregtem Signal.

Eine Analyse der beobachteten Zeitabhängigkeit des CARS-Signals vom elektronisch angeregten Zustand zeigte, dass der wichtigste Relaxationsmechanismus der C-C-H-Biegeschwingungen, C-H-Defomationsmoden und der C-O-Streckmoden von Stilben-3 nach Photoanregung Schwingungsrelaxation ('vibrational cooling') ist, welche mit einer Zeitkonstante von 5 ps abläuft. Eine Reorganisation der Stilben-3 C=C-

Doppelbindungen nach Anregung in den ersten angeregten elektronischen Zustand konnte über ein zeitliches Anwachsen der CARS-Signalintensität, wobei der CARS-Prozess Raman-resonant auf die C=C-Doppelschwingungen abgestimmt wurde, verfolgt werden. Die Zeitkonstante für diesen Prozess betrug ungefähr 5 ps.

Zusammenfassend wurde die nichtlineare Frequenzumwandlung niederenergetischer Femtosekunden-Laserpuls in Festkörpern untersucht. Die Raman-Konversion in einem Weisslicht-freien System über impulsiv stimulierte Raman-Streuung wurde durch Pumpen eines KGW-Kristalls mit einem Bessel-Strahl erreicht. Die effiziente Erzeugung eines Superkontinuums konnte durch Fokussierung von sub- $\mu$ J-Puls in eine mikrostrukturierte Fiber nachgewiesen werden. Des Weiteren wurde das große Potential von Vier-Wellen-Misch-Techniken zur Beobachtung der Dynamik polyatomarer Moleküle im elektronisch angeregten Zustand demonstriert. Die spektralen und zeitlichen Eigenschaften der elektronischen Relaxationswege in Azulen-Derivaten wurden mittels TG- und TA-Technik erforscht. Mithilfe der Pump-CARS-Technik konnten in Photo-angeregtem Stilben-3 die Zeitkonstanten der zu den Umverteilungsmechanismen der Schwingungsenergie gehörenden Prozesse bestimmt werden. Dabei fungierte der CARS-Prozess als effektiver Moden-selektiver Filter.

# Bibliography

- [1] P.A. Franken, A.E. Hill, C.W. Peters, and G. Weinreich. *Phys. Rev. Lett.*, **7**:118–119, 1961.
- [2] W.K. Ng E.J. Woodbury. *Proc. IRE*, **50**:2367, 1962.
- [3] N.F. Pilipetskii and A.R. Rustamov. *Sov. JETP*, **2**:88–90, 1965.
- [4] A.M. Prokhorov. *Sov. Phys. JETP*, **7**:1140, 1958.
- [5] A.L. Shawlow and C.H. Townes. *Phys. Rev.*, **112**:1940–1949, 1958.
- [6] T.H. Maiman. *Nature*, **187**:493–493, 1960.
- [7] N.A. Papadogiannis, B. Witzel, C. Kalpouzos, and D. Charalambidis. *Phys. Rev. Lett.*, **83**:4289–4292, 1999.
- [8] M. Hentschel, R. Kienberger, Ch. Spielmann, G.A. Reider, N. Milosevic, T. Brabec, P. Corkum, U. Heinzmann, M. Drescher, and F. Krausz. *Nature*, **414**:509–513, 2001.
- [9] J.A. Valdmanis and R.L. Fork. *IEEE J. Quant. Electr.*, **22**:112–118, 1986.
- [10] R.L. Fork, C.H.B. Cruz, P.C. Becker, and C.V. Shank. *Opt. Lett.*, **12**:483–485, 1987.
- [11] A.H. Zewail. *J. Phys. Chem. A*, **104**:5660–5694, 2000.
- [12] J.C. Joshi and P.B. Corcum. *Physics Today*, **48**:36–43, 1995.
- [13] D.E. Spence, P.N. Kean, and W. Sibbet. *Opt. Lett.*, **16**:42–44, 1991.

- 
- [14] H.A. Haus, J.G. Fujimoto, and E.P. Ippen. *IEEE J. Quant. Electr.*, **28**:2086–2096, 1992.
- [15] G. Steinmeyer, D.H. Sutter, L. Gallmann, N. Matuschek, and U. Keller. *Science*, **286**:1507–1512, 1999.
- [16] *Mira 900 operation manual*.
- [17] J.-C. Diels and W. Rudolph. *Ultrashort laser pulse phenomena*. Academic press, New York, 1999.
- [18] M. Nisoli, S. De Silvestri, V. Magni, O. Svelto, R. Danielius, A. Piskarskas, G. Valiulis, and A. Varanavicius. *opt*, **19**:1973–1975, 1994.
- [19] *TOPAS. User's manual*.
- [20] W. Demtröder. *Laserspektroskopie*. Springer, Berlin, 1993.
- [21] F. Benabid, G. Bouwmans, J.C. Knight, P.St.J. Russell, and F. Couny. *Phys. Rev. Lett.*, **93**:123903/1–123903/4, 2004.
- [22] P. Černý, H. Jelínková, P.G. Zverev, and T.T. Basiev. *Progr. Quant. Electr.*, **28**:113–143, 2004.
- [23] Y.-X. Yan, Jr. E.B. Gamble, and K.A. Nelson. *J. Chem. Phys.*, **83**:5391–5399, 1985.
- [24] S. Ruhman, B. Kohler, A.G. Joly, and K.A. Nelson. *Chem. Phys. Lett.*, **141**:16–24, 1987.
- [25] Y.-X. Yan, L.-T. Cheng, and K.A. Nelson. Impulsive stimulated light scattering. In R.J.H. Clark and R.E. Hester, editors, *Advances in nonlinear spectroscopy*, volume 16 of *Advances in Spectroscopy*. Wiley, 1988.
- [26] G. Korn, O. Duhr, and A. Nazarkin. *Phys. Rev. Lett.*, **81**:1215–1218, 1998.
- [27] A. Nazarkin, G. Korn, M. Wittmann, and T. Elsaesser. *Phys. Rev. Lett.*, **83**:2560–2563, 1999.

- 
- [28] M. Wittmann, A. Nazarkin, and G. Korn. *Opt. Lett.*, **26**:298–300, 2001.
- [29] M. Wittmann, A. Nazarkin, and G. Korn. *Phys. Rev. Lett.*, **84**:5508–5511, 2000.
- [30] P. Černý and H. Jelínková. *Opt. Lett.*, **26**:360–362, 2002.
- [31] N. Zhavoronkov, F. Noack, V. Petrov, V. P. Kalosha, and J. Herrmann. *Opt. Lett.*, **26**:47–49, 2001.
- [32] M. Wittmann and A. Penzkofer. *Opt. Comm.*, **126**:308–318, 1996.
- [33] S. Klewitz, S. Sogomonian, M. Woerner, and S. Herminghaus. *Opt. Comm.*, **154**:186–190, 1998.
- [34] U. T. Schwarz, L. Niggel, and Max Maier. *Opt. Comm.*, **181**:413–423, 2000.
- [35] A. Nazarkin, G. Korn, and T. Elsaesser. *Opt. Comm.*, **203**:403–412, 2002.
- [36] A.S. Grabtchikov, R.V. Chulkov, V.A. Orlovich, M. Schmitt, R. Maksimenka, and W. Kiefer. *Opt. Lett.*, **28**:926–928, 2003.
- [37] A. Smekal. *Naturwiss.*, **11**:873–875, 1923.
- [38] G. Landsberg and L. Mandelstam. *Naturwiss.*, **16**:557–558, 1928.
- [39] C.V. Raman and K.S. Krishnan. *Nature*, **121**:501–502, 1923.
- [40] J. Reintjes and M. Bashkansky. Stimulated Raman and Brillouin scattering. In M. Bass, J.M. Enoch, E.W. Van Stryland, and W.L. Wolfe, editors, *Handbook of Optics, Vol. IV*. McGraw-Hill, New York, 2001.
- [41] W. Kaiser and M. Maier. Stimulated Rayleigh, Brillouin and Raman spectroscopy. In F.T. Arecchi and E.O. Schulz-Dubois, editors, *Laser Handbook, Vol. 2*. North-Holland, Amsterdam, 1972.
- [42] E.J. Woodbury and W.K. Ng. *Proc. IRE*, **50**:2367–2368, 1962.

- [43] G.Eckhardt, R.W. Hellwarth, F.J. McClung, S.E. Schwarz, D. Weiner, and E.J. Woodbury. *Phys. Rev. Lett.*, **9**:455–457, 1962.
- [44] A. Laubereau and W. Kaiser. *Rev. Mod. Phys.*, **50**:607–665, 1978.
- [45] N. Bloembergen and Y.R. Shen. *Phys. Rev. Lett.*, **12**:504–507, 1964.
- [46] G. Hilfer and C.R. Menyuk. *J. Opt. Soc. Am. B*, **7**:739–749, 1990.
- [47] A. Penzkofer, A. Laubereau, and Kaiser. *Progr. Quant. Electr.*, **6**:55–140, 1979.
- [48] H.M. Pask. *Progr. Quant. Electr.*, **27**:3–56, 2003.
- [49] E.E. Hagenlocker, R.W. Minck, and W.G. Rado. *Phys. Rev.*, **154**:226–233, 1967.
- [50] R.L Carman, F. Shimuzu, C.S. Wang, and N. Bloembergen. *Phys. Rev. A*, **2**:60–72, 1970.
- [51] M.D. Duncan, R. Mahon, L.L. Tankersley, and J. Reintjes. *J. Opt. Soc. Am. B*, **5**:37–52, 1988.
- [52] S.A. Akhmanov, V.A. Vysloukh, and A.S. Chirkin. *Optika femtosekundnyh lazernykh impulsov* (Optics of femtosecond laser pulses, in russian), pages 136–137. Nauka, Moskva, 1988.
- [53] M. Sheik-Bahae and M.P. Hasselbeck. Third-order optical nonlinearities. In M. Bass, J.M. Enoch, E.W. Van Stryland, and W.L. Wolfe, editors, *Handbook of Optics, Vol. IV*. McGraw-Hill, New York, 2001.
- [54] J. Durnin. *J. Opt. Soc. Am. A*, **4**:651–654, 1987.
- [55] F.P. Schäfer. *Appl. Phys. B*, **39**:1–8, 1986.
- [56] I. Golub. *Opt. Lett.*, **20**:1847–1849, 1995.
- [57] J. Fagerholm, A.T. Friberga, J. Huttunen, D.P. Morgan, and M.M. Salomaa. *Phys. Rev. E*, **54**:4347–4352, 1996.

- 
- [58] P. Saari and K. Reivelt. *Phys. Rev. Lett.*, **79**:4135–4138, 1997.
- [59] E.B. Treacy. *J. Appl. Phys.*, **42**:3848–3858, 1971.
- [60] J.H. McLeod. *J. Opt. Soc. Am.*, **44**:592–596, 1954.
- [61] G. Eckhardt, D.P. Bortfeld, and M. Geller. **3**:137–138, 1963.
- [62] E.O. Ammann and C.D. Decker. *J. Appl. Phys.*, **48**:1973–1975, 1977.
- [63] A.S. Grabtschikov, A.N. Kuzmin, V.A. Lisinetskii, V.A. Orlovich, and G.I. Ryabtsev. **75**:3742–3744, 1999.
- [64] F.P. Milanovich. Nonlinear optical properties/radiation damage. In M.J. Weber, editor, *Handbook of laser science and technology, Vol. 3*, pages 283–296. CRC Press, 1986.
- [65] T.T. Basiev, A.A. Sobol, P.G. Zverev, V.V. Osiko, and R.C. Powell. **38**:594–598, 1999.
- [66] G. Eckhardt. *IEEE J. Quant. Electr.*, **2**:1–8, 1966.
- [67] I.V. Mochalov. *Opt. Eng.*, **36**:1660–1669, 1997.
- [68] V. Vaičaitis, A. Stabinis, A. Marcinkevičius, and V. Jarutis. *Opt. Comm.*, **178**:461–467, 2000.
- [69] E.M. Belenov, P.G. Kryukov, A.V. Nazarkin, and I.P. Prokopovich. *J. Exp. Theor. Phys.*, **78**:15–22, 1994.
- [70] J.C. Knight, T.A. Birks, P.S.J. Russell, and D.M. Atkin. *Opt. Lett.*, **21**:1547–1549, 1996.
- [71] P.J. Bennet, T.M. Monro, and D.J. Richardson. *Opt. Lett.*, **24**:1203–1205, 1999.
- [72] A.B. Fedotov, A.M. Zheltikov, L.A. Mel’nikov, A.P. Tarasevitch, and D. von der Linde. *JETP Lett.*, **71**:281–284, 2000.

- [73] D.A. Akimov, A.A. Ivanov, M.V. Alfimov, S.N. Bagayev, T.A. Birks, W.J. Wadsworth, P.S.J. Russell, A.B. Fedotov, V.S. Pivtsov, A.A. Podshivalov, and A.M. Zheltikov. *Appl. Phys. B*, **74**:307–311, 2002.
- [74] *Nonlinear Optics of Photonic Crystals*, Feature Iss. *J. Opt. Soc. Am. B*, **19**, 2002.
- [75] N.G.R. Broderick, T.M. Monro, P.J. Bennett, and D.J. Richardson. *Opt. Lett.*, **24**:1395–1397, 1999.
- [76] W.H. Reeves, J.C. Knight, P.S.J. Russell, and P.J. Roberts. *Opt. Express*, **10**:609–613, 2002.
- [77] S.A. Diddams, D.J. Jones, J. Ye, S.T. Cundiff, J.L. Hall, J.K. Ranka, R.S. Windeler, R. Holzwarth, T. Udem, and T.W. Hänsch. *Phys. Rev. Lett.*, **84**:5102–5105, 2000.
- [78] T. Udem, S.A. Diddams, K.R. Vogel, C.W. Oates, E.A. Curtis, W.D. Lee, W.M. Itano, R.E. Drullinger, J.C. Bergquist, and L. Hollberg. *Phys. Rev. Lett.*, **86**:4996–4999, 2001.
- [79] S. Lakó, J. Seres, P. Apai, J. Balázs, R.S. Windeler, and R. Szipöcs. *Appl. Phys. B*, **76**:267–275, 2003.
- [80] I. Hartl, X.D. Li, C. Chudoba, R.K. Rhanta, T.H. Ko, J.G. Fujimoto, J.K. Ranka, and R.S. Windeler. *Opt. Lett.*, **26**:608–610, 2001.
- [81] A. Baltuska, T. Fuji, and T. Kobayashi. *Opt. Lett.*, **27**:1241–1243, 2002.
- [82] J. Herrmann, U. Griebner, N. Zhavoronkov, A. Husakou, D. Nickel, J.C. Knight, W.J. Wadsworth, P.S.J. Russell, and G. Korn. *Phys. Rev. Lett.*, **88**:173901/1–4, 2002.
- [83] A.N. Naumov, A.B. Fedotov, A.M. Zheltikov, V.V. Yakovlev, L.A. Mel’nikov, V.I. Beloglazov, N.B. Skibina, and A.V. Shcherbakov. *J. Opt. Soc. Am. B*, **19**:2183–2190, 2002.



- [84] D.A. Akimov, A.A. Ivanov, M.V. Alfimov, T.A. Birks, W.J. Wadsworth, P.S.J. Russell, O.A. Kolevatova, A.B. Fedotov, S.O. Konorov, A.A. Podshivalov, and A.M. Zheltikov. *JETP Lett.*, **77**:7–11, 2003.
- [85] A.B. Fedotov, P. Zhou, A.N. Naumov, V.V. Temnov, V.I. Beloglazov, N.B. Skibina, L.A. Mel'nikov, A.V. Shcherbakov, A.P. Tarasevitch, D. von der Linde, and A.M. Zheltikov. *Appl. Phys. B*, **75**:621–627, 2002.
- [86] A.B. Fedotov, P. Zhou, A.P. Tarasevitch, K.V. Dukel'skii, Y.N. Kondrat'ev, V.S. Shevandin, V.B. Smirnov, D. von der Linde, and A.M. Zheltikov. *J. Raman Spectrosc.*, **33**:888–895, 2002.
- [87] D.A. Akimov, M. Schmitt, R. Maksimenka, K.V. Dukel'skii, Y.N. Kondrat'ev, A.V. Khokhlov, V.S. Shevandin, W. Kiefer, and A.M. Zheltikov. *Appl. Phys. B*, **77**:719–726, 2003.
- [88] D.A. Akimov, E.E. Serebryannikov, A.M. Zheltikov, M. Schmitt, R. Maksimenka, W. Kiefer, K.V. Dukel'skii, V.S. Shevandin, and Y.N. Kondrat'ev. *Opt. Lett.*, **28**:1048–1050, 2003.
- [89] P.B. Corkum, C. Rolland, and T. Srinivasan-Rao. *Phys. Rev. Lett.*, **57**:2268–2271, 1986.
- [90] A.A. Babin, D.V. Kartashov, A.M. Kiselev, V.V. Lozhkarev, A.N. Stepanov, and A.M. Sergeev. *Appl. Phys. B*, **75**:509–514, 2002.
- [91] J.K. Ranka, R.S. Windeler, and A.J. Stentz. *Opt. Lett.*, **25**:25–27, 2000.
- [92] A.B. Fedotov, A.M. Zheltikov, A.P. Tarasevitch, and D. von der Linde. *Appl. Phys. B*, **73**:181–184, 2001.
- [93] G. Yang and Y.R. Shen. *Opt. Lett.*, **9**:510–512, 1984.
- [94] J.J. Glowina, J. Misewich, and P.P. Sorokin. *J. Opt. Soc. Am. B*, **3**:1573–1579, 1986.

- [95] F.A. Ilkov, L.Sh. Ilkova, and S.L. Chin. *Opt. Lett.*, **18**:681–683, 1993.
- [96] N. Bloembergen. *Opt. Comm.*, **8**:285–288, 1973.
- [97] S.P. Le Blanc, R. Sauerbrey, S.C. Rae, and K. Burnett. *J. Opt. Soc. Am. B*, **10**:1801–1809, 1993.
- [98] S.A. Akhmanov, V.A. Vysloukh, and A.S. Chirkin. *Optika femtosekundnyh lazernykh impulsov* (Optics of femtosecond laser pulses, in russian). Nauka, Moskva, 1988.
- [99] T. Brabec and F. Krausz. *Phys. Rev. Lett.*, **78**:3282–3285, 1997.
- [100] A.L. Gaeta. *Phys. Rev. Lett.*, **84**:3582–3585, 2000.
- [101] N. Akozbek, M. Scalora, C.M. Bowden, and S.L. Chin. *Opt. Comm.*, **191**:353–362, 2001.
- [102] A.L. Gaeta. *Opt. Lett.*, **27**:924–926, 2002.
- [103] V.P. Kandidov, O.G. Kosareva, I.S. Golubtsov, W. Liu, A. Becker, N. Akozbek, C.M. Bowden, and S.L. Chin. *Appl. Phys. B*, **77**:2268–2271, 2003.
- [104] G.P. Agrawal. *Nonlinear fiber optics*. Academic, Boston, 1989.
- [105] A.W. Snyder and J.D. Love. *Optical Waveguide Theory*. Chapman and Hall, New York, 1983.
- [106] S.O. Konorov, A.B. Fedotov, W. Boutu, E.E. Serebryannikov, D.A. Sidorov-Biryukov, Yu.N. Kondrat'ev, V.S. Shevandin, K.V. Dukel'skii, A.V. Khokhlov, and A.M. Zheltikov. *Opt. Spectrosc.*, **94**:575–579, 2004.
- [107] A.M. Zheltikov, P. Zhou, V.V. Temnov, Yu.N. Kondrat'ev, S.N. Bagayev, V.S. Shevandin, K.V. Dukel'skii, A.V. Khokhlov, V.B. Smirnov, A.P. Tarasevitch, and D. von der Linde. *Quant. Electron.*, **32**:542–544, 2002.

- [108] A.B. Fedotov, S.O. Konorov, Y.N. Kondrat'ev, S.N. Bagayev, V.S. Shevandin, K.V. Dukel'skii, D.A. Sidorov-Biryukov, A.V. Khokhlov, V.B. Smirnov, and A.M. Zheltikov. *Laser Phys.*, **13**:856–860, 2003.
- [109] S. Coen, A.H.L. Chau, R. Leonhardt, J.D. Harvey, J.C. Knight, W.J. Wadsworth, and P.S.J. Russell. *Opt. Lett.*, **26**:1356–1358, 2001.
- [110] S. Coen, A.H.L. Chau, R. Leonhardt, J.D. Harvey, J.C. Knight, W.J. Wadsworth, and P.S.J. Russell. *J. Opt. Soc. Am. B*, **19**:753–764, 2002.
- [111] T.M. Monro, D.J. Richardson, N.G.R. Broderick, and P. J. Bennett. *J. Lightwave Technol.*, **17**:1093–1120, 1999.
- [112] A.H. Zewail. *Femtochemistry: Ultrafast dynamics of the chemical bond, volume I+II*. World Scientific, Singapore, 2001.
- [113] J. Manz and L. Wörste, editors. *Femtosecond chemistry*. VCH, Weinheim, 1995.
- [114] H.J. Eichler, P. Günter, and D. W. Pohl. *Laser-Induced Dynamic Gratings*. Springer, Berlin, 1986.
- [115] E.J. Brown, Q. Zhang, and M. Dantus. *J. Chem. Phys.*, **110**:5772–5788, 1999.
- [116] L. Gomez-Jahn, J. Kasinski, and R.J.D. Miller. *Chem. Phys. Lett.*, **125**:500–506, 1986.
- [117] F.W. Deeg, J.J. Stankus, S.R. Greenfield, V.J. Newell, and M.D. Fayer. *J. Chem. Phys.*, **90**:6893–6902, 1989.
- [118] M. Terazima. *Chem. Phys. Lett.*, **218**:574–578, 1994.
- [119] E. Vauthey and A. Henseler. *J. Phys. Chem.*, **100**:170–175, 1996.
- [120] T. Siebert, V. Engel, A. Materny, W. Kiefer, and M. Schmitt. *J. Phys. Chem. A*, **107**:8355–8362, 2003.

- [121] B. Dietzek, R. Maksimenka, G. Hermann, W. Kiefer, J. Popp, and M. Schmitt. *ChemPhysChem*, **5**:1171–1177, 2004.
- [122] K. Holliday, M. Croci, E. Vauthey, and U.P. Wild. *Phys. Rev. B*, **47**:14741–14752, 1993.
- [123] A. Laubereau. In W. Kaiser, editor, *Ultrafast laser pulses and applications*. Vol. 60, Topics in applied physics, page 411. Wiley-VCH, Weinheim, 2000.
- [124] T. Siebert. *Four-wave mixing techniques applied to the investigation of non-adiabatic dynamics in polyatomic molecules*. PhD thesis, Universität Würzburg, 2002.
- [125] S.A. Payne and R.M. Hochstrasser. *J. Phys. Chem.*, **90**:2068–2074, 1986.
- [126] J.-M. Funk, U. Schmitt, W. Kiefer, and A. Materny. *J. Raman Spec.*, **31**:743–753, 2000.
- [127] T. Siebert, M. Schmitt, V. Engel, A. Materny, and W. Kiefer. *J. Am. Chem. Soc.*, **124**:6242–6243, 2002.
- [128] T. Siebert, R. Maksimenka, A. Materny, V. Engel, W. Kiefer, and M. Schmitt. *J. Raman Spectrosc.*, **33**:844–854, 2002.
- [129] F.X. Redl, O. Köthe, K. Röckl, W. Bauer, and J. Daub. *Macromol. Chem. Phys.*, **201**:2091–2100, 2000.
- [130] S. Schmitt, M. Baumgarten, J. Simon, and K. Hafner. *Angew. Chem. Int. Ed.*, **37**(8):1077–1081, 1998.
- [131] T. Mrozek, H. Görner, and J. Daub. *Chem. Eur. J.*, **7**:1028–1040, 2001.
- [132] P. Wang, P. Zhu, C. Ye, A.E. Asato, and R.S.H. Liu. *J. Phys. Chem. A*, **103**:7076–7082, 1999.
- [133] J.J. Wolff and R. Wortmann. *Adv. Phys. Org. Chem.*, **32**:121–217, 1999.

- [134] T. Verbiest, S. Houbrechts, M. Kauranen, K. Clays, and A. Persoons. *J. Mater. Chem.*, **7**:2175–2189, 1997.
- [135] C. Lambert, W. Gaschler, E. Schmälzlin, K. Meerholz, and C. Bräuchle. *J. Chem. Soc. Perkin Trans.*, **2**:577–588, 1999.
- [136] B.S. Brunshwig, C. Creutz, and N. Sutin. *J. Chem. Soc. Perkin Trans.*, **31**:168–184, 2002.
- [137] J.-P. Launay. *Chem. Soc. Rev.*, **30**:386–397, 2001.
- [138] K.D. Demadis, C.M. Hartshorn, and T.J. Meyer. *Chem. Rev.*, **101**:2655–1686, 2001.
- [139] S.F. Nelsen, R.F. Ismagilov, and D.A. Trieber. *Science*, **278**:846–849, 1997.
- [140] S.F. Rak and L.L. Miller. *J. Am. Chem. Soc.*, **114**:1388–1394, 1992.
- [141] M. Mayor, M. Büschel, K.M. Fromm, J.-M. Lehn, and J. Daub. *Chem. Eur. J.*, **7**:1266–1272, 2001.
- [142] P. Strohriegl and J.V. Grazulevicius. *Adv. Mater.*, **14**:1439–1452, 2002.
- [143] D.P. West and M.D. Rahn. In V. Balzani, editor, *Electron Transfer in Chemistry, Vol. 5*, page 472. Wiley-VCH, Weinheim, 2001.
- [144] C. Lambert, G. Nöll, M. Zabel, F. Hampel, E. Schmälzlin, C. Bräuchle, and K. Meerholz. *Chem. Eur. J.*, **9**:4232–4239, 2003.
- [145] M. Beer and H.C. Longuet-Higgins. *J. Chem. Phys.*, **23**:1390–1391, 1955.
- [146] A.J. Wurzer, T. Wilhelm, J. Piel, and E. Riedle. *Chem. Phys. Lett.*, **299**:296–302, 1999.
- [147] M.J. Bearpark, F. Bernardi, S. Clifford, M. Olivucci, M.A. Robb, B.R. Smith, and T. Vreven. *J. Am. Chem. Soc.*, **118**:169–175, 1996.

- [148] B.D. Wagner, D. Tittelbach-Helmrich, and R.P. Steer. *J. Phys. Chem.*, **96**:7904–7908, 1992.
- [149] A.J. Wurzer, S. Lochbrunner, and E. Riedle. *App. Phys. B*, **71**:405–409, 2000.
- [150] A.A. Ruth, E.-K. Kim, and A. Hese. *Phys. Chem. Chem. Phys.*, **1**:5121, 1999.
- [151] D.J. Tannor and S.A. Rice. *Adv. Chem. Phys.*, **70**:441–523, 1988.
- [152] V. Kozich, W. Werncke, J. Dreyer, K.-W. Brzezinka, M. Rini, A. Kummrow, and T. Elsaesser. *J. Chem. Phys.*, **117**:719–726, 2002.
- [153] I. Hartl, P. Gilch, and W. Zinth. *App. Phys. B*, **71**:397–403, 2000.
- [154] W. Wernecke, K. Kozisch, J. Dreyer, M. Rini, A. Kummrow, and T. Elsaesser. Vibrational excitation and energy redistribution due to back-electron transfer in para-nitroaniline. In *XII Conference on Ultrafast Processes in Spectroscopy(UPS), Florence*, 2001.
- [155] M. Yoshizawa and M. Kurosawa. *Phys. Rev. A*, **61**:13808/1–6, 2000.
- [156] D.W. McCamant, Ph. Kukura, and R.A. Mathies. *Appl. Spec.*, **57**:1317–1323, 2003.
- [157] M. Yoshizawa, H. Aoki, and H. Hashimoto. *Bull. Chem. Soc. Jpn.*, **75**:949–955, 2002.
- [158] D.W. McCamant, Ph. Kukura, and R.A. Mathies. *J. Phys. Chem. A*, **107**:8208–8214, 2003.
- [159] W. Kiefer, A. Materny, and M. Schmitt. *Naturwissenschaften*, **89**:250–258, 2002.
- [160] M. Motzkus, S. Pedersen, and A.H. Zewail. *J. Phys. Chem.*, **100**:5620–5633, 1996.
- [161] V. Blanchet, M.Z. Zgierski, T. Seideman, and A. Stolow. *Nature*, **401**:52–54, 1999.

- [162] D. Zigmantas, T. Polivka, R.G. Hiller, A. Yartsev, and V. Sundström. *J. Phys. Chem. A*, **105**:10296–10306, 2001.
- [163] S. Mukamel. *Ann. Rev. Phys. Chem.*, **51**:691–729, 2000.
- [164] P. Hamm, M. Lim, and M. Hochstrasser. *J. Phys. Chem. B*, **102**:6123–6138, 1998.
- [165] R. Maksimenka, B. Dietzek, T. Siebert, A. Szeghalmi, W. Kiefer, and M. Schmitt. *Chem. Phys. Lett.*, 2005.
- [166] S. Maeda, T. Kamisuki, and Y. Adachi. Condensed phase cars. In R.J.H. Clark, editor, *Advances in Spectroscopy, Vol. 15 (Adv. Non-Linear Spectrosc.)*. Wiley, Chichester, UK, 1988.
- [167] R.K. Bauer, A. Balter, A. Kowalczyk, and Ch. Jung. *Z. Naturforsch.*, **35A**:1319–1324, 1980.
- [168] B.J. Prince, N.T. Kaltcheva, A.W. Schwabacher, and Peter Geissinger. *Appl. Spec.*, **55**:1018–1024, 2001.
- [169] N. Izard, C. Ménard, D. Riel, E. Doris, C. Mioskowski, and E. Anglaret. *Chem. Phys. Lett.*, **391**:124–128, 2004.
- [170] W. Werncke, A. Lau, M. Pfeiffer, K.M. Bok, and T.J. Tscholl. Time-resolved resonance-CARS spectroscopy of the first excited singlet state of stilbene-3 and of cyanine photoisomers. In E. Klose and B. Wilhelmi, editors, *Springer Proceedings in Physics, Vol. 49 (Ultrafast Phenom. Spectrosc.)*, Berlin-Heidelberg, 1990. Springer.
- [171] R. Leonhardt, W. Holzappel, W. Zinth, and W. Kaiser. *Rev. Phys. Appl.*, **22**:1735–1741, 1987.
- [172] S. Meyer, M. Schmitt, A. Materny, W. Kiefer, and V. Engel. *Chem. Phys. Lett.*, **281**:332–336, 1997.

- 
- [173] M. Heid, T. Chen, U. Schmitt, and W. Kiefer. *Chem. Phys. Lett.*, **334**:119–126, 2001.
- [174] T.L. Gustafson, D.M. Roberts, and D.A. Chernoff. *J. Chem. Phys.*, **81**:3438–3443, 1984.
- [175] J. Qian, S.L. Schulz, G.R. Bradburn, and J.M. Jean. *J. Phys. Chem.*, **97**:10638–10644, 1993.
- [176] T. Nakabayashi, H. Okamoto, and M. Tasumi. *J. Phys. Chem. A*, **102**:9686–9695, 1998.



# Acknowledgments

It is impossible to imagine the work described in this thesis to be done without help and support of many people, surrounded me.

First of all, I would like to express my gratitude to Prof. Dr. Dr. h.c. Wolfgang Kiefer, for providing me with a fascinating subject for my PhD thesis and for possibility to work in outstandingly equipped lab. He created the atmosphere of the friendly support. At the same time, independence in expression of own ideas also greatly encouraged my experimental work.

I sincerely appreciate PD Dr. Michael Schmitt for everything he taught me from my first days in Würzburg. His patience in disputes concerning experimental as well as theoretical aspects of my work I also strongly recognize. For all the wisdom and things he shared with me I thank femto-guru Dr. Torsten Siebert.

I will always be obliged to Prof. Dr. Valentin Antonovich Orlovich and to Dr. Alexander Stepanovich Grabtchikov for continuous scientific and moral support from my motherland, Belarus. I greatly appreciate the times, when Dr. Grabtchikov was visiting Würzburg. I would like to note the crucial role played in my life by Julia Kruchenok.

I thank cordially Dr. Adriana Szeghalmi for helping me a lot in getting used to Würzburg and to Germany in general. It was a special joy to work together with Dr. Krisztina Babosci, who was always a ray of sunlight in darkness of femtolab. I thank Benjamin Dietzek as well as Dr. Denis Akimov for wonderful team work, for fruitful discussions concerning nonlinear optics and for their faultless readiness to help. Warmest thanks to Niculina Peica and Bernd Küstner for being always so nice. I thank to the present and the former members of AK Kiefer, my colleagues and friends from Institutes of Physical, Organic and Inorganic Chemistry for nice time we spent together during last 3.67 years.

I am grateful to Frau Ulrsula Müller for her help concerning official stuff. Thanks to Belinda Böhm and the personnel of the mechanical and electronic workshops for their help concerning technical stuff. For stable Internet connection thanks to Peter Popp. With a sorrow I remember about Melanie Grom, whose smile will always stay with us.

I thank my parents and friends from Minsk, Soligorsk, München, Berlin and Kiel for continuous moral support.

For all the love she is giving, I thank my wife Katja. For all the joy he is bringing, I thank my son Matvei.

# Cirriculum Vitae

---

## Personal:

Name: Raman Maksimenka  
Date of birth: January, 16 1979  
Place of birth: Soligorsk, Belarus  
Marital status: married

---

## School:

1989 - 1994 Secondary School, Soligorsk, Belarus  
1994 - 1996 Liceum affilated with Belarusian State University,  
Minsk, Belarus

---

## Study:

09.1996 - 07.2001 At the Faculty of Physics, Belarusian State Uni-  
versity, Minsk  
09.2000 - 05.2001 Graduation work, performed in Laboratory of Lu-  
minescence, Vavilov Institute of Physics, National  
Academy of Sciences of Belarus, Minsk  
Title: "Photophysical Properties of Novel Fluores-  
cent Membrane Probes"  
06.2001 Diplom (Master degree) in Physics

---

## Postgraduate study:

09.2001 - 03.2005 In the Institute of Physical Chemistry, University  
of Wuerzburg, in the group of Prof. W. Kiefer  
Subject: "Techniques in Frequency Conversion  
and Time-Resolved Spectroscopy with Nonlinear  
Optical Processes in the Femtosecond Regime"

---

June 19, 2005

Raman Maksimenka